



Study of electronic states in novel materials:
Topological insulators and rare-earth dantimonides

Matteo Michiardi

PhD Dissertation



Department of Physics and Astronomy
Aarhus University
Denmark

Study of electronic states in novel
materials:
Topological insulators and rare-earth
diantimonides

A Dissertation
Presented to the Faculty of Science and Technology
of Aarhus University
in Partial Fulfilment of the Requirements
for the PhD Degree

by
Matteo Michiardi
November 1, 2015

Supervisor:
Philip Hofmann

Preface

The research presented in this dissertation was conducted from November 2012 to October 2015. The official enrolment in the PhD program at the Aarhus Graduate School of Science was accepted from August 2012. The work was performed under the supervision of: Professor Philip Hofmann, Department of Physics and Astronomy, Interdisciplinary Nanoscience Centre, Aarhus University, 8000 Aarhus C, Denmark.

This thesis is submitted to the Faculty of Science at Aarhus University in order to fulfil the requirements for obtaining a PhD degree in physics. The work has been carried out primarily at the Department of Physics and Astronomy (IFA) and at the Institute for Storage Ring Facilities in Aarhus (ISA).

Most of the research performed during these three years were done at the SGM3 beamline at ISA. In 2012/2013 the beamline was fed by the radiation produced in the ASTRID synchrotron. In 2013/2014 I was involved in moving and commissioning the beamline and the end-station to the new ASTRID2 synchrotron. From summer 2014 the new SGM3 beamline become operational and the last period was spent there. Additionally, I spent some time in Hamburg university in collaboration with the scanning tunnelling microscopy group of Roland Wiesendanger and in international synchrotron facilities, in particular at the spin-ARPES beamline i3 at Max-Lab.

Abstract

In this thesis we present a series of experimental work exploring the electronic structure of some materials with intriguing electronic properties: topological insulators and rare earth diantimonides. Topological insulators (TI) are a newly discovered state of matter where, because of the unconventional topology of the band structure, spin-polarised states are found at the surface [1–3]. These topological states are protected by the time reversal symmetry of the system. Topological insulators are extensively studied for their exotic properties and promising technological applications. We focus in this work on the prototypical topological insulators Bi_2Te_3 , $\text{Bi}_2\text{Te}_2\text{Se}$ and Bi_2Se_3 , utilizing angle resolved photoemission spectroscopy (ARPES) as our principal experimental technique.

The combination of ARPES and *ab initio* calculations was used to map the bulk band structure of Bi_2Te_3 , where many-body effects were found to be vital to its accurate description [4]. Secondly the surface properties of $\text{Bi}_2\text{Te}_2\text{Se}$ and Bi_2Te_3 were investigated under surface modification: a two dimensional electron gas (2DEG) with strong spin-orbit splitting is induced at the surface by local deposition of Rb, an electron donor. The dispersion of the 2DEG is found to be seemingly at odds with standard models of Rashba splitting for free electron states, possessing a strong anisotropy both in the dispersion and in the momentum splitting. The observed dispersion is successfully modelled with an effective Rashba Hamiltonian with the inclusion of band structure effects on the dispersion. The interplay between band structure and spin-orbit splitting can give rise to complex spin texture and can be exploited to maximize spin-orbit splitting in the momentum direction, paving the way to anisotropic spin transport phenomena [5]. The doping of the same surfaces with magnetic adatoms Ni and Fe also reveals an n-doping effect, but not the spectroscopic evidence of broken time-reversal symmetry that might be expected for these systems. The magnetisation was found to be out of the surface plane for the Fe adatoms, while the Ni exhibits a quenched magnetic moment. Moreover we explore the electronic structure at the interface between Bi_2Se_3 and the two dimensional topological insulator candidate Bi-bilayer by studying quasi-particle interference effects (QPI) at the surface detected with scanning tunnelling spectroscopy. We develop a semi-theoretical model to study the QPI pattern of complex systems employing joint density of states simulations. We find that the interface electronic structure is a complex mixture of states from both Bi_2Se_3 and Bi where a new interface spin polarized Dirac state is created [6].

Finally we report the study of the electronic structure of the rare earth diantimonide LaSb_2 by ARPES and *ab initio* calculations. LaSb_2 was found in previous works to possess an exotic linear and non-saturating magnetoresistance as well as superconductivity [7, 8]. The investigated electronic structure reveals a semimetal character with uneven hole and electron pockets. The key to the linear magnetoresistance might lie in strongly directional Dirac-like bands with small carrier density found close to the Fermi level.

Resumé

I denne afhandling vil vi præsentere en række eksperimentelle værker, som udforsker elektronisk struktur og egenskaber i materialer, hvor disse er af særlig interesse: topologiske insulatorer og sjældne jordartsdiantimoner. Topologiske insulatorer (TI) er en nyligt opdaget tilstand, som visse materialer kan optræde i. Grundet deres ukonventionelle topologi i båndstrukturen kan man finde spin-polariserede tilstande på overfladen af disse materialer [1–3]. Disse tilstande er beskyttede af tid-omvendingssymmetrien i systemet. Topologiske insulatorer bliver studeret grundigt, da de har eksotiske egenskaber samt lovende teknologiske anvendelsesmuligheder. Vi fokuserer her på de prototypiske topologiske insulatorer Bi_2Te_3 , $\text{Bi}_2\text{Te}_2\text{Se}$ og Bi_2Se_3 , og vi bruger vinkelopløst photoemissionsspektroskopi (ARPES) som vores primære eksperimentelle teknik.

En kombination af ARPES og *ab initio* beregninger er blevet brugt til at undersøge båndstrukturen af den tredimensionelle tilstand af Bi_2Te_3 , hvor mange-delseffekter viser sig uvurderlige for en nøjagtig beskrivelse [4].

Desuden er overflade-egenskaberne for $\text{Bi}_2\text{Te}_2\text{Se}$ og Bi_2Te_3 blevet udforsket under overflade modifikation: En todimensionel elektron gas (2DEG) med kraftig spin-orbit opsplittning induceres på overfladen ved aflejring af rubidium - en elektron donor. Spredningen af 2DEG'en synes umiddelbart at være i strid med standard modellen for Rashba opsplittning for frie elektroniske tilstande, idet den udviser en kraftig anisotropi i såvel dispersion som momentum opsplittning. Den observerede spredning kan med god præcision modelleres med en effektiv Rashba Hamilton operator, som inkluderer båndstrukturens effekt på spredningen. Samspillet imellem båndstrukturen og spin-orbit opsplittning kan give ophav til komplekse spin teksture, og det kan udnyttes til at maksimere spin-orbit opsplittningen i retning af momentumet. Dette fører til anisotropisk spin transport fænomener [5].

Doping af de samme overflader med magnetiske adatomer som nikkell og jern viser en n-doping effekt, men de forventede spektroskopiske effekter, som forårsages af et brud på tid-omvendingssymmetrien, ses ikke i disse systemer. Magnetiseringen blev påvist at være vinkelret på overfladen for jern adatomerne, mens nikkels magnetiske moment dæmpes.

Yderligere udforsker vi den elektroniske struktur af grænsefladen imellem Bi_2Se_3 og en todimensionel topologisk insulator kandidat, et bismuth dobbelt lag, ved at studere quasipartikel interferens effekter (QPI) ved overfladen ved brug af skanning tunneleringsspektroskopi. Vi har udviklet en semi-teoretisk model til studiet af QPI mønstret i komplekse systemer, som benytter simuleringer bygget på fælles tæthed af tilstande. Vi finder, at grænsefladens elektroniske struktur er en kompleks blanding af tilstande fra såvel Bi_2Se_3 som bismuth, som tilsammen danner en ny interface spin-polariseret Dirac tilstand [6].

Slutteligt beskriver vi et studie af den elektroniske struktur af den sjældne jordartsdiantimon LaSb_2 via ARPES og *ab initio* beregninger. Det er tidligere blevet vist, at LaSb_2 har en eksotisk lineær og umættelig magnetoresistans og superkonduktivitet. Den

undersøgte elektroniske struktur afslører en semimetallisk karakter med ujævne huler og elektronlommer [7, 8]. Nøglen til den lineære magnetoresistans skal måske findes i særdeles retningsbestemte Dirac-lignende bånd med lav carrier tæthed, som findes tæt ved Fermi-niveauet.

Acknowledgments

I do believe the acknowledgements are better done in person, but I realize that the written word can be a more permanent memento, that one might want to read to look back at the time passed.

Thanks are due to all members of the group, past and present, that helped me, discussed with me and collaborated with me; internal collaborations are not explicitly written in the text of the thesis but all the experiments were always performed with the precious help of people in the group. Special thanks to Philip Hofmann for his scientific guidance, for his contagious passion and his great humanity. Thanks to Marco Bianchi for being the most fatherly figure to me when it comes to UHV and ARPES. Special thanks to Maciek and Charlotte for the many laughs in the lab, in the office and in the outside world, for the scientific stimulation, the trips across Europe and the great personal support. Particular thanks to Antonija for all the tea, to Fabian, for being the best foosball partner, to Arlette for her teachings, to Jill for her spirit, to Søren for his passion for beer and science. Thank you to all external collaborators whose collaboration I hope to maintain through my scientific carrier. In particular thanks to all people who spent sleepless days with me at beamtimes.

*Matteo Michiardi,
Aarhus, November 1, 2015.*

List of Publications

Publications relevant for the thesis

Strongly anisotropic spin-orbit splitting in a 2 dimensional electron gas, Matteo Michiardi, Marco Bianchi, Maciej Dendzik, Jill Miwa, Moritz Hoesch, Timur K. Kim, Peter Matzen, Jianli Mi, Martin Bremholm, Bo Brummerstedt Iversen and Philip Hofmann, Physical Review B 91, 035445 (2015).

Intra- and Interband Electron Scattering in the Complex Hybrid Topological Insulator Bismuth Bilayer on Bi_2Se_3 , A. Eich, M. Michiardi, G. Bihlmayer, X.-G. Zhu, J.-L. Mi, Bo B. Iversen, R. Wiesendanger, Ph. Hofmann, A. A. Khajetoorians and J. Wiebe, Physical Review B 90, 155414 (2014).

Bulk band structure of Bi_2Te_3 , Matteo Michiardi, Irene Aguilera, Marco Bianchi, Vagner Eustáquio de Carvalho, Luiz Orlando Ladeira, Nayara Gomes Teixeira, Edmar Avellar Soares, Christoph Friedrich, Stefan Blügel and Philip Hofmann, Physical Review B 90, 075105 (2014).

Other Publications

Growth and electronic structure of epitaxial single-layer WS_2 on $Au(111)$, Maciej Dendzik, Matteo Michiardi, Charlotte Sanders, Marco Bianchi, Jill A. Miwa, Signe S. Grønberg, Jeppe Vang Lauritsen, Philip Hofmann, Submitted (2015), arXiv:1509.05133v1.

Direct observation of spin-polarised bulk bands in an inversion-symmetric semiconductor, Jonathon Riley, Federico Mazzola, Maciej Dendzik, Matteo Michiardi, Tomohiro Takayama, Lewis Bawden, Cecilie Granerød, Mats Leandersson, Thiagarajan Balasubramanian, Moritz Hoesch, Timur Kim, Hide Takagi, Worawat Meevasana, Philip Hofmann, Mohammad Bahramy, Justin Wells, and Phil King, Nature Physics 10, 835 (2014), see also News and Views by John Schaibley and Xiaodong Xu.

Tailoring the electronic texture of a topological insulator via its surface orientation, Xie-Gang Zhu, Malthe Stensgaard, Lucas Barreto, Wendell Simoes e Silva, Søren Ulstrup, Matteo Michiardi, Marco Bianchi, Maciej Dendzik, and Philip Hofmann, New Journal of Physics 15, 103011 (2013).

Factors determining the gas crossover through pinholes in polymer electrolyte fuel cell membranes, Stefan Kreitmeier, Matteo Michiardi, Alexander Wokaun, Felix N. Büchi, *Electrochimica acta*, 80, 240 (2012).

Contents

Preface	i
Abstract	iii
Resumé	v
Acknowledgements	vii
List of Publications	ix
Contents	xi
I Introduction	1
1 Theoretical background	5
1.1 Electronic structure of surfaces	6
1.2 Spin-orbit coupling	7
1.2.1 Symmetry dependent spin-orbit interaction	8
1.3 Topological Insulators	11
1.3.1 Definition of a topological invariant	12
1.3.2 A massless surface state topologically protected	14
1.4 Other Dirac fermions	15
2 Experimental techniques	17
2.1 Angle Resolved Photoemission Spectroscopy	17
2.1.1 Photoemission process	17
2.1.2 Electron momentum in photoemission	19
2.1.3 Spectral shape and quasi particle effects	22
2.1.4 Acquiring and analysing ARPES Data	24
2.1.5 The beamlines: SGM3 at ASTRID and ASTRID2	26
2.2 Scanning tunnelling microscopy and spectroscopy	27
II Results and Discussion	33
3 Bulk band structure of Bi_2Te_3	35
3.1 Bismuth chalcogenides topological insulators	35

3.2	A study of the Bi_2Te_3 bulk band structure	37
3.2.1	The calculated band structure: LDA vs GW	38
3.2.2	ARPES vs DFT	38
3.3	Summary	43
4	Surface modifications and new electron states in bismuth tellurides	45
4.1	Two dimensional electron gasses at surfaces	45
4.2	Anisotropic 2DEGs on topological insulators	47
4.2.1	Rb-surface doping of $\text{Bi}_2\text{Te}_2\text{Se}$	47
4.2.2	An exotic 2DEG	49
4.2.3	The “warped” effective Rashba Hamiltonian	50
4.2.4	Analysis of the splitting	53
4.3	The case of Bi_2Te_3	56
4.4	An outlook	60
4.5	Exploring the magnetic properties with magnetic surface doping	63
4.5.1	Adsorption sites	64
4.5.2	Magnetic properties	65
4.5.3	Effect of magnetic adatoms on the electronic structure	66
5	Interfacing a 2D and a 3D topological insulator - $\text{Bi}/\text{Bi}_2\text{Se}_3$	69
5.1	The electronic structure of the interface	70
5.1.1	ARPES characterization	71
5.1.2	DFT calculations	73
5.2	FT-STs and JDOS simulations, an indirect probe of complex structures	74
5.2.1	Quasi particle interferences	75
5.2.2	The simulation procedure: the Joint Density of States	75
5.2.3	QPI vs JDOS	81
5.3	Conclusions	84
6	Electronic structure of rare earth diantimonides: LaSb_2 and NdSb_2	87
6.1	An overview	87
6.2	Synthesis and experimental challenges	90
6.3	The electronic structure	91
6.3.1	The Fermi surface	92
6.3.2	The band dispersion	93
6.4	Features and properties of the electronic structure	97
7	Conclusive Remarks	101
	Bibliography	103

Part I

Introduction

The search for novel physical properties of the condensed matter is at the basis of the research in solid state physics and material science; it allows to explore the fundamental physical principles and provides, at the same time, the ground-work for technological advancement. To this end, the fundamental research on the electronic properties of solids led to some of the greatest technological achievements. Superconductivity, giant magnetoresistance, semiconductor physics are just few examples of condensed matter electronic properties, explored in the past century, that made their way to every-day life applications. Today's state of the art technology in electronics is based on the consolidated knowledge of the physical properties of materials. The job of the solid state research is to push forward the frontiers of knowledge and study new physical concepts and new systems.

The work presented in this PhD thesis is dedicated to the study of electronic properties of some novel materials, in specific the focus is on topological insulators and rare earth diantimonides. Topological insulators (TI) are a new electronic state of matter, discovered in 2007 [9]. In these materials, the bulk is insulating but the surface is conductive. This conductivity is ensured by the presence of spin polarized, massless, robust surface states. This feature is particularly relevant for new spintronic applications where the spin degree of freedom could be used to store and manipulate information without the use of magnetic fields [10]. Moreover TIs are an extremely fertile playground for a variety of exotic physical phenomena such as magnetic monopoles [11], Majorana fermions [2], topological superconductivity [12], and received enthusiastic attention from the scientific community in the last years. In this work we focus on the electronic structure of TIs with particular interest on the electronic modifications under surface transformations and creation of interfaces.

The last part of this thesis is dedicated to the study of the electronic structure of rare earth diantimonides, materials that exhibit unconventional magnetoresistive properties [7] and whose electronic structure was previously unknown.

First an introduction covering briefly the theoretical background necessary to the understanding of the thesis is given, followed by a description of the techniques and instruments used. The second part focuses on the achievements of this work and is dedicated to the description and discussion of the presented results.

Outline of the thesis

Chapter 1 provides a general introduction to the physical concepts of surface electron states, spin-orbit interactions and topological insulators, which represent the theoretical background of this work.

Chapter 2 presents the experimental techniques utilized during the work of this thesis. The main principles of angle resolved photoemission spectroscopy and scanning tunnelling spectroscopy are outlined and we take a brief tour of the instrumentation at SGM3 beamline at the ASTRID(2) synchrotron.

Chapter 3 introduces the experimental bulk band structure of the topological insulator Bi_2Te_3 and compares it with different theoretical models.

Chapter 4 investigates the effect of adatoms on top of topological insulators Bi_2Te_3 and $\text{Bi}_2\text{Te}_2\text{Se}$. Rb adatoms are used to induce an anisotropic two dimensional electron gas with strong spin-orbit splitting on the surface. The state's dispersion is studied

using model $\mathbf{k} \cdot \mathbf{p}$ Hamiltonians. Fe and Ni atoms are used to determine the properties of magnetic adsorbates on the TIs, combining magnetic circular dichroism with photoemission experiments.

Chapter 5 describes the electronic structure at the interface of the heterostructure Bi bilayer/ Bi_2Se_3 , a case of coupling a two dimensional TI with a three dimensional TI.

Chapter 6 introduces the rare earth diantimonides as novel materials for electron correlation and transport studies. The electronic structure of LaSb_2 and NdSb_2 is unveiled with experiments and theory.

Chapter 1

Theoretical background

In solid state, electrons lose the single particle behaviour and they are rather described as an ensemble of particles/waves subject to the rules dictated by the chemistry and the symmetry of the entire solid. The generation, in solids, of collective electronic structures gives rise to an extremely wide spectrum of physical properties, whose discoveries have been milestones in the field of solid state physics. The up-to date knowledge of solid state physics is reported in various literally works and extensive reviews [13, 14]. Here we simply cite the basic concepts useful for the understanding of this work.

A single atom has both core electrons, deep in the energy level spectrum, and valence electrons in the most external shell. The latter are responsible for chemical bonding that leads to the creation of electronic structures in solids. Electron states are described by Bloch wave functions, with form $\Psi_{\mathbf{k}}(\mathbf{r}) = u_{\mathbf{k}}(\mathbf{r}) \exp(i\mathbf{k} \cdot \mathbf{r})$, where $\hbar\mathbf{k}$ is the crystal momentum and $u_{\mathbf{k}}(\mathbf{r})$ has the same real space periodicity as the crystal lattice. Solving the Schrödinger equation

$$\left[-\frac{\hbar^2 \nabla_r^2}{2m} + V(\mathbf{r})\right] \Psi(\mathbf{r}) = E \Psi(\mathbf{r}), \quad (1.1)$$

in the lattice periodic potential $V(\mathbf{r})$ one obtains the energy dispersion of electron states $E(\mathbf{k})$. For each \mathbf{k} vector the energy E has multiple solutions, which correspond to multiple electron bands. When the Schrödinger equation is solved for vanishing potential $V(\mathbf{r})$, the wave function is a simple plane wave $\Psi_{\mathbf{k}}(r) = e^{i\mathbf{k} \cdot \mathbf{r}}$ and the dispersion relation is $E(\mathbf{k}) = \hbar^2 \mathbf{k}^2 / 2m_e$. The free electrons, have parabolic dispersion in reciprocal space, and this is frequently observed for simple metals. When the crystal potential is switched on the solution to Eq. 1.1 can define a finite band gap of forbidden energies where bulk electron states cannot exist. The band dispersion is reshaped from the parabolic behaviour, according to the potential felt in the three dimensions. However it is often possible to employ a quasi-free electron model and describe critical points of the bands approximating to a parabolic dispersion with an effective mass $m^* \neq m_e$.

The whole theory of solid state physics, and in particular the electronic structure is based on the concept of infinite periodicity. This has remarkable success in describing the properties of bulk crystals. But what happens when the periodicity of the system is broken? This situation is far from being unrealistic: defects and dislocation disrupts the crystal periodicity, but the surface of the solid is the most obvious candidate to consider the effect of broken translational symmetry.

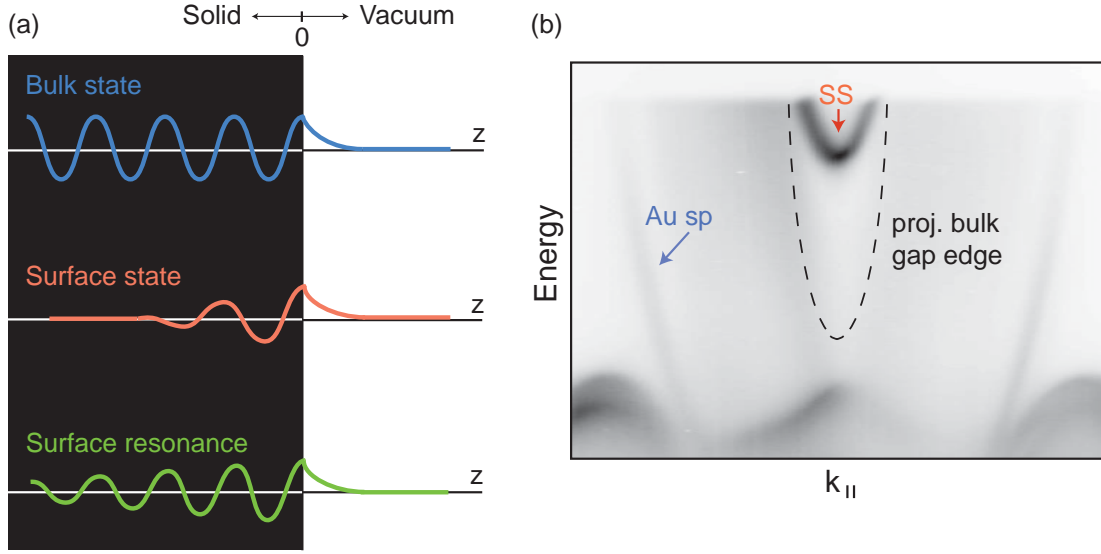


Figure 1.1: (a) Real part of the electron wave functions in the surface region. A bulk state (blue) has Bloch character throughout the solid and decays on the vacuum side. The surface state (red) exponentially decays on both sides of the surface localizing it in two dimensions. A surface resonance (green) is a bulk state whose intensity is enhanced at the surface. (b) Angle resolved photoemission spectrum of Au(111) surface. A parabolic surface state is formed in the projected bulk band gap.

1.1 Electronic structure of surfaces

Introducing the surface in modelling the band structure of a continuous solid is not a trivial task. The pioneering work on surface localized electron states was done by Shockley [15] and Tamm [16]. We can imagine the surface as a sudden step in the electron potential: periodic and negative $V(\mathbf{r})$ in the crystal and $V(\mathbf{r}) = 0$ in the vacuum. The electron wave function, and its derivative, must be matched at the surface with a wave function exponentially decaying in vacuum. The electron is described as a travelling wave with real \mathbf{k} vector inside the crystal which vanishes exponentially in the vacuum side. It must be pointed out that the real value of \mathbf{k} is not a restriction of the Bloch theorem; allowing for a complex \mathbf{k} along the direction perpendicular to the surface (z) such as $\mathbf{k}_{\perp} = \mathbf{k}'_{\perp} \pm i\boldsymbol{\kappa}$ in a Bloch state yields a wave function $\Psi_{\mathbf{k}}(\mathbf{r}) = u_{\mathbf{k}}(\mathbf{r}) \exp(i\mathbf{k}' \cdot \mathbf{r}) \exp(\mp \boldsymbol{\kappa} \cdot \mathbf{z})$. These wave functions, and hence the electron densities, are diverging at $\pm\infty$ and cannot exist in an infinite crystal. However in a semi-finite crystal these solutions assume physical meaning. Let us take the wave function that exponentially decays inside the solid (for example at positive z): on the vacuum side ($z < 0$) the wave function will not diverge because the boundary conditions impose again the match with a decaying function.

The comparison between the real parts of the wave functions for states of different nature is shown in Fig. 1.1(a). The bulk state is a travelling wave inside the bulk that vanishes from $z = 0$ (the surface). The surface state decays both in the bulk and in vacuum, remaining localized close to $z = 0$. A non-zero \mathbf{k}'_{\perp} (the real part of \mathbf{k}_{\perp}) is responsible for maintaining a Bloch-like behaviour of the surface state. The surface localized states (SS) cannot cross the path of the bulk bands since the degeneracy of the two would merge the SS to the bulk travelling wave. Surface states can hence only exist within the projected band

gaps, i.e. energy vs \mathbf{k}_{\parallel} regions where no bulk bands exist at any \mathbf{k}_{\perp} . It is worth to point out that there are few cases where this exclusion criterion does not hold: it can happen that surface states are degenerate with bulk bands if the two states have well defined and distinct symmetries [17]. In the case when the surface state mixes with a bulk band, the state has finite intensity through the whole bulk but is enhanced at the surface. This is the case of the surface resonances shown in Fig. 1.1(a).

The existence of surface states is not an exotic phenomenon. Such states are very commonly found on semiconductor surfaces [18] and in metal projected band gaps [19, 20]. Experimental evidence of a surface state on the (111) surface of gold is reported in Fig. 1.1(b). The parabolic state is well visible within the projected bulk band gap. However the SS existence is somehow precarious, surface reconstruction, defects, chemi- and physisorption are all factors that can destroy the SS.

1.2 Spin-orbit coupling

The spin-orbit interaction is a relativistic effect that acts both at the single atom level and on the electron collective in valence states. It can also have drastic consequences on the band structures of solids. Spin-orbit coupling (SOC) derives from the interaction of the electron spin with its motion (orbital momentum). We can think of this in simple terms: a charged particle with spin \mathbf{S} moves with velocity \mathbf{v} in a static electric field \mathbf{E} . In the reference frame of the particle the moving electric field is perceived as a magnetic field \mathbf{B} through Lorentz transformation

$$\mathbf{B} = -\frac{1}{c}\mathbf{v} \times \mathbf{E} = \frac{1}{mc}(\mathbf{E} \times \mathbf{p}), \quad (1.2)$$

where c is the speed of light and \mathbf{p} is the electron momentum. Higher order terms have been omitted. The particle carries a magnetic moment $\boldsymbol{\mu}_s$ related to its spin. The effective magnetic field exerts a force on $\boldsymbol{\mu}_s$ via the Hamiltonian $H_B = -\boldsymbol{\mu}_s \cdot \mathbf{B}$. This energy term induces a Zeeman-like splitting in energy for particle with spin in a magnetic field. An electron moving in the atomic (or crystal) potential must obey the same rules, giving rise to the spin-orbit coupling.

Taking into account that $\mathbf{E} = -\nabla V$ the spin-orbit coupling Hamiltonian can be obtained directly from the relativistic Dirac equation and assumes the form:

$$H_{SOC} = \frac{\hbar}{4m^2c^2}\boldsymbol{\sigma}(\nabla V \times \mathbf{p}), \quad (1.3)$$

expressing the Pauli matrices for spin as $\boldsymbol{\sigma}$. In the case of a single atom the potential V can be approximated by a spherical potential. The gradient ∇V is proportional to the atomic number to the forth power, Z^4 . The implication here is very important: the SOC becomes stronger for heavier elements. Indeed looking at the periodic table, elements in the first periods effectively show virtually null effect of the SOC, while energy scale of the order of the eV can be found in elements belonging to the last two periods. The spin-orbit Hamiltonian is proportional to the total angular momentum \mathbf{J} . In atomic and molecular physics the SOC splits the electron energy level into two sub-levels with high ($\mathbf{J} = |\mathbf{L} + \mathbf{S}|$) and low ($\mathbf{J} = |\mathbf{L} - \mathbf{S}|$) spin states. This is also true for localized core levels in solids, as outlined in Fig. 1.2. For example a p state will be split into two degenerate levels $p_{3/2}$ and

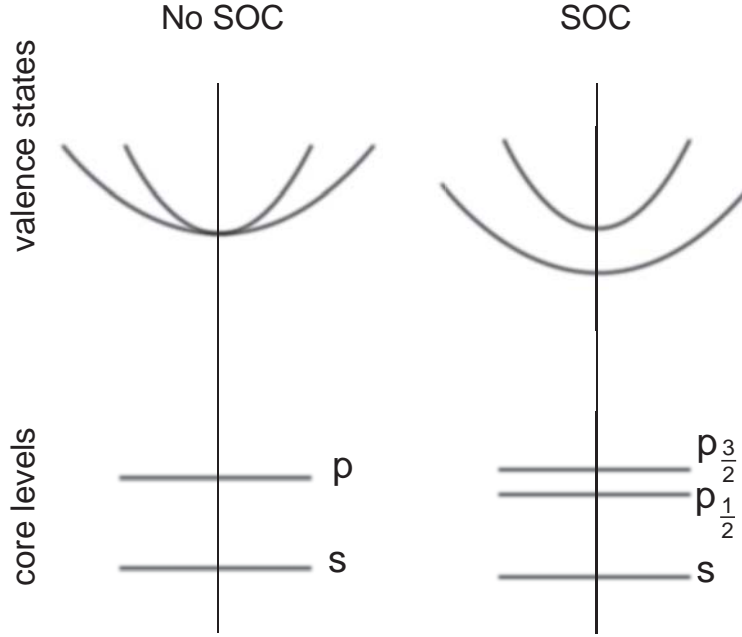


Figure 1.2: Sketch of the effect of the spin-orbit coupling on core level states and valence states. SOC splits p-like core level states and reshapes the valence band dispersion, but does not effect the s- electrons with orbital momentum $L=0$.

one $p_{1/2}$. An s state, on the other hand, cannot be split since it carries orbital momentum equal to zero.

The same spin-orbit treatment is valid for valence electrons, however the manifestation of SOC in valence states can assume different forms. The energy dispersion of the valence states is indeed affected by the spin-orbit coupling, but the creation of spin non-degenerate states is not a trivial task.

1.2.1 Symmetry dependent spin-orbit interaction

To continue with the analysis of SOC in solids, a few symmetry considerations are in order. First we define the time-reversal operator $\Theta = -iS_yK$, K being a complex conjugate operator and S_y the spin operator along y, so that $\Theta H(t)\Theta^{-1} = H(-t)$. When time reversal symmetry (TRS) holds the system is symmetric towards the reversal of all quantities depending on the time in first order, such as velocities and momenta. Normally the system Hamiltonian commutes with Θ meaning that when momenta are reversed the energy eigenvalues from solving the Schrödinger equation will be the same. In practice time reversal symmetry enforces the following condition,

$$E(|\mathbf{k}, \uparrow\rangle) = E(|-\mathbf{k}, \downarrow\rangle). \quad (1.4)$$

States at opposite points in the Brillouin zone (opposite \mathbf{k}) must carry opposite spin direction. In those points of the Brillouin zone where $\mathbf{k} = \mathbf{k} + \mathbf{G}$ (\mathbf{G} being a reciprocal lattice vector) the momentum $\mathbf{k} = -\mathbf{k}$ and Eq. 1.4 requires all states to be spin degenerate. These

points are called time reversal invariant momenta (TRIM). TRS can be broken by a magnetic field. Since the Lorentz force manifests itself as a cross product between particle velocity and B field, the magnetic force is odd under time reversal.

The second symmetry we consider is the inversion symmetry. Many crystals are inversion symmetric in their lattice, and all the materials explored in this thesis are indeed inversion symmetric. From a mathematical point of view the system is inversion symmetric when the parity operator P ($P\Psi(r) = \Psi(-r)$) commutes with the system Hamiltonian. We conclude that for each electron level there must be a degenerate level at the opposite side of the Brillouin zone carrying the same spin

$$E(|\mathbf{k}, \uparrow\rangle) = E(|-\mathbf{k}, \uparrow\rangle). \quad (1.5)$$

It is straight forward to realize that when both conditions hold the degeneracy constraints imposed by symmetry become very strict:

$$E(|\mathbf{k}, \uparrow\rangle) \stackrel{inv}{=} E(|-\mathbf{k}, \uparrow\rangle) \stackrel{trs}{=} E(|+\mathbf{k}, \downarrow\rangle) \stackrel{inv}{=} E(|-\mathbf{k}, \downarrow\rangle). \quad (1.6)$$

Eq. 1.6 goes to imply that electron states are always doubly spin degenerate throughout the whole reciprocal space.

In order to lift the degeneracy at least one of the two symmetries must be broken. The behaviour for a parabolic state under symmetry breaking is sketched in Fig. 1.3. As discussed, one way to achieve this is through the break of TRS, for example with magnetic field or in magnetic materials. Breaking TRS results in two sub-bands carrying opposite spin direction and generating majority and minority spin carriers.

The second way to obtain spin-polarized bands is to break inversion symmetry. This is achieved even in centro-symmetric materials at the surface of the solid. The presence of the surface breaks the mirror symmetry perpendicular to the surface, breaking, *de facto*, the inversion. The theoretical basis of the SOC at surfaces was pioneered by Bychkov and Rashba [21, 22] and is nowadays commonly called Rashba effect. The Rashba Hamiltonian is simply derived from the spin-orbit Hamiltonian in Eq. 1.3. If we assume a quasi-free electron state with effective mass m^* as shown in Fig. 1.3 and take the direction z as perpendicular to the surface, the total Hamiltonian for electrons on the x-y plane is

$$H = H_k + H_R = \frac{\mathbf{p}_{\parallel}^2}{2m^*} + \frac{\alpha}{\hbar}(\boldsymbol{\sigma} \times \mathbf{p}_{\parallel}) = \frac{\hbar^2 \mathbf{k}_{\parallel}^2}{2m^*} + \alpha(\sigma_x k_y - \sigma_y k_x). \quad (1.7)$$

The first term is the kinetic energy and the second is the Rashba Hamiltonian. α is the so called Rashba parameter and is a measure of the strength of the spin-orbit coupling in the system. It comprehends the SOC strength and the electric field strength at the surface. When the Rashba Hamiltonian is applied to the surface state of Fig. 1.3, the band splits into two spin-split sub-bands. The energy splitting is linear in \mathbf{k}_{\parallel} and equal to $\Delta E = 2\alpha|\mathbf{k}_{\parallel}|$. The momentum splitting depends on the band dispersion and for the quasi-free electron case is $\Delta \mathbf{k}_{\parallel} = 2\alpha m^*/\hbar^2$. The two sub-bands are effectively shifted in the momentum direction. The two branches are degenerate at $\mathbf{k}_{\parallel} = 0$ which is a TRIM. To understand the spin texture of a Rashba state, we can go back to the simple image of the effective magnetic field. At the surface the electric field is perpendicular to the surface plane, the electron velocity is normal with respect to the Fermi contour (a circle for a free electron band), hence the magnetic field [Eq. 1.2] is orthogonal to both vectors. The spin

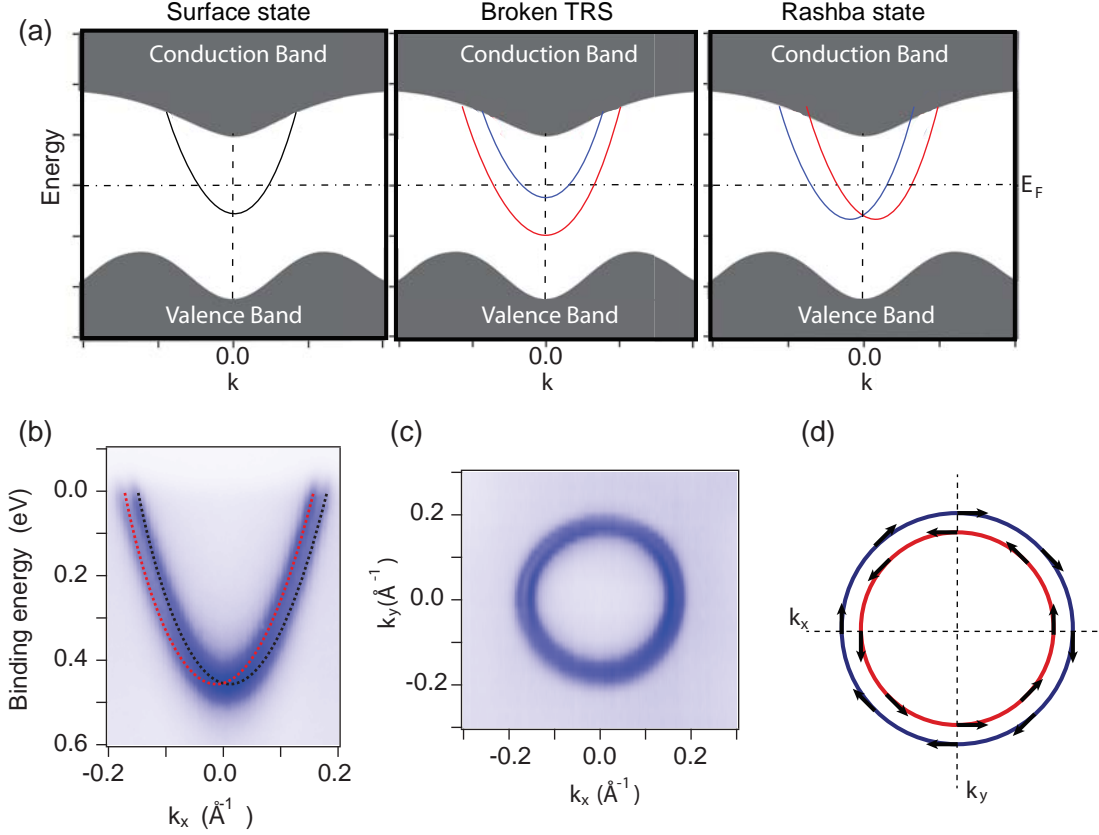


Figure 1.3: Influence of spin-orbit coupling on surface states. (a) Symmetry constrains the effect of the spin-orbit coupling. When inversion symmetry and time-reversal symmetry hold the state is spin-degenerate. The degeneracy is lifted by broken time reversal symmetry, like a magnetic field, or broken inversion symmetry in a Rashba-like state. In the Rashba state time reversal symmetry constrains the degeneracy at the $\bar{\Gamma}$ point. (b) Photoemission spectrum of the surface state of Au(111). The two parabola resemble the Rashba state dispersion. Blue and red lines are a guide for the eye, representing the two branches with opposite spin direction. (c) Fermi surface cut of the surface state of Au(111). Two concentric circles resemble the constant energy contour of the model Rashba state sketched in (d). The spin direction (arrow) is tangential to the contour.

aligns parallel and anti-parallel to the effective B-field creating the spin texture sketched in Fig. 1.3(d). The spin direction is locked to the electron momentum tangentially to the contour.

The Rashba model is a very useful tool in the study of electrons at surfaces. Surface Rashba splitting was first found and investigated on the surface of gold(111) [23], an example is shown in Fig. 1.3(b,c). The dispersion cut and the Fermi surface reveal the existence of the two spin-split sub-bands.

The presence of spin polarized states, especially metallic, is strongly desired for novel spintronic applications, where the spin degree of freedom can be used to process and store information. The aim would be to control the spin degree of freedom without the use of magnetic fields but rather using solely electric switches. The first, and most renowned proposal for such a device is the so called Datta-Das spin transistor, that requires strong Rashba splitting in a two-dimensional channel [24]. It is worth reminding that for non

centro-symmetric systems spin-split states can be obtained without the need of the surface. This was described for Zinc-Blende structures by Dresselhaus [25], but it can also be found in different crystal structures [26, 27].

Further development in the Rashba model requires the integration in Eq. 1.7 of higher order terms in \mathbf{k} . These terms can significantly change the spin splitting and the dispersion of the band as well. Inclusion of higher order terms is further discussed in Chapter 4.2. For a deeper understanding of the Rashba coupling we refer to the many reviews [28–31].

1.3 Topological Insulators

Topological insulators are a class of materials that was recently discovered and classified as a new state of matter [3]. Macroscopically topological insulators are materials insulating in the bulk but conductive on the surface, meaning that, despite their insulating nature, metallic surface states are always found. But this definition is actually quite far from being accurate. The presence of metallic states localized on the surface in semi-conductors is a common phenomenon. The nature of the surface states in topological insulators is of a different nature, and shows exotic properties, such as spin-Hall effect, spin-momentum locking and linear dispersion. The experimental discovery of the first TI in 2007 [9] is only the result of a series of theoretical developments of the model. The discovery of TIs called for a great deal of research in topological insulators, and in new topological states of matter. The theory behind TIs is quite complex. A full, and efficient, description requires to extend the abstract geometrical concepts of topology to the band structure theory of solid state physics. Here, for brevity sake, we will simply cover the main phenomenological aspects and some of the considerations that brought the topological formalism into the materials physics field. For a more thorough description, we can point to some of the many reviews on the topic [1, 2, 32–34].

Topology is a branch of differential geometry that explores the properties invariant under continuous transformations. The entire topological formalism can then be reduced to the study of topological invariants, constants of continuity in a topological space. A physical system is equivalently described by physical invariants that are protected by the system topology. The first discovery of topological invariants in the band structure of a material was found by Thouless *et al.* describing the Quantum Hall Effect [35]. In the quantum Hall effect a two dimensional electron gas under a strong magnetic field and low temperature develops an insulating phase because of the quantization of the density of states into Landau levels. The quantum Hall system develops conductive channels at the edges, described by a quantized Hall conductance. The physical implications of the quantum Hall effect are of extreme interest, because the edge states are chiral in nature and backscattering cannot occur. On the negative side, the quantum Hall effect requires extreme conditions, especially the strong magnetic field, which is undesirable for real-life applications. In 2005 Kane *et al.* proposed that materials with strong spin-orbit coupling could develop a particular form of quantum Hall effect, called quantum spin Hall effect, without the presence of magnetic fields [3]. The idea is that, given the right conditions, chiral states could be developed without breaking time reversal symmetry, and hence without the use of magnetic fields, by having two counter-propagating chiral states that possess opposite spin direction. The 3D quantum spin Hall state of matter was later also named topological insulator.

The necessary ingredients to obtain a TI are two: (1) strong spin-orbit coupling, this

is intuitive because of the need for spin-polarized states, and (2) a band inversion across the band gap. Spin-orbit interaction modifies the band structure, as briefly discussed in Section 1.2. When this interaction is strong it can happen that the energy of valence-like states becomes lower than the conduction-like states leading to an inversion of characters in the bands across the band gap (see Fig. 1.4(a)). For example, we can imagine that the valence band and the conduction band of an insulator will invert their character (like their orbital character) in the point in the Brillouin zone where they are closer to each other. Of course the insulating condition must always be maintained and the gap cannot be closed. Whenever the character inversion happens an odd number of times across the Brillouin zone the material is a topological insulator. In the most general case the band “character” is defined as the time reversal polarization of the occupied bands across the Brillouin zone [1]. The time reversal polarization is basically the difference in charge polarization between spin up and spin down bands. The calculations of the time-reversal polarization can be complex. However, in 2007 it was reported that for centro-symmetric crystals the topological considerations can be greatly simplified by the study of the sole parity eigenvalues of the occupied bands [36].

1.3.1 Definition of a topological invariant

We look now a bit more in detail how a topological invariant is defined in the case of a three dimensional TI with inversion symmetry [36, 37], since throughout this thesis we will only discuss centro-symmetric materials. The topological character of insulators is defined by a \mathbb{Z}_2 invariant called ν . This is calculated from the parity eigenvalues of the occupied bands’ wave functions at the TRIMs. The parity can assume two values: 1 for even and -1 for odd parity. At each TRIM Λ_i the product of the parity eigenvalues ξ of all the occupied bands is calculated as

$$\delta_i(\Lambda_i) = \prod_p \xi_{2p}(\Lambda_i), \quad (1.8)$$

where ξ_{2p} is counting only one of every two spin-degenerate bands. The topological invariant is then determined from the product of the parities at all TRIMs.

$$(-1)^\nu = \prod_{i=1}^{\#\Lambda_i} \delta_i. \quad (1.9)$$

The value of ν can be either 0 or 1. $\nu=0$ indicates that a parity inversion does not occur or it occurs an even number of times. The topology is therefore trivial, this is the case for normal insulators. If $\nu=1$ the insulator is non trivial because the band structure presents a topological “twist” and it is nominally called topological insulator.

Note that the non triviality of the band structure does not carry any useful information *per se* because the system is continuous in its own topological space. The novel electronic properties arise only when two different topological spaces are connected, in the present case a non trivial insulator with a trivial one (such as vacuum). For reasons of continuity, a new state is localized at the interface/surface of the TI in order to connect the two topologies. This state is called topological state (TS) and as a result of the odd topology it must generate an odd number of Fermi contours.

As an example we look at the sketch of the Brillouin zone of tetradymite TIs, such as prototypical topological insulators Bi_2Se_3 , Bi_2Te_3 , $\text{Bi}_2\text{Te}_2\text{Se}$, in Fig. 1.4(b). Eight TRIMs

are identified in the bulk Brillouin zone. The parity value δ_i is -1 for the Γ point but it is even (+1) for all the other TRIMs. We can expect this to be a topological insulator. Moreover projecting the bulk Brillouin zone onto one surface (the (111) surface in this case) the parity values for the surface TRIMs are straight forwardly calculated. Here only $\bar{\Gamma}$ has odd parity and a single topological state is expected on this surface.

The TS in an insulator is always confined in one dimension lower than the bulk. So far we have described three dimensional (3D) systems and the topological properties are detectable in two dimensions, such as surfaces or interfaces [37]. The case of a two dimensional (2D) topological insulator is actually even simpler and all the topological considerations are equally valid, leading to an insulating 2D material with topological 1D edge states, such as the first example of TI in 2007 [9]

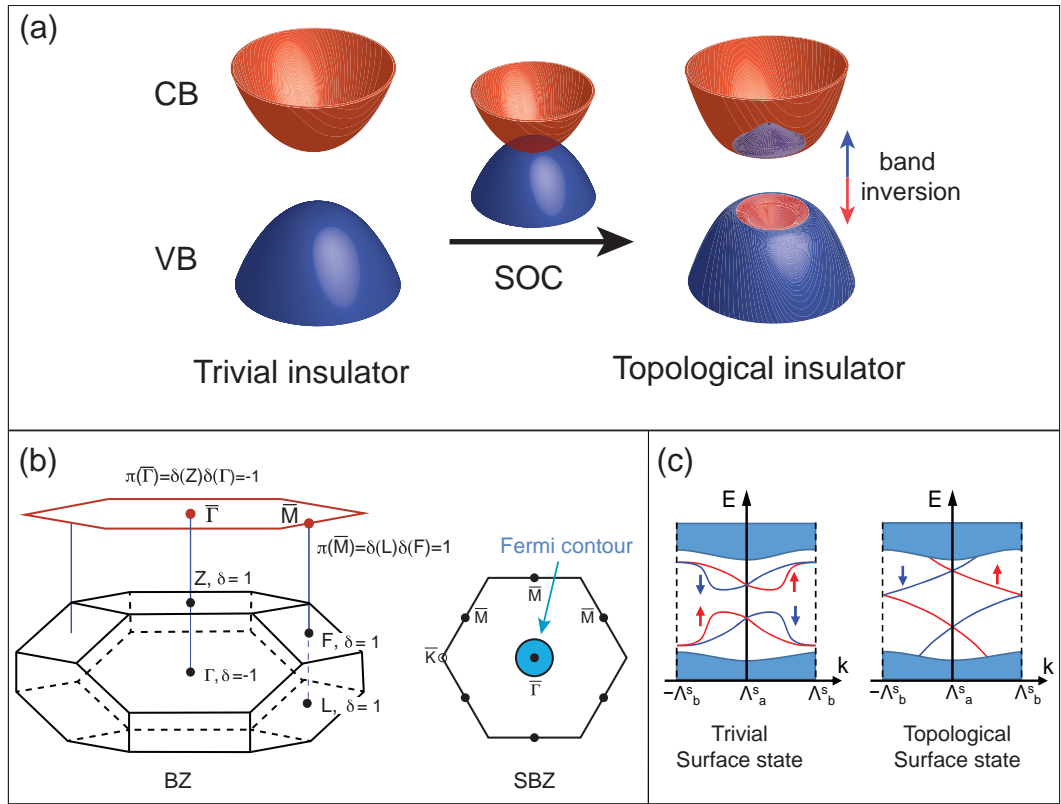


Figure 1.4: (a) Graphic representation of band inversion mechanism in topological insulators. In a trivial insulator the valence band (VB) has “blue” character and the conduction band (CB) “red”. The spin-orbit coupling pushes the two bands across the gap. If the “blue” state assumes lower binding energy than the “red” state a band inversion takes place. When this happens an odd number of times across the Brillouin zone the material is a topological insulator. (b) Projection of a rhombohedral structure Brillouin zone (BZ) onto one surface, high symmetry points are projected as well. This is an example of a strong topological insulator, a single inversion of parity at $\bar{\Gamma}$ leads to the creation of a single Fermi contour. The surface Brillouin zone (SBZ) has hexagonal shape; the high symmetry points $\bar{\Gamma}$ and \bar{M} are surface TRIMs while \bar{K} , at the corners, is not. Adapted from Ref. [38]. (c) Examples of spin split edge states: on the left example of trivial surface state with spin splitting, on the right example of topological state. The trivial surface state can be smoothly deformed but the metallicity is not granted because a gap exists or can be opened. In the case of the topological state as long as the degeneracy at TRIMs is maintained no smooth transformation can undo the Fermi level crossing. After Ref. [1].

1.3.2 A massless surface state topologically protected

It must be noted that the TS is different from other trivial surface states for two main reasons: 1- The topological surface state existence is due to the properties of the bulk and it does not derive from the surface. This makes it robust against surface impurity, disorder or surface reconstructions. 2- The TS derives from a character inversion across the band gap and it is forced to connect the valence band to the conduction band. Given these connectivity considerations the TS must always be metallic (it crosses the Fermi level): Fig. 1.4(c) shows the dispersion and the spin polarization of a trivial surface state, such as a Rashba state, and a TS. Both have spin polarized bands. However, the first generates an even number of closed constant energy contours, any smooth transformation can make it cross the Fermi level or move it away from it. In the case of the topological state, this can never happen because an odd number of Fermi level crossing is granted by topology. A smooth transformation is here defined as a deformation that maintains all the topological premises we imposed: band inversion, band gap and time reversal symmetry. If the time reversal symmetry lacks on the system, the degeneracy at TRIMS is not granted and a gap in the TS can be opened.

A peculiarity of the topological state is its linear dispersion. The linear dispersion of the bands is mathematically described by the Dirac equation $E = \pm c\sqrt{p^2 + m^2c^2}$ for a massless relativistic fermion. The term massless does not refer to a null effective mass, in fact the linear dispersion indicates by definition divergent m^* , but rather to a dispersion similar to the one of the photon. When the TS is two dimensional (for three dimensional TIs) the state assumes the characteristic "Dirac cone" shape of Fig. 1.5(a). The crossing point of the two bands is called Dirac point and has vanishing density of states. The band dispersion is linear as long as the mass term is zero, otherwise a gap is opened.

The other fundamental property of the topological state is the spin helicity (as shown in Fig. 1.5 (a,b)) which means that the two branches of the topological state carry inverse spin orientation and, in first approximation, the in-plane component of the spin is perpendicular to the electron momentum. The spin helicity of the states protects the electrons from backscattering. A non-magnetic impurities cannot impart the momentum to flip the spin of the scattering electron. Because of time reversal symmetry backscattering requires the electron to pass from a state $|\mathbf{k}, \uparrow\rangle$ to a state $|\mathbf{-k}, \downarrow\rangle$ which is a spin-flipping process. Because of the spin polarized states suppressed backscattering the topological insulators are explored for use in spintronic and modern electronics to transport dissipationless spin currents. A constant energy contour of a TS is represented in Fig. 1.5(b). Elastic scattering can still occur in the TS when the scattering angle is lower than 180° because the projected spin directions of final and initial state have a finite overlap. In the case of two dimensional TIs the edge states can carry a true dissipationless spin current (Fig. 1.5(c)) since the backscattering is the only possible event in one dimensional edge states.

A small summary of topological insulators and topological properties is given in the following:

- Insulating materials can be classified according to their band structure topology. A band inversion due to SOC can lead to a non trivial topology. This leads to a topological insulator.
- TIs have TS localized at the surface (edge). The TS is due to the bulk band structure and not to the surface (edge) properties. It is hence robust against surface (edge)

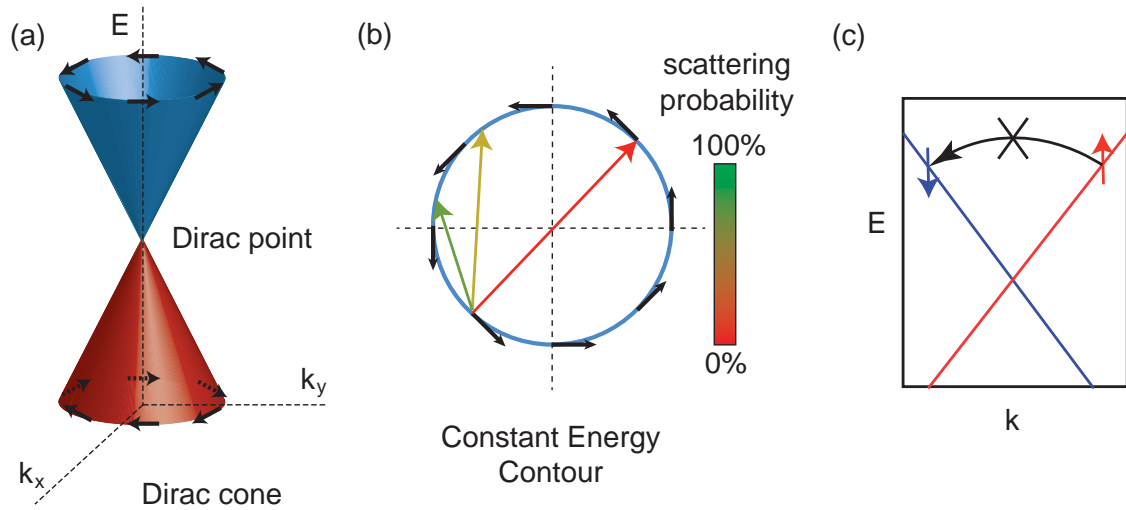


Figure 1.5: (a) Dirac cone topological state in momentum space for 3D TIs. The dispersion is linear and the branches are spin polarized with helical spin texture. (b) Example of a constant energy contour of the 2D topological state. Due to the spin helicity scattering through non magnetic impurity is impossible in the back-scattering geometry (red arrow). It is however possible the scattering at different angles, with probability scaling as $(1 - \cos(\theta))$ (θ is the scattering angle). (c) Schematic dispersion of a 1-D topological state. Opposite branches carry opposite spin (red-blue arrow), the elastic scattering is forbidden.

modifications.

- The TS is spin polarized with chiral spin texture.
- The TS has a linear dispersion (to some extent) and can be treated as describing massless Dirac fermions.
- Backscattering within the TS is forbidden by time reversal symmetry.

1.4 Other Dirac fermions

Topological insulators are not the only materials that show a Dirac-like dispersion of the bands. Graphene was the first material to trigger the interest in relativistic fermions [39]. Similar states are also found in d-wave superconductors [40] and in other topological states of matter such as crystalline topological insulators [41] and Weyl semimetals [42]. The wave-like behaviour of Dirac fermions has opened the gate to a series of new physical phenomena, mostly related to transport properties. In graphene, for example the electron-hole symmetry leads to perfect ambipolar effect and very high carrier mobility. Also, because of their photon-like dispersion Dirac fermions respond differently than other states to external perturbations. Applying a magnetic field perpendicular to the Dirac state surface produces always a zero mode in the Landau level spectrum, a signature of the linear dispersion. A mass term in the Dirac equation, on the other hand, generates gapped insulating states [43]. The linear dispersion also influences the magnetoresistive properties of materials, and it can push the magnetoresistance down to its quantum limit [44]. This point will be discussed in Chapter. 6 studying the case of rare-earth dantimonides. Dirac fermions are a new playground for incorporating relativistic effects into solid-state physics.

Chapter 2

Experimental techniques

2.1 Angle Resolved Photoemission Spectroscopy

Angle Resolved Photoemission Spectroscopy (ARPES) is one of the most used techniques for the study of the electronic structure of materials. The big asset of ARPES is the ability to provide, arguably, the most direct visualization of the electronic band structure. The ARPES technique finds its root in the physics of the photoelectric effect. Discovered by Hertz [45] and later explained by Einstein [46] the photoelectric effect is an exquisite manifestation of quantum mechanics: if a beam of light of sufficient energy is shun on a material its electrons can absorb single photons and get expelled from the solid. The finality of ARPES is to collect the photoemitted electrons and analyse them in terms of energy and emission angle in order to trace back the momentum dependent energy dispersion ($E(k)$) of the electrons inside the solid. Other than a view on the electronic structure of a material, ARPES also takes a peak into the dynamical properties of electrons in solid state. In the following we will describe the basic principles of angle resolved photoemission spectroscopy in solids, and the information that can be extracted from photoemission spectra, as relevant to this thesis. For additional information we refer to the extensive literature on the subjects [47–51].

2.1.1 Photoemission process

The basic principle of the photoemission process in a solid is sketched in Fig. 2.1(a). When a photon of energy $h\nu$ is shone on the sample an electron can be emitted. The energy necessary to extract an electron from the material is equal to the binding energy of the electron inside the solid (E_B) plus the work function Φ . The work function is the energy step that prevents the electrons from escaping the surface. It manifests as an energy offset between the Fermi level of the material and the vacuum level. Typical values for the work function are in the order of 4-5 eV. By energy conservation the kinetic energy of the photoemitted electrons is:

$$E_k = h\nu - E_B - \Phi. \quad (2.1)$$

The binding energy is defined by convention as positive and starts with zero value at the Fermi level. The electrons are collected by a spectrometer that discriminates their energies and counts the individual photoemission events. The photoemission intensity is proportional to the density of states and the kinetic energy can be transformed in binding

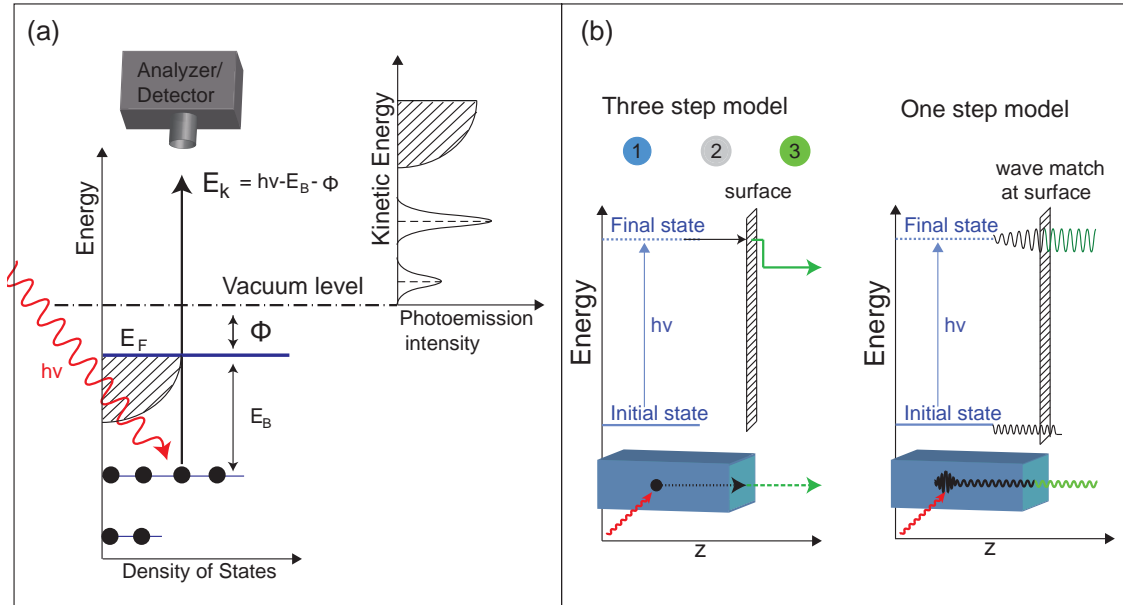


Figure 2.1: (a) Schematics of the energy levels in a photoemission process. A photon with energy $h\nu$ extracts an electron in the material from an energy level with binding energy E_B . The kinetic energy of the photoemitted electron is given by energy conservation. The detection of the photoemitted electrons generates an energy spectrum as a function of kinetic energy. (b) Basic models for the photoemission process: On the left the three step model. The electron is first excited by the photon to a final state, then it travels to the surface and in the end gets transmitted through the surface. On the right the one step model. Quantum-mechanically the photoemission process happens as a simultaneous match of initial state, final state and a vacuum state, mediated by the photonic transition.

energy through Eq. 2.1. Photoemission spectroscopy can only probe occupied electron states. The photoemission process is usually described with two models: the three-step and one-step model. Schematic representations of both are portrayed in Fig. 2.1(b). The former is the most commonly employed to describe the photoemission in solids. The process is outlined in the following three steps: 1) The electron is photo-excited from an initial state $|\Psi_i(E_i)\rangle$ to a final state $|\Psi_f(E_f = E_i + h\nu)\rangle$; 2) the electron travels in the bulk to the surface incurring in eventual scattering; 3) the electron is transmitted through the surface and leaves the solid. The step 1 contains the information about the state of the electron inside the material. In the step 2 the electron has to go through the bulk. This results in possibly single or multiple scattering event(s). If the electron is scattered inelastically, energy and momentum of the initial state (step 1) are changed. Inelastic scattering contributes to the background in the energy spectrum. Instead of talking about scattering cross section, it is common to refer to the inelastic mean free path λ that the electrons can travel on average within the material without being subject to inelastic scattering processes. The mean free path depends on the medium and on the electron kinetic energy. A universal mean free path curve, as shown in Fig 1.11 of Ref. [48], gives a general indication of the energy dependence and order of magnitude for λ . Electrons are strongly interacting particles and the mean free path is rather short. For the energy range used in ARPES (4-100 eV) the mean free path is only few Ångströms, this makes photoemission spectroscopy an extremely surface sensitive technique. Step 3 corresponds to a transmission probability through the surface.

The three step model is the most commonly employed approach and it is very successful, mostly in the description of the bare band energy dispersion. However this model is simplistic in its form. A more accurate quantum-mechanical description requires to define a single one-step process. The transition is described by a finite overlap between an initial state and a final state through an optical transition Hamiltonian. The probability for the transition is given by Fermi's golden rule and has rate w defined as

$$w = \frac{2\pi}{\hbar} |\langle \Psi_f^N | H_{int} | \Psi_i^N \rangle|^2 \delta(E_f^N - E_i^N - h\nu), \quad (2.2)$$

where the initial state is eigenstate of the N-particle system and the final state is eigenstate of the (N-1) electrons ionized system. Moreover, boundary conditions dictate that the final state includes a component in the form of a free electron plane wave in vacuum. The optical interaction Hamiltonian employs a dipole operator in first order time-dependent perturbation as:

$$H_{int} = \frac{e}{2mc} (\mathbf{A} \cdot \mathbf{p} + \mathbf{p} \cdot \mathbf{A}), \quad (2.3)$$

where \mathbf{A} is the vector potential of the electromagnetic radiation and \mathbf{p} is the electron momentum. The one-step model provides the most accurate picture of photoemission, however the description as a unique coherent process is rather complex and the phenomenological three step model is more frequently used.

In the experimental technique of X-ray photoemission spectroscopy (XPS), electrons are emitted from deep lying core levels using photon energies of 200-2000 eV. Values of the binding energy of the core levels are used to extract information about elemental composition and chemical environment of the sample.

Photoemission is an elastic process that must conserve not only the energy but also the total momentum. Knowledge of the momentum of the electrons inside the materials can be retrieved as well. While this might not seem relevant for the study of the core levels, which have no dispersion in momentum space, it can be used in the study of the valence bands. Investigation of the valence bands dispersion is the main purpose of ARPES.

2.1.2 Electron momentum in photoemission

The electrons are emitted at different angles from the surface of the sample, according to their momentum; it is possible to make a measurement of the photoelectrons discriminating their emission angle, this is done in ARPES. The derivation of the photoelectron momentum is not straight forward and requires a few considerations. We examine what happens to the electron momentum in the three-step model, in order to simplify the understanding and outline the main processes. Fig. 2.2(a) shows the \mathbf{k} vectors of the photoelectron inside and outside the solid.

At the initial stage we find an electron with crystal momentum \mathbf{k}^i and a photon with momentum $\mathbf{p} = h/\lambda$. For practical purposes, the momentum of the photon is neglected since it is much smaller than the average value of electron momentum in the solid. This approximation is good for low energy photons, such as typically used in ARPES. However, the effect of the photon momentum cannot be disregarded in case of high-energy ARPES. In step 1 the electron is excited to the final state in the solid. Since we are assuming the optical transition to be vertical in a dispersion plot, the final state momentum must be equal to the initial state momentum plus or minus a reciprocal lattice vector. Simplifying

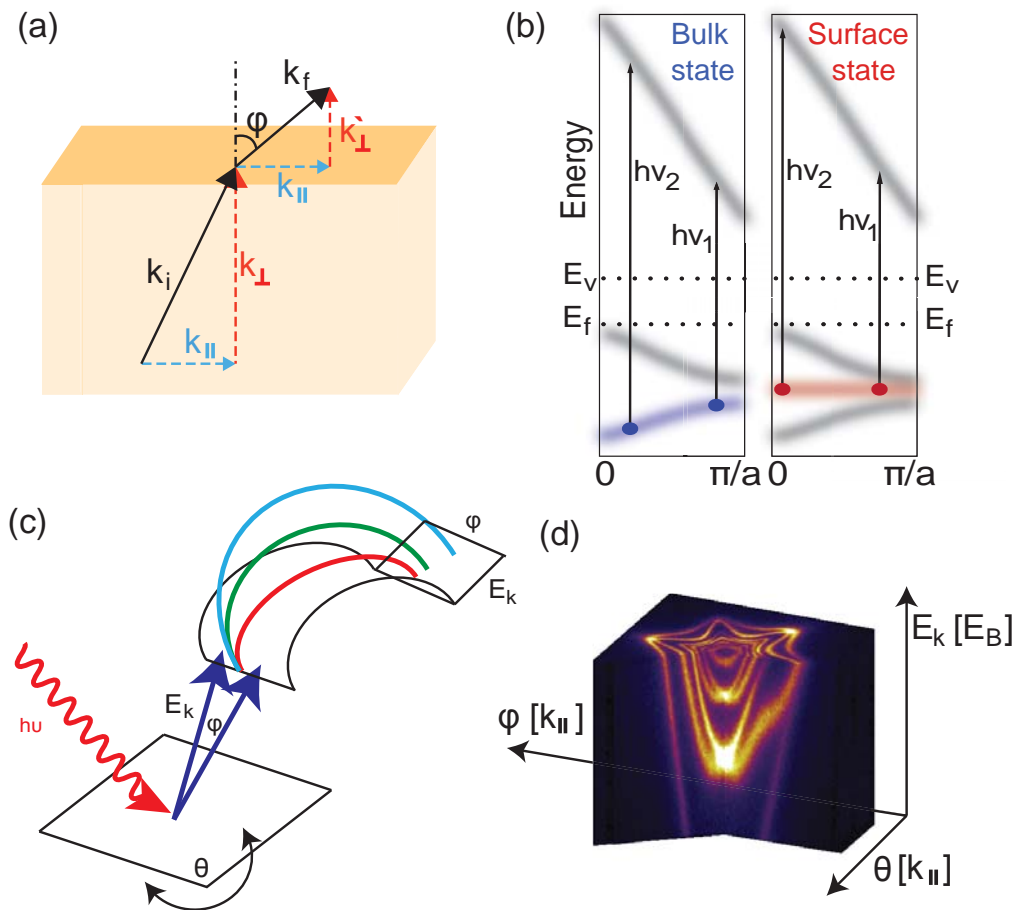


Figure 2.2: (a) Initial and final \mathbf{k} vectors of the photoemission process. The component parallel to the surface is maintained, the perpendicular component is not. (b) Schematics of the photo-absorption process for a bulk state and for a surface state. Only the bulk state shows dispersion with the photon energy. Figure adapted from Ref. [32]. (c) Schematic representation of an ARPES experiment setup. Light is shone on the surface of the sample. Photoemitted electrons are collected and discriminated based on their kinetic energy and emission angle(s). (d) Representation of a three dimensional dataset of ARPES. Intensity is reported as a function of kinetic energy and angles θ and ϕ . Physical information is retrieved when transformed and plotted as a function of binding energy and $\mathbf{k}_{||}$.

the picture in a reduced Brillouin zone scheme we can avoid to track the reciprocal vector(s) \mathbf{G} involved in the process. The final state momentum inside the solid is $\mathbf{k}^{fi} = \mathbf{k}^i$. Step 2 does not influence the electron momentum as long as the electron is not scattered. In step 3 the photoelectron enters in vacuum. At the surface the electron is subjected to a refraction process because of the lack of translation symmetry in the normal direction. Since the translation symmetry at the surface plane is maintained the component of the momentum parallel to this plain is not subject to change and $\mathbf{k}_{\parallel}^f = \mathbf{k}_{\parallel}^i$. On the contrary, the perpendicular component \mathbf{k}_{\perp} is not conserved and $\mathbf{k}_{\perp}^f \neq \mathbf{k}_{\perp}^i$. \mathbf{k}_{\perp} is not even a good quantum number for the system any more because of the destroyed periodicity. The electron in its final state is a free electron in vacuum and from simple geometrical consideration, it is easy to see that in two dimensions

$$\mathbf{k}_{\parallel}^f = \sqrt{2mE_k/\hbar^2} \sin(\phi) \text{ and } \mathbf{k}_{\perp}^f = \sqrt{2mE_k/\hbar^2} \cos(\phi), \quad (2.4)$$

where ϕ is the angle between the trajectory of the photoemitted electron and the surface normal.

Considering Eq. 2.4, we can notice that the dispersion of the state is affected by the photon energy. Let us take a measurement at normal emission, where the spectrometer looks along the sample surface normal. Here $\theta = 0$ and thus $\mathbf{k}_{\parallel} = 0$. Changing the photon energy, and thence the kinetic energy, does not alter \mathbf{k}_{\parallel} . On the other hand the \mathbf{k}_{\perp} depends on the kinetic energy and the photon energy used. These relation provides a good way to distinguish between two dimensional and three dimensional states. The dispersion of a generic initial state and a final state in \mathbf{k}_{\perp} is sketched in Fig. 2.2(b): the surface state, does not disperse in \mathbf{k}_{\perp} due to its two-dimensionality. Utilising different photon energies to probe the 2D band results always in the same binding energy. In the case of a three dimensional bulk state, photons with different energies probe states at different \mathbf{k}_{\perp} and the observed binding energy varies. Moreover, the ill-defined \mathbf{k}_{\perp} carries an uncertainty which is reflected as a spectral broadening of the band, making the bulk bands usually broader than surface states. While this is a convenient way to distinguish bulk and surface states, it must be remembered that at times bulk states have zero or little \mathbf{k}_{\perp} dispersion, especially in layered materials, and could be misinterpreted as surface states.

From a practical point of view, to reconstruct the band structure of a solid the photoelectrons are collected along, at least, two angles. An electron analyser discriminates the electrons according to their energy and emission angles and a 3D intensity map of $(E_k(\theta, \phi))$ is built, as sketched in Fig. 2.2(c,d). Finally, through some geometrical considerations and the mentioned $\mathbf{k}(\theta, E_k)$ relations, the map is converted in $(E_B(\mathbf{k}_{\parallel}))$. Details on the conversion from a real dataset are given in Section 2.1.4. The dispersion of 2D states can be completely investigated with this method. For 3D bulk states knowledge of the \mathbf{k}_{\perp} dispersion of the state must be retrieved varying the photon energy. The final \mathbf{k}_{\perp}^f is known from Eq. 2.4 but, as mentioned, this does not correspond to the \mathbf{k}_{\perp}^i inside the solid.

To quantify the \mathbf{k}_{\perp} after the transmission through the surface, we need to make some assumption on the final state inside the solid. The assumption often made is the one of a free electron final state. In this case the electron dispersion is

$$E^f(\mathbf{k}) = \frac{\hbar^2 \mathbf{k}^2}{2m} - |E_0| = \frac{\hbar^2 (\mathbf{k}_{\parallel}^2 + \mathbf{k}_{\perp}^2)}{2m} - |E_0| = E_k + \Phi, \quad (2.5)$$

where E_0 is the bottom of the valence band. Inserting \mathbf{k}_{\parallel} from Eq. 2.4 one obtains:

$$\mathbf{k}_{\perp} = \frac{1}{\hbar} \sqrt{2m(E_k \cos^2(\theta) + V_0)}, \quad (2.6)$$

with $V_0 = |E_0| + \Phi$ being the inner potential, the energy of the bottom of the valence band referred to the vacuum level. V_0 is the only unknown parameter. Several ways can be employed to find the correct value. From an experimental point of view it is often easier to find V_0 by recursive method. One can identify the high symmetry points in the dispersion in photon energy, whose distance in \mathbf{k} -space is known. Eq. 2.6 is then used employing V_0 as a free recursive parameter until the distance between the two high symmetry points equals the calculated one [52]. This approach is widely used and allows for a good identification of the \mathbf{k}_{\perp} dispersion, even when the assumption on the final state is not necessarily correct.

2.1.3 Spectral shape and quasi particle effects

The photoemission spectrum not only provides information about the band structure of the material but it can also give an insight in the many body effects inside the solid, opening the gate to the vast world of solid state quasi particles. We owe this to the interaction that the photoemitted particle has with its surroundings. Every time the electron is ejected a photoelectron/photohole pair is generated and the system is left behind in a perturbed state. In order to understand how to quantify many-body interactions in the system, we need to look at the expression of the photoemission intensity.

The photoemission transition probability can be described via Fermi's golden rule as expressed in Eq. 2.2. We make now the assumption that, in the time it takes to the electron to escapes the crystal, the system do not relax; this is called *sudden approximation*. This assumption is not necessarily valid but strongly simplifies the problem. Its validity holds better for high energy photoelectrons. We can now write final and initial states as $\Psi_{f(i)}^N = K \phi_{f(i)}^{\mathbf{k}} \Psi_{f(i)}^{N-1}$. K is an antisymmetry operator, Ψ_f^{N-1} is the final state wave function of the system left with $N-1$ electrons and ϕ_f is the wave function of the photoelectron with momentum \mathbf{k} . The initial state is factorized into the one electron orbital $\phi_i^{\mathbf{k}}$ and the remaining $(N-1)$ term $\Psi_f^{N-1} = c_{\mathbf{k}}^- \Psi_i^N$ where $c_{\mathbf{k}}^-$ is the electron annihilation operator. The intensity of the ARPES signal is expressed as

$$\begin{aligned} I(\mathbf{k}, E_{kin}) &\propto w_{f,i} \propto \\ \sum_{f,i} | \langle \phi_f^{\mathbf{k}} | H | \phi_i^{\mathbf{k}} \rangle |^2 &\sum_m | \langle \Psi_m^{N-1} | c_{\mathbf{k}}^- | \Psi_i^{N-1} \rangle |^2 \delta(E_{kin} + E_m^{N-1} - E_i^N - h\nu) = \\ &= \sum_{f,i} |M_{f,i}^{\mathbf{k}}|^2 \sum_m |s_{m,i}|^2 \delta(E_{kin} + E_m^{N-1} - E_i^N - h\nu) = \\ &= \sum_{f,i} |M_{f,i}^{\mathbf{k}}|^2 * \mathcal{A}. \end{aligned} \quad (2.7)$$

$M_{f,i}^{\mathbf{k}}$ is defined as the single particle matrix elements while $|s_{m,i}|^2$ is the probability to remove an electron from the i -st state leaving the system in the excited state m . The matrix elements $M_{f,i}^{\mathbf{k}}$ are responsible for the intensity modulation of the ARPES features and depend on the energy and polarization of the photon other than on the electron states. \mathcal{A} is the so called spectral function and incorporates the sum over all possible states of

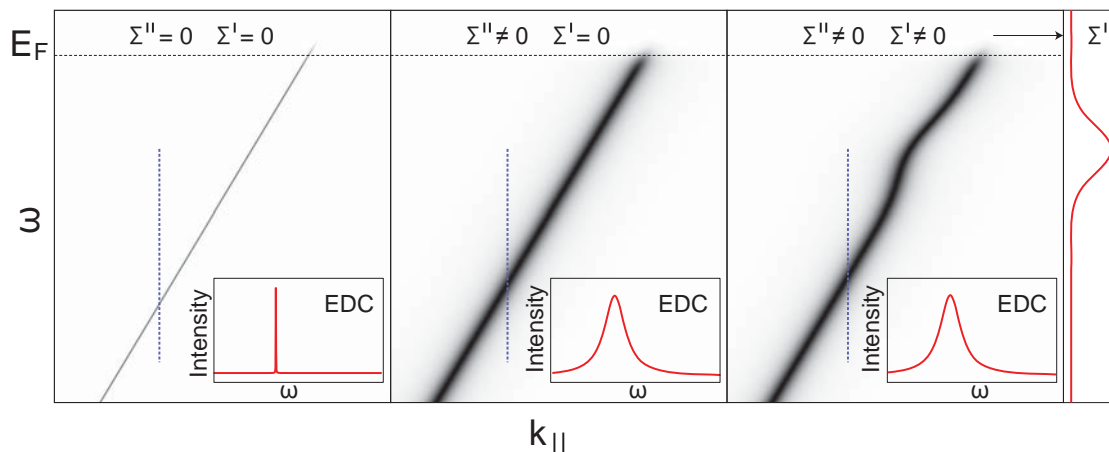


Figure 2.3: Effect of the self energy on the spectral function of a linearly dispersing band. On the left: model spectral function where the self energy tends to 0, the dispersion is just a single line. The Energy Distribution Curve (EDC) shown in the inset is taken along the blue dashed line. The profile tends to a Dirac function around the value of the bare energy $\epsilon(\mathbf{k})$. In the middle: The imaginary part of the self energy is set to a finite value, while the real part is set to zero. The dispersion is again equal to the bare energy but the spectral feature is broadened by Σ'' and the EDC assumes a Lorentzian shape peaked around $\epsilon(\mathbf{k})$. On the right: Σ'' has finite value and Σ' has the arbitrary Gaussian shape shown on the right side. The effect of the real part of the self energy is to renormalise the energy dispersion with an offset equal to Σ' . Note that this is a simplified example with arbitrary values, Σ' and Σ'' are actually related by Kramers-Kronig transformations and when Σ' depends on ω the same is true for Σ'' .

excitation; the energy conservation is expressed by the Dirac delta. For a single non-interacting particle the sum over all possible final states m is reduced to the only term where $\Psi_m^{N-1} = \Psi_i^{N-1}$, leaving a single delta function around the electron binding energy. This is not the case when many-body effects play a role [47]. The photoemission is probing not only the electron but also the photohole state left behind. The overlap integral $|s_{m,i}|$ assumes finite values for the many eigenstates m , resulting in a broadening of the lineshape. The spectral function in Eq. 2.7 can be expressed according to the Green function formalism of many-body systems. Considering the one-electron Green function $G(\mathbf{k},\omega)$ it can be derived that $\mathcal{A} = -(1/\pi)\text{Im}G(\mathbf{k},\omega)$ with electron energy $\hbar\omega$. The spectral function formula can be rewritten in terms of a self energy, leading to the convenient expression

$$\mathcal{A}(E, \mathbf{k}) = \frac{1}{\pi} \frac{|\Sigma''(\omega, \mathbf{k})|}{[\omega - \epsilon(\mathbf{k}) - \Sigma'(\omega, \mathbf{k})]^2 + \Sigma''(\omega, \mathbf{k})^2}. \quad (2.8)$$

Here we express the real and imaginary part of the self energy as $\Sigma'(\omega, \mathbf{k})$ and $\Sigma''(\omega, \mathbf{k})$ respectively and the single particle dispersion $\epsilon(\mathbf{k})$.

The picture here is the one of a particle of (bare) energy $\epsilon(\mathbf{k})$ which becomes “dressed” with a self-energy caused by the interaction with the environment. The “dressed” particle can be treated as a single quasi-particle. To understand the role of the self energy on the spectral features we look at Fig. 2.3 where the same model band with linear dispersion is shown in three different cases. For a non-interacting system both contributions to the self-energy are vanishingly small and the band looks like a simple line. The intensity profile along the cut shown with a blue line is plotted in the inset. This is a simple delta function as discussed previously. By adding a finite $\Sigma''(\omega, \mathbf{k})$, the spectral feature is

broadened. The shape is a Lorentzian peaked around the bare energy $\epsilon(\mathbf{k})$. The full width half maximum (FWHM) is equal to $2\Sigma''(\omega, \mathbf{k})$ [53]. $\Sigma''(\omega, \mathbf{k})$ and the spectral width are inversely proportional to the lifetime of the state, the broader the feature the shorter the lifetime. The imaginary self-energy contains contribution from electron-electron, electron-phonon and electron-impurity interactions. When a finite real part of the self energy, shown in Fig. 2.3 on the right having an arbitrary Gaussian profile in energy, is added to the system, the dispersion (and with it band velocity, curvature etc..) is changed respect to the bare energy. $\Sigma'(\omega, \mathbf{k})$ acts as an offset in the peak position renormalizing the particle dispersion into the quasi-particle one. This usually translates into kinks of the dispersion as seen for graphene, high temperature superconductors and many others [53–57]. Real and imaginary part of the self-energy are actually not independent but they are related to each other through the Kramers-Kronig relation.

2.1.4 Acquiring and analysing ARPES Data

Experimentally, ARPES is performed in ultra high vacuum (UHV) chambers. The vacuum conditions are necessary to maintain the sample surface in a “clean” state, meaning that the amount of adsorbate and contamination must be minimized at the surface. Furthermore the electron trajectory in vacuum is usually several centimetres long and UHV is required to prevent electron scattering in the rest gas, as well as UV-light absorption. The ARPES setup requires the following three components: a light source, a sample and an electron analyser with a detector. The source provides high brilliance and monochromatic light. Discharge lamps and laser light are commonly used in laboratories; both provide radiation in the low UV range. The downside of these sources is the impossibility to tune the photon energy. To solve this problem, the use of synchrotron radiation is necessary.

The sample must satisfy strict conditions as well: the sample must be a single crystal and the surface must be “clean” and flat. The presence of multiple domains mixes different emission angles in a single trajectory, potentially erasing any information about the crystal dispersion. The surface must contain minimum amount of adsorbates, steps and defects that can scatter the outgoing photoelectrons. Imperfections of the surface result in increased background in the spectrum. In order to have a clean surface the sample must usually be treated after being inserted in the vacuum chamber to remove contaminations from exposure to air. Standard methods to clean the surface are annealing, sputtering the surface with energized ions and in vacuum cleaving. Cleaving removes a layer of material from the top of the sample exposing a brand new surface. When done in UHV the new surface will only experience UHV atmosphere. For samples that can exfoliate very easily the scotch tape technique might be used, where a simple piece of scotch tape is attached to the sample surface in such a way that it can later be removed inside the vacuum chamber. When removed, some layers of material are cleaved away resulting in a shiny surface. An other employed method is the top-post technique. A small post of ceramic or metal is glued on top of the sample surface; this is later knocked out in vacuum. If the bond to the glue is stronger than the inter-layer bonding strength, the sample is cleaved.

The photoemitted electrons are collected by an analyser. The task of the analyser is to discriminate the electrons based on their kinetic energy and angle of emission. At the end of the analyser a detector is placed to count the single electronic events. Different types of analyser are on the market with specific properties. The most widely used, and the one used throughout this thesis, is the hemispherical analyser.

map of the dispersion inside the crystal or a Fermi surface, the sample must be rotated by a second angle orthogonal to ϕ . In this geometry the sample can be rotated along a second angle, θ , to acquire a, so called, angular scan. Concatenating $E_k(\phi)$ images for different θ angles, a 3D map is constructed. The angles must be transformed in the reference frame of the analyser and the momentum relations for this geometry are defined as:

$$k_x = \sqrt{\frac{2mE_k}{\hbar^2}} [\cos(\alpha) \sin(\phi) - \sin(\alpha) \cos(\phi) \cos(\theta)], \quad (2.9a)$$

$$k_y = \sqrt{\frac{2mE_k}{\hbar^2}} \cos(\phi) \sin(\theta). \quad (2.9b)$$

If the ARPES system is placed at the end of a beamline it is possible to perform “energy scans” where the photon energy is varied instead (or in addition to) the θ angle. With the energy scan is possible to reconstruct the dispersion along the component of the momentum perpendicular to the surface, as explained in Section 2.1.2.

Looking at the ARPES image is useful for understanding the band structure from a qualitative point of view. For a more quantitative analysis a useful approach is to take intensity line profiles. Profiles taken along the energy direction with constant \mathbf{k} are commonly called Energy Distribution Curves (EDC); lines in the momentum direction at constant energy are called Momentum Distribution Curves (MDC). For weakly interacting systems the intensity of a 2D ARPES spectrum along the energy direction has the shape of a Lorentzian (the spectral function) convoluted with a Gaussian profile derived from the instrumental resolution,

$$I(\omega, \mathbf{k}) \propto A(\omega, \mathbf{k}) |M_{f,i}^{\mathbf{k}}|^2 f(\omega) \otimes G(\Delta\omega) + B(\omega), \quad (2.10)$$

where $M_{f,i}^{\mathbf{k}}$ are the intensity matrix elements derived from Fermi golden rule, $f(\omega)$ is the Fermi-Dirac function, $G(\Delta\omega)$ is the Gaussian energy resolution and $B(\omega)$ the background. In the presence of strong kinks in the dispersion, in strongly interacting systems, the EDC profiles displays satellite features due to the presence of the excited states created in the photoemission process [47]. The intensity profile along the momentum directions is always the one of a Lorentzian, whose width depends on the EDC width and the band dispersion (its slope), convoluted with the angular resolution Gaussian. The momentum resolution depends both on the angle and energy resolution. The distribution curves might be fitted with Voigt profiles plus a background to obtain the spectral feature parameters. Tracing the peak location allows to quantify the band dispersion. Width and intensity provide information on lifetime and matrix elements effects.

2.1.5 The beamlines: SGM3 at ASTRID and ASTRID2

The ARPES experiments presented in this thesis have been acquired at the SGM3 beamline at Aarhus SStorage RIng in Denmark (ASTRID) and ASTRID2. The experiment described in Chapter 4 is performed at the i05 beamline at Diamond light source.

A synchrotron is a particle accelerator where particles are forced to circulate in a loop. In synchrotrons used for radiation production bunches of electrons are injected and accelerated in the storage ring. Here the particles can be further accelerated and maintained at fixed energy. Every time the electron passes through a magnetic field its trajectory bends and electromagnetic radiation is produced. The electron energy is restored thanks to radio

frequency cavities placed along the ring while the radiation is collected in beamlines where it is monochromatised and delivered to the experimental end station.

ASTRID is a small low energy synchrotron in Aarhus University. The electron energy in the ring is 580 MeV, the electron current is up to 200 mA. In the year 2014 a new ring ASTRID2 was commissioned and the beamlines were moved to the new synchrotron. ASTRID is still in use as a booster ring that pre-accelerates electrons and feeds ASTRID2 with top-up injections. ASTRID2 improved the performance respect to ASTRID in terms of lifetime and emittance, effectively reducing the beam spot size [59]. The components of the SGM3 beamline at ASTRID and ASTRID2 are similar, a drawing of the beamline in ASTRID2 is shown in Fig. 2.5. The insertion device is an undulator, a series of coupled magnets that force the electron in a “zig-zag” trajectory creating coherent polarized light. The light is focused via a set of mirrors and slits and monochromatised by a spherical grating mirror. A last toroidal mirror conveys the light in the end station and, ultimately, on the sample. The photon energy from the beamline can be varied from 14 eV to 150 eV.

The experimental end-station at SGM3 also underwent major developments during the synchrotron upgrade. The end station at ASTRID was composed of two major vacuum chambers, a Preparation chamber (PC) and a main chamber (MC). The PC design is optimized for sample treatment: Ar/Ne sputter guns are used to clean the sample surface, a mass spectrometer used to analyse the rest gases. An horizontal manipulator can hold and transfer the samples and it hosts a cooling stage as well as a tungsten filament for electron bombardment, it covers a temperature range of 140-1600 K. Evaporators can be placed in the chambers for sample growth or surface doping. The MC hosts Low Energy Electron Diffraction (LEED) optics for surface structure analysis, and a commercial electron hemispherical analyser SPECS Phoibos 150, used for photoemission. The light enters from the beamline and hits the sample held in place by a vertical manipulator equipped by a close cycle cryostat and a heating filament as well. The manipulator has five axis, the polar angle is motorized to make angular scans while translational axis and the tilt are operated manually (see Fig. 2.5(d)). After the upgrade to ASTRID2 the end station (Fig. 2.5(c)) has been equipped with an additional chamber on the opposite side of MC, optimized for MBE growth. This chamber is furnished with a set of electron beam epitaxy (EBE) evaporators on the bottom, as well as gas lines, a heating stage and a reflection high energy electron diffraction (RHEED) setup used to control thin film growth. Moreover in the PC a Aarhus-style scanning tunnelling microscope (STM) [60] is mounted. The combination of all these surface technique allows for growth, structural and electronic characterization of samples.

The sample plates used are rigid tantalum or molybdenum plates with the shape shown in Fig. 2.5(e). Depending on the kind of sample, samples are either fixed with clips and stripes or glued with conductive epoxy glue. A thermocouple is mounted on the back of the plate for an accurate determination of the temperature.

2.2 Scanning tunnelling microscopy and spectroscopy

Scanning Tunneling Microscopy (STM)/ Spectroscopy (STS) is one of the most exploited techniques in surface science, very well known for the ability of acquiring images of single atoms. Its potential goes way beyond the simple surface topography: STM/STS provides real space information of the electron density of states at a very local level. Moreover it

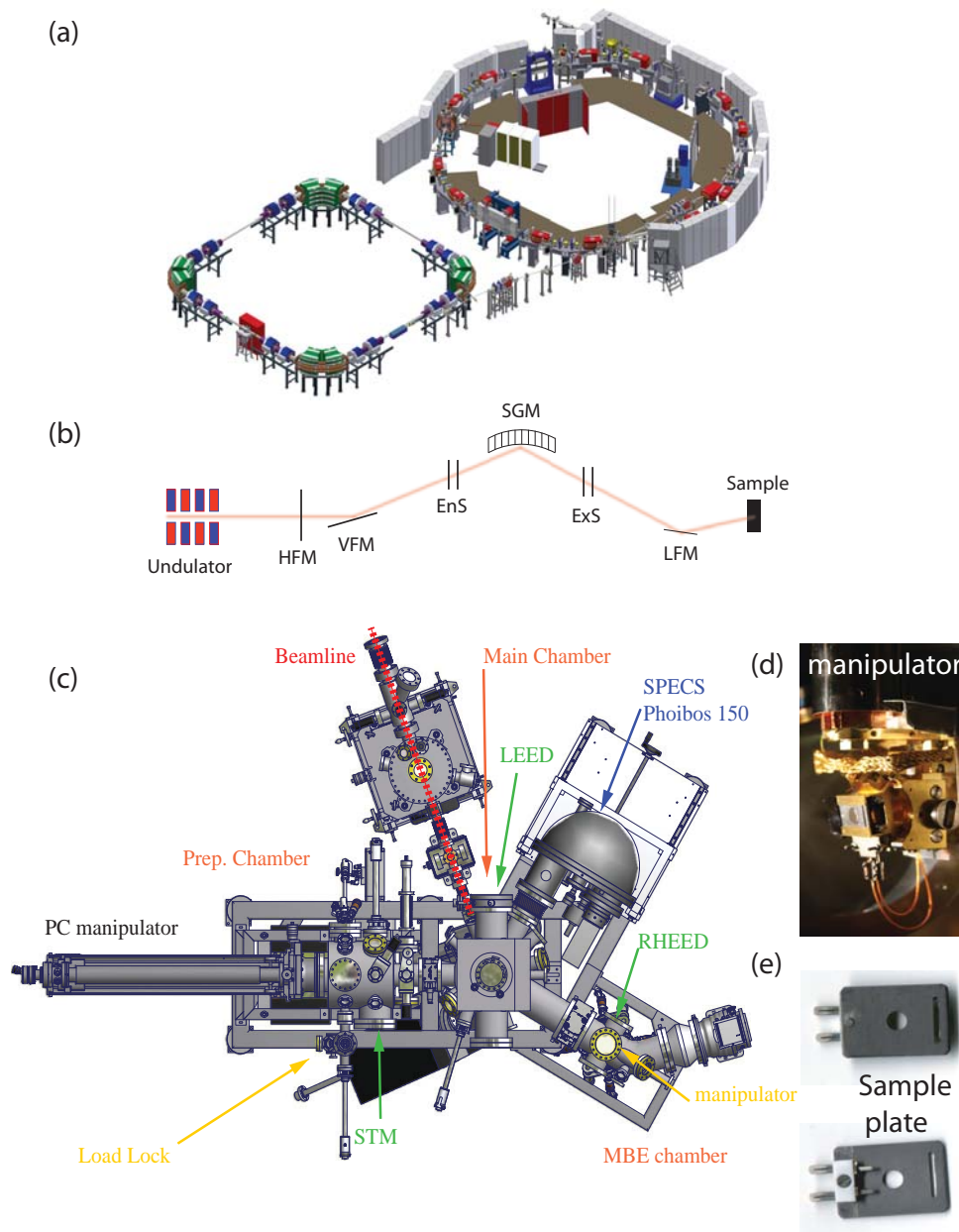


Figure 2.5: (a) Design of the synchrotron facility at Aarhus university. The smaller square-shaped ring (ASTRID) functions as booster ring for ASTRID2. (b) Schematics of the SGM3 beamline: the insertion device is an undulator, the light is focused and directed by an horizontal focusing mirror (HFM) and a vertical focusing mirror (VFM) through the entrance slit (EnS). The radiation frequency is selected by the monochromator (SGM) and directed through an exit slit (ExS) on the toroidal last focusing mirror (LFM), where it is reflected onto the sample. (c) Experimental setup of the end-station at the SGM3 beamline. The system revolves around three main vacuum chambers. LEED, RHEED, STM, EBE evaporators, a mass spectrometer and a SPECS Phoibos 150 electron analyzer allow for a thorough investigation of sample surfaces. (d) Photo of the 5-axis manipulator in the main chamber. (e) Photos of the sample plates used at the end station. A thermocouple is mounted on the back.

can also provide magnetic, vibrational and chemical information.

An atomically sharp tip is approached close to the sample surface (few Å distance), a voltage is applied between the sample and the tip, electrons can tunnel across the potential barrier and a tunnelling current is recorded. Electrons tunnel from/to the tip to/from the sample with finite probability of transmission $T \propto \exp -2k'L$. L is the space between sample and tip and $k' = -i\sqrt{2m(E - V_p)/\hbar^2}$ with potential barrier $V_p > E$. The tunnelling current is hence proportional to the tip-sample distance and thus to the surface height, allowing to indirectly record topographic information. A full description of the tunnelling process requires full knowledge of the state of the sample and of the tip. The tunnelling current I is expressed as

$$I \propto \int_0^{eV} \rho_t \rho_s(E, r_0) |M_{t,s,z,E}|^2 dE, \quad (2.11)$$

where E is the electron energy and ρ is the density of states (for tip and sample). The exponential decay is hidden in the Matrix elements $|M_{t,s,z,E}|$. In Fig. 2.6(a) the tunnelling

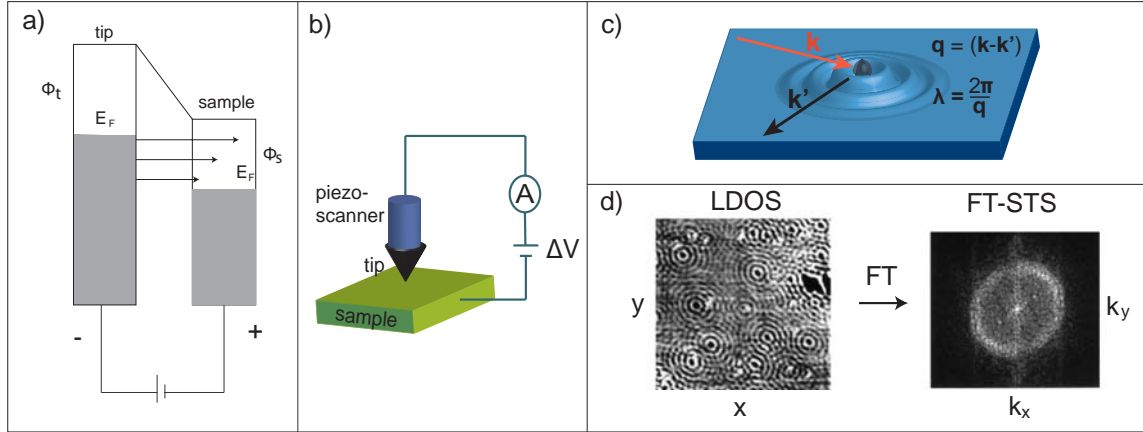


Figure 2.6: (a) Schematics of the tunneling process between tip and sample. Electrons can tunnel from the metal negatively biased to the metal positively biased (b) Schematic of the setup of an STM: an atomically sharp tip is scanned on the surface of the sample thanks to a piezo-scanner. The tunnelling current is recorded as a function of (x,y) position. (c) Quasi particle interference on the surface. An electron with momentum \mathbf{k} scatters on an impurity into a state with momentum \mathbf{k}' with scattering vector \mathbf{q} . The two electron waves interfere creating a modulation of the LDOS around the impurity. The wavelength of the modulation is $\lambda = 2\pi/q$. (d) Differential conductance map of the copper surface, performing the Fourier transform passes from the real space to the \mathbf{k} space of scattering vectors. Images from Ref. [61].

mechanism is shown. When the bias imposed on the sample is positive the electrons tunnel from the tip to the sample, while, if the bias is negative, the direction is inverted.

The tip can be moved on top of the surface to record a 2D image of the tunnelling current as a function of real space coordinates. As schematic representation of the experimental setup is sketched in Fig. 2.6(b). The tip has three translational degrees of freedom, it is moved by a piezoelectric scanner in the x,y plane and on the vertical z -direction. The piezo-scanner allows ultra precise movement controlled by a simple voltage. The tunnelling current is used in a feedback loop with the z -piezo to adjust the vertical position. The STM is mainly run in constant current mode (recording $z_{V,I}(x,y)$) and constant height mode (recording $I_{z,V}(x,y)$).

The STM does not detect the atoms per se but the local electron density of states (LDOS). This means that the topographic information (which is given by the tip-sample distance) is superimposed onto a purely electronic one.

In order to obtain more detailed knowledge about the electronic structure utilizing the STM setup, scanning tunnelling spectroscopy is employed. To record the LDOS at finite energy, LDOS(E), the differential conductance must be recorded. By differentiating the intensity from Eq. 2.11 at constant energy $E = e \cdot V$ and assuming ρ_t to be constant we obtain

$$\left. \frac{dI}{dV} \right|_{eV} \propto e \rho_s(eV) |M_{t,s,z,eV}|^2 + e \int_0^{eV} \rho_s E \frac{d(|M_{t,s,z,E}|^2)}{dV} dE. \quad (2.12)$$

The first term is directly proportional to the sample LDOS while the second depends on the variation of tunnelling probability with the energy. The effect of the second term is usually minimized by plotting the results in terms of $(dI/dV)/(I/V)$ vs V [62, 63].

Differential conductance maps are acquired by recording the dI/dV signal over a wide region. This is a map of the LDOS(E). Most frequently the spectra are recorded at the same time as the topography by imposing a high frequency oscillating voltage signal; the corresponding current signal in phase with the voltage is then filtered by a lock-in amplifier.

If the surface presents some defects or steps the LDOS maps can manifest the so-called Quasi-Particle Interference (QPI) effect: When an electron travelling on the surface of the material is scattered by an impurity the electron wave of the incoming electron can interfere with the outgoing particle creating a Friedel-like modulation in the local density of states that appears like “ripples” in the LDOS signal (see Fig. 2.6(c)).

More formally: The local density of states is

$$LDOS(E_0) = \sum_k |\Psi_{\mathbf{k}}(\mathbf{r})|^2 \delta(E - E_0), \quad (2.13)$$

where $\Psi_{\mathbf{k}}(\mathbf{r}) = u_{\mathbf{k}} e^{i\mathbf{k} \cdot \mathbf{r}}$ is the Bloch wave function at \mathbf{k} . When the Bloch electron is scattered it goes from a state $|\mathbf{k}\rangle$ to a state $|\mathbf{k}'\rangle$. the resulting wave function will be a mixed state of \mathbf{k} and \mathbf{k}' as a linear combination of the two primitive Bloch states

$$\begin{aligned} \Psi_{\mathbf{k},\mathbf{k}'}(\mathbf{r}) &= a\Psi_{\mathbf{k}}(\mathbf{r}) + b\Psi_{\mathbf{k}'}(\mathbf{r}) \\ LDOS(E_0) &= |\Psi_{\mathbf{k},\mathbf{k}'}(\mathbf{r})|^2 = |a|^2 |u_{\mathbf{k}}|^2 + |b|^2 |u_{\mathbf{k}'}|^2 + \\ &+ ab^* u_{\mathbf{k}} u_{\mathbf{k}'}^* \exp(i(\mathbf{k} - \mathbf{k}') \cdot \mathbf{r}) + a^* b u_{\mathbf{k}'}^* u_{\mathbf{k}} \exp(i(\mathbf{k} - \mathbf{k}') \cdot \mathbf{r}). \end{aligned} \quad (2.14)$$

The first two terms correspond to the lattice periodic modulation of the LDOS. The last two terms are oscillating functions with wavelength $\lambda = 2\pi/(\mathbf{k}' - \mathbf{k})$ (this can be easily seen by assigning real values to a and b and the lattice periodic functions, reducing the last terms to a cosine function). A full treatment of the electron screening reveals an asymptotic behaviour of the amplitude of the oscillation for $\mathbf{r} \rightarrow \infty$ [64].

Probing the LDOS by STS it is possible to visualize the QPI standing waves around the impurities. Fig. 2.6(d) presents one example, the LDOS map for the surface of copper. Small oscillations of the density of states are found around the impurities. By Fourier transforming the spectroscopic image one obtains a map of the frequencies of the oscillations. These frequencies correspond to the magnitudes of the scattering vectors of the electron-waves. If the constant energy contour (CEC) of the material band structure is known it is

possible to relate the QPI wavelengths to the possible scattering vectors. This approach provides very local information about the static electronic structure of the surface and also the electron dynamics, identifying the possible scattering processes. Indirectly information of the spin-texture of the states can also be retrieved [65]. By varying the applied bias one can obtain the QPIs in a large range of energies to reconstruct the band dispersion. This technique is in principle very powerful and presents some advantages respect to ARPES: local informations, access to unoccupied states and scattering dynamics information. On the other hand the interpretation of the FT-STs data can be a very arduous task.

Part II

Results and Discussion

Chapter 3

Bulk band structure of Bi_2Te_3

3.1 Bismuth chalcogenides topological insulators

Bismuth chalcogenides Bi_2Se_3 and Bi_2Te_3 are without any doubt the most well known and extensively studied topological insulators [33, 66, 67]. Thanks to these materials the experimental, and theoretical, work on TIs exploded in the last five years with over 3500 articles published [68]. The success of bismuth chalcogenides is attributable to their simple topology and the ease of access to clean surfaces. Bi_2Se_3 , Bi_2Te_3 and their alloys share the same structure and topology. For this purpose we generalize referring to Bi_2X_3 to those bismuth chalcogenides $\text{Bi}_2\text{Te}_{(3-x)}\text{Se}_x$ with $0 \leq x \leq 3$ for the following discussion. Bi_2X_3 has tetradymite crystal structure, a rhombohedral lattice with space group $R\bar{3}m$ typical of metal chalcogenides [69]. Alternatively consider the hexagonal supercell whose [001] direction corresponds to the [111] direction of the primitive rhombohedral cell (we will still refer to the rhombohedral directions throughout the text). The structure possesses inversion

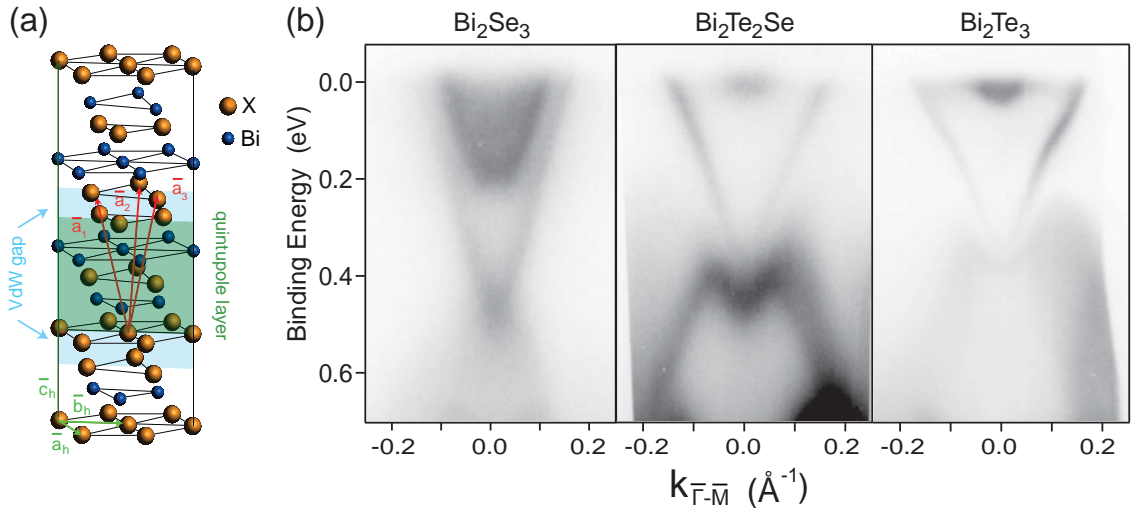


Figure 3.1: (a) Crystal structure of Bi_2X_3 : It is formed by stacking of quintuple layers separated by weak Van der Waals gaps. The vectors \mathbf{a}_1 , \mathbf{a}_2 , \mathbf{a}_3 are the lattice vectors of the primitive cell, \mathbf{a}_h , \mathbf{b}_h , \mathbf{c}_h are the lattice vectors of the hexagonal cell. (b) Low energy band structure of Bi_2Se_3 (left), $\text{Bi}_2\text{Te}_2\text{Se}$ (centre) and Bi_2Te_3 (right) from ARPES measurements.

	$a_h=b_h$ (Å)	c_h (Å)	Δ_{gap} (eV)
Bi_2Se_3	4.138	28.64	0.32
$\text{Bi}_2\text{Te}_2\text{Se}$	4.28	29.86	0.28
Bi_2Te_3	4.383	30.487	0.14

Table 3.1: Experimental lattice constants of the hexagonal supercell and band gap values for Bi_2Se_3 , $\text{Bi}_2\text{Te}_2\text{Se}$, Bi_2Te_3 . From Ref. [70].

symmetry, simplifying the topology calculations. Inspection of the modelled structure in Fig. 3.1 reveals the layered structure of the material. A sequence of quintuple layers (QL) [X-Bi-X-Bi-X] pile up along the [111] direction exposing only the chalcogenide X at the top and bottom. Stoichiometric compounds $\text{Bi}_2\text{Te}_2\text{Se}$ ($\text{Bi}_2\text{Se}_2\text{Te}$) have ordered structures where Te (Se) sits exclusively in the terminal layers while Se(Te) sits in the middle of the QL. The quintuple layers are held together by strong covalent bonding while only Van der Waals interactions act in between QLs generating a weak inter-QL bonding. For this reason the (111) is by far the most relevant surface in Bi_2X_3 TIs: the weak Van der Waals bonding makes it easy to expose a clean (111) surface with simple cleaving techniques. Structural parameters and band gap value for Bi_2Se_3 , $\text{Bi}_2\text{Te}_2\text{Se}$, Bi_2Te_3 can be found in Tab. 3.1.

The band structure topology of these materials is quite simple, and the parity eigenvalues in the bulk Brillouin zone were already shown in Fig. 1.5(a). There is a single band inversion at the bulk Γ point, leading to a non-trivial topology ($\nu = 1$). The strong spin-orbit coupling derives mostly from the bismuth atoms contribution, because of its high atomic number. Throughout the text, we will only consider the (111) surface, all the other surfaces are expected to retain the same topology but with different symmetry considerations [71]. The projected surface Brillouin zone has hexagonal shape; high symmetry points are found at the centre ($\bar{\Gamma}$), at the corners (\bar{K}) and at the mid-point of the edges (\bar{M}). A single topological state is found around $\bar{\Gamma}$ crossing the energy gap. ARPES images of the low energy band structure of Bi_2Se_3 , $\text{Bi}_2\text{Te}_2\text{Se}$, Bi_2Te_3 are shown in Fig. 3.1(b). At high binding energy the valence band has a M-like shape; the conduction band (CB) drops below the Fermi level, an intrinsic n-doping that is usually due to chalcogenide vacancies. The doping effect is particularly strong for Bi_2Se_3 while the bulk carrier concentration can be tuned to \approx zero for the two tellurides. The topological state sits in the band gap, connecting the two bulk bands. Only the upper Dirac cone is visible because the state merges in the bulk valence band (VB) just below the Dirac point (DP). It was revealed that the VB maximum for Bi_2Se_3 is found at $\bar{\Gamma}$, creating a direct gap, and has hole-like character [72]. The Dirac point sits just above the valence band maximum (VBM). Contrarily the TS in $\text{Bi}_2\text{Te}_2\text{Se}$ and Bi_2Te_3 sinks in the bulk VB making the Dirac point inaccessible to transport. The dispersion of the topological state can always be approximated to a line close to the Dirac point. Further away from $\bar{\Gamma}$ the bands deviate from linearity because of a combination of spin-orbit interaction and crystal symmetry. This result in a characteristic trigonal warping of the topological state constant energy contours [73, 74]. The warping effect is small for Bi_2Se_3 and it becomes stronger along the series towards Bi_2Te_3 .

3.2 A study of the Bi_2Te_3 bulk band structure

Bi_2Se_3 and Bi_2Te_3 are considered prototypical TIs. Despite the many similarities there are also several significant differences when looking at the band structure. It has been shown and explained how the Bi_2Te_3 exhibits a strong hexagonal warping effect on the TS [73]. This effect, even if present, is much weaker for Bi_2Se_3 . On a second look, the bulk band structure of these materials can be quite different as well. Of particular interest are the bands closest to the Fermi level. The nature of the gap for Bi_2Te_3 is still subject of debate with controversial results both in theory and experiments [75–77]. To resolve this a good match between theory and experiments is strongly desirable. *Ab initio* calculations of topological insulators have mainly been performed using local density (LDA) or generalized gradient (GGA) approximations of density functional theory (DFT). These approach allows the study of bulk band structure as well as the surface band structure, which attracted the most interest in these materials. While these approaches, with the necessary inclusion of spin-orbit coupling, gave good agreement with the experimental results for the topological surface state [66, 78], they seem to fail in reproducing correctly the low energy bulk states. In particular the concave shape of the top valence band and bottom conduction band, classic feature of the SOC induced band gap, seem to be exaggerated. The band gap size is underestimated by LDA instead.

To address this issues we combine a thorough ARPES study of the bulk band structure of Bi_2Te_3 with DFT calculations performed in the LDA approximation with inclusion of the *GW* correction [79, 80]. The *GW* correction takes care of the quasi-particle corrections to the energy spectrum and it has been shown how this compares better to photoemission experiments [75, 81], and in particular it seem to better describe shape and size of the band gaps in TIs [72, 75, 77, 81–86]. The description of the bulk band dispersion through ARPES requires to acquire photoemission spectra using different photon energies. The photon energy can be transformed, using some assumptions, into \mathbf{k}_\perp coordinates [87] as described in chapter 2.

ARPES spectra have been acquired at the SGM3 beamline at ASTRID. The Bi_2Te_3 sample was cleaved in vacuum ($\sim 10^{-8}$ mbar) with the scotch tape technique. The sample was rotated such that the data are acquired with the two high symmetry directions $\bar{\Gamma}\bar{M}$ and $\bar{\Gamma}\bar{K}$ along the non dispersive plane of the analyser. The photon energy used spans from 14 eV to 32 eV. In this low-mid energy range the mean free path of the electrons is in the order of 5-15 Å. While this is indeed a surface sensitive technique the tail of the bulk wave function extends well onto the surface making it accessible to direct investigation.

The conversion from photon energy to \mathbf{k}_\perp has been done with the assumption of a free electron final state. This assumption might as well be not accurate but a wrong final state will only stretch the \mathbf{k}_\perp scale, but it will not influence the conclusions we draw. In particular bandwidths and the binding energy of critical points, used for the calibration of V_0 , are not affected. The inner potential V_0 has been chosen as a fitting parameter: we identified the Γ and Z points in the photon energy scans thanks to strong \mathbf{k}_\perp dispersion of the low energy states; V_0 was chosen such that the Γ point is at \mathbf{k}_\perp value multiple of the Brillouin zone extent in the perpendicular direction and such that the Γ - Z distance corresponds to the actual value. V_0 is unequivocally determined to the value of 1 eV.

The LDA and *GW* calculations were performed within the all-electron full-potential linearised augmented-plane-wave (FLAPW) formalism using the codes Fleur [88] and spex, [89] respectively. The SOC was incorporated self-consistently employing the second vari-

ation technique [90]. The SOC effects are not applied as *a posteriori* correction but it is rather taken into account in the reference system allowing for the self energy to renormalise the SOC itself [83]. The quasi particle equation in the basis of the LDA single-particle states is here solved explicitly, taking into account the off-diagonal elements of the self-energy. This already proved to describe more correctly the top valence band of Bi_2Te_3 in Ref. [86]. The complete description of the calculation methods used for the following work can be found in Ref. [4]

The Bi_2Te_3 samples were grown in Soares group at Universidade Federal de Minas Gerais, ARPES experiments and analysis were made by the author, DFT calculations were carried out by Irene Aguilera in Blügel group at Forschungszentrum Jülich.

3.2.1 The calculated band structure: LDA vs GW

In Fig. 3.2(a) the bulk band dispersion of Bi_2Te_3 , calculated by LDA with and without GW correction is shown along the the Γ -Z-F- Γ -L line. The Figs. 3.2(b) and (c) show the band structure projected on the (111) surface. The energy scale of all the calculations has been rigidly shifted downward of 0.13 eV to fit with the experimental data. Since this is a bulk band structure calculation the surface states are here not present. In the Fig. 3.2 green circles, called A, B, C, emphasize the three main differences between LDA and GW : A denotes the differences in dispersion and binding energy at Γ and Z for the upper valence band (VB1) and the lowest conduction band (CB1). B remarks the difference in the size of the projected band gap below the VB1, the size of which is much higher in GW . C addresses the nature and size of the energy band gap. While LDA shows an almost-direct band gap along the Z-F line, GW reallocates the CBM along the Γ -Z line and generates a larger band gap. It should be noted that our calculated band structure differs from what was seen by other studies [81], especially in the shape of the VB1 where GW does not pertain the M-shape. This difference is due to the *a posteriori* inclusion of the SOC in Ref. [81].

3.2.2 ARPES vs DFT

Fig. 3.3 shows the ARPES spectra acquired around $\bar{\Gamma}$ along the two high symmetry directions $\bar{\Gamma}\bar{M}$ and $\bar{\Gamma}\bar{K}$ for the freshly cleaved Bi_2Te_3 at three different photon energies. In the three panels the band structure of the seventh Brillouin zone at Γ (a), Z (c) and a point in between (b) are shown. The different photoemission intensities along the two directions is due to matrix elements effects connected to the spin-orbital character of the states. The topological state is visible in the gap assuming the usual Dirac-cone shape, this assesses the quality of the sample and of the cleave. Below the Dirac cone there is the M-shaped upper valence band (VB1). At the bottom there is a very intense V-shaped state that here we argue is a surface state of Bi_2Te_3 . Finally at the Fermi level some spectral intensity reveals the presence of the lower conduction band (CB1) between the TS branches. The presence of the CB below the Fermi level is symptomatic of the n-doping of the bulk Bi_2Te_3 , possibly due to tellurium vacancies in the crystal [91]. While the VB1 and the CB1 show dispersion in \mathbf{k}_\perp , the topological state and the surface state do not show dispersion, as expected. The VB1 at Γ (Fig. 3.3(a)) is significantly lower respect to Z (Fig. 3.3(c)). This is better visible when looking at the \mathbf{k}_\perp dispersion at $\bar{\Gamma}\bar{M}$ as shown in Fig. 3.4

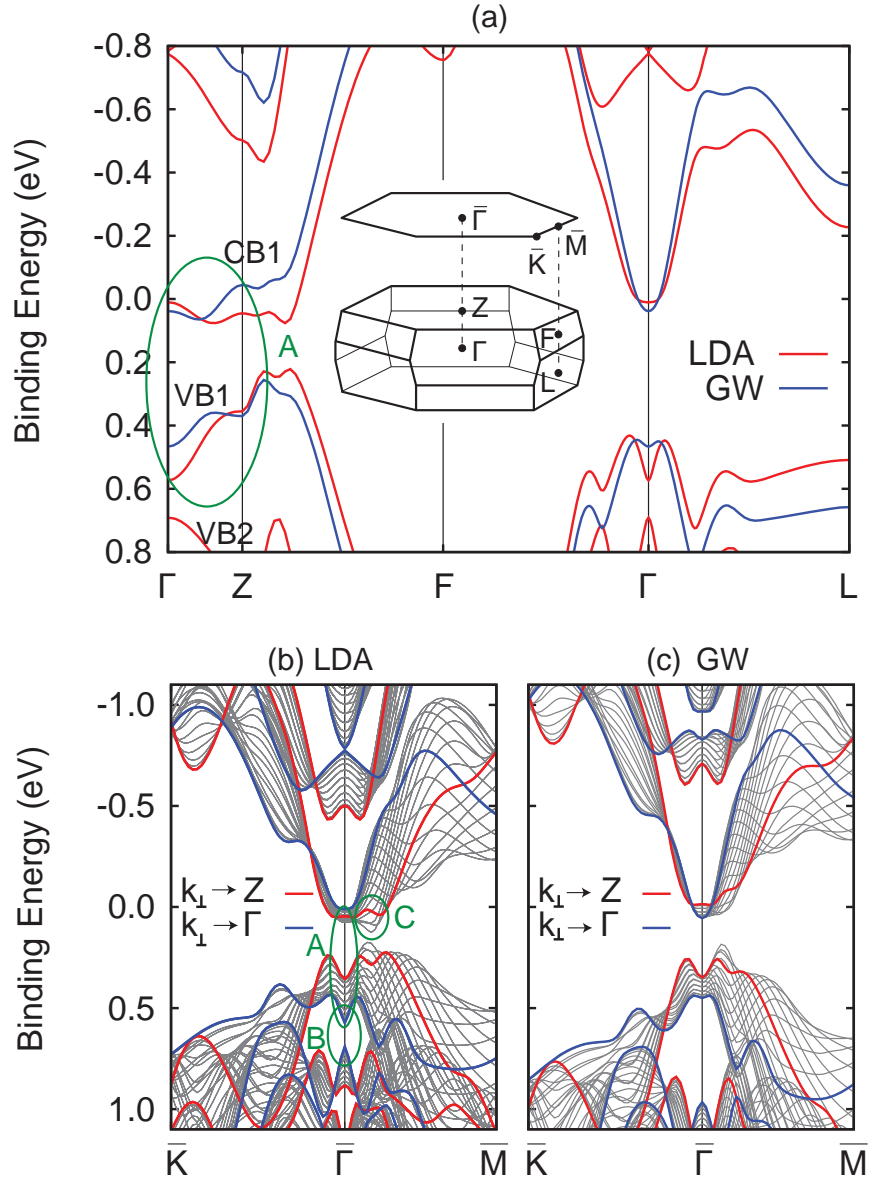


Figure 3.2: (a) Bulk band dispersion of Bi_2Te_3 calculated by LDA (red) and GW (blue). VB1, VB2 and CB1 denote the bands for which the dispersion is compared to the experimental data. The inset shows the bulk Brillouin zone and its projection onto the (111) surface. (b) and (c) display the projected bulk bands of Bi_2Te_3 onto the (111) surface along the $\bar{\Gamma}$ - \bar{K} and $\bar{\Gamma}$ - \bar{M} directions, calculated with LDA and GW , respectively. The green circles denote the regions **A**-**C** that were chosen for a comparison to the experimental data because the differences between LDA and GW are maximal.

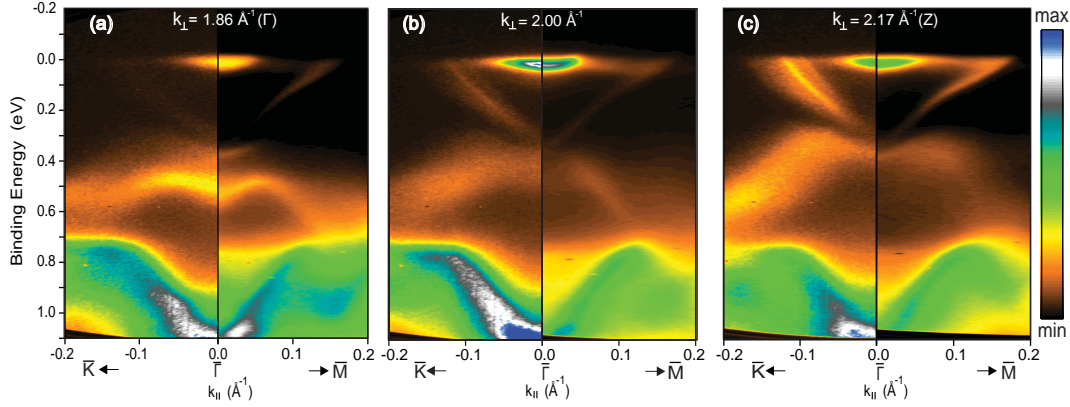


Figure 3.3: (a-c) Photoemission intensity from $\text{Bi}_2\text{Te}_3(111)$ along the $\bar{K}-\bar{\Gamma}$ and $\bar{\Gamma}-\bar{M}$ directions, for different values of the crystal momentum perpendicular to the surface \mathbf{k}_\perp .

Here we identify the Γ and the Z points by looking at the dispersion of VB1 and through a comparison with the calculated bands. At the Γ point the VB1 reaches a minimum. At the Z point LDA predicts an energy maximum. On the other hand, the GW correction smooths down the maximum point resulting in a dip in the \mathbf{k}_\perp dispersion at Z. In the ARPES data the Z point is first identified by carefully fitting both VB1 and CB1 from 2.05 \AA^{-1} to 2.25 \AA^{-1} and locating the symmetrical point.

We look into the three spectral regions A-C where the differences between LDA and GW are more relevant. A: After a first inspection of Fig. 3.4, looking at the direct comparison between ARPES data and calculations, it appears that the actual result lies somewhere in between the two: LDA predicts a larger bandwidth for VB1 and a monotonic increase in energy. GW on the other hand, narrows the bandwidth and produces the dip at the Z point. ARPES shows a smaller bandwidth respect to LDA; GW corrects the dispersion in the right direction but seems to overestimate the renormalisation. The dip in binding energy at Z is also found in the experimental data. The \mathbf{k}_\perp dispersion at $\bar{\Gamma}$ of the CB1 shows also strong differences between the two theoretical approaches: both LDA and GW find a conduction band minimum between Γ and Z (at $\mathbf{k}_\perp = 2.06 \text{ \AA}^{-1}$ and 1.99 \AA^{-1} , respectively). The main difference is at the high symmetry points where the GW predicts a higher binding energy at Γ with respect to LDA, but it is much lower at the Z point, resulting in a larger bandwidth. Conveniently we can see part of the conduction band in the photoemission experiment because of the n-doping. Indeed the experiment seems to reproduce the presence of a minimum between the two high symmetry points at $\mathbf{k}_\perp = 2.035 \text{ \AA}^{-1}$, and this seems to be replicated in the next Brillouin zone. Nevertheless the CB1 is dispersing above the Fermi level and we only see the tail of the CB spectral function. The dispersion in the unoccupied states and the strong matrix elements effects on the photoemission intensity at different photon energies (and therefore at different \mathbf{k}_\perp) make it impossible to precisely reconstruct the energy dispersion at the Brillouin zone edge.

B: The region around $\bar{\Gamma}$ between the first and the second valence band (VB2) is distinctly different in LDA and GW , where the projected gap between the two valence bands is much larger in the GW case. This is ascribed to the much smaller gap between VB1 and VB2 at

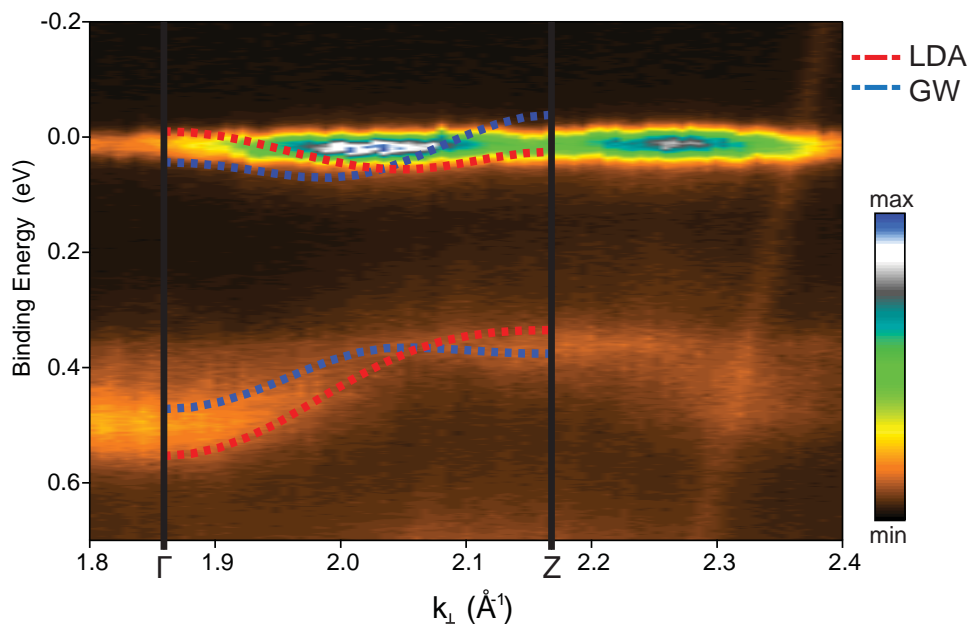


Figure 3.4: Photoemission intensity in normal emission as a function of \mathbf{k}_\perp , i.e., the dispersion along the Γ -Z direction with over-imposed band structure calculations along Γ -Z using the LDA (red dashed line) and GW (blue dashed line) approximations. The position of the bulk Γ and Z points is marked. The Fermi level of theoretical data is shifted by +0.13 eV with respect to midgap. The labels VB1 and VB2 refer to the calculations.

the bulk Γ point for LDA. Further towards \bar{K} and \bar{M} the gap is dictated by the dispersion of the VB2 at the Z bulk point. We compare the two scenarios with the experiments by plotting the experimental and theoretical dispersion at the Γ bulk point in Fig. 3.5. The VB1 is well visible in the ARPES data. The energy of VB1 close to normal emission seems again to stand between LDA and GW. The VB2 is not clearly visible and it appears to be dispersing at higher binding energies. Instead a very intense V-shaped state is visible in that spectral region. This is not to be confused with the VB2. As it can be seen in Fig. 3.3 the V-state does not show any dispersion in \mathbf{k}_\perp but merely different intensity, as confirmed by fitting the dispersion at different photon energies. The reason why this band is not predicted by the calculation is because of its surface nature. A similar state has been found in Bi_2Se_3 and Sb_2Te_3 thanks to surface calculation within LDA [92–94]. In the case of Bi_2Te_3 previous surface LDA studies show a wrong W-shaped state at the surface [78, 92]. The distortion of this state is symptomatic of the wrong bulk gap in LDA between VB1 and VB2. The absence of VB2 features in the energy range investigated proves that the gap is much larger than predicted by LDA, in better agreement with GW. However the gap is likely to be even larger than predicted by GW. VB2 can be actually seen at the bulk Z point in Fig. 3.3 at $\mathbf{k}_\parallel \approx 0.17 \text{ \AA}^{-1}$ off normal emission and approximately 0.9 eV of binding energy.

C: We now address the nature of the band gap in Bi_2Te_3 . The main difference between LDA and GW is in the position of the conduction band minimum. Fig. 3.2(b) shows a CBM out of normal emission, specifically CB1 drops below the value at $\bar{\Gamma}$ for $\mathbf{k}_\parallel = 0.145 \text{ \AA}^{-1}$ along the $\bar{\Gamma}\bar{M}$ direction with the highest binding energy reached at $\mathbf{k}_\perp = 2.108 \text{ \AA}^{-1}$. This

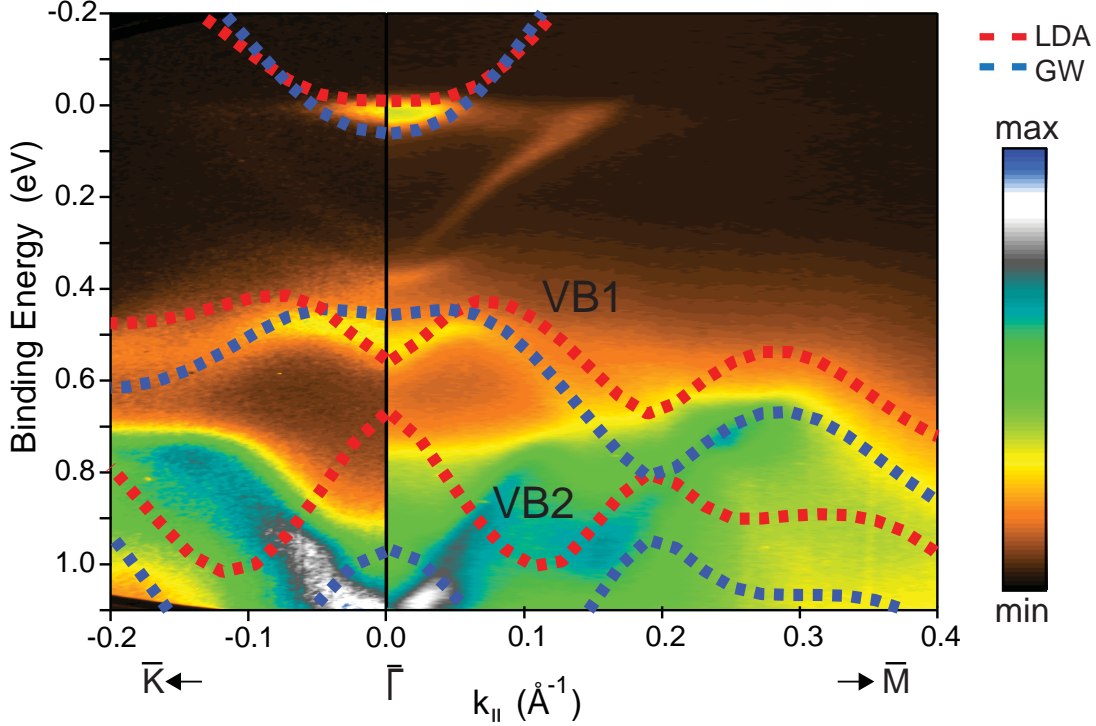


Figure 3.5: (a) Photoemission intensity for \mathbf{k}_\perp near the bulk Γ point along $\bar{K}-\bar{\Gamma}-\bar{M}$ direction with the calculated band dispersion in the LDA (red dashed line) and GW (blue dashed line) approximations superimposed. Fermi level of theoretical data is shifted by $+0.13$ eV respect to midgap.

generates a quasi direct gap with the VB1, as plotted in Fig. 3.6(a). The ARPES do not show any sign of this drop of the CB1. This can be seen by looking of Fig. 3.6(b). Here the \mathbf{k}_\perp dispersion of the CB1 at $\mathbf{k}_\parallel = 0.145 \text{ \AA}^{-1}$ is plotted. The N and O points in the Brillouin zone are defined as the projections of Γ and Z on the $\mathbf{k}_\parallel = 0.145 \text{ \AA}^{-1}$ line. The single intensity streak is non-dispersing and can be assigned to the topological state, while the CB1 drop is not detected. From the ARPES it is evident that the CBM is found at $\bar{\Gamma}$. This is the same conclusion the GW calculation draws. The VBM is predicted for both LDA and GW to be out of normal emission at the \mathbf{k}_\perp shown in Fig. 3.6. In both cases the VBM is predicted to be along the $\bar{\Gamma}\bar{M}$ direction rather than the $\bar{\Gamma}\bar{K}$. This does not find proof in the experimental results where the energy of the VBM along the two directions is found to be very similar. In better agreement with the experiment, GW opens the gap wider by pushing the VBM to higher binding energy. The CB is also smoothed by the quasi-particle effects but not enough to appropriately describe the single-minimum shape of the CB from ARPES in Fig. 3.6(a). The nature of the gap is a clear evidence of the efficiency of the GW approach. This in fact places the CBM at $\bar{\Gamma}$ creating a clear indirect band gap as observed in the experimental results as well. The size of the gap is 120 meV, in better agreement with experimental data of 130-170 eV [95–98]. LDA instead predicts an almost direct band gap of 50 meV out of normal emission as discussed. We point out that the perturbative one-shot GW approach, that calculates only the diagonal elements of the self energy, has been shown to give wrong predictions [72], because of the neglect

of hybridization effects from the off-diagonal part of the self energy.

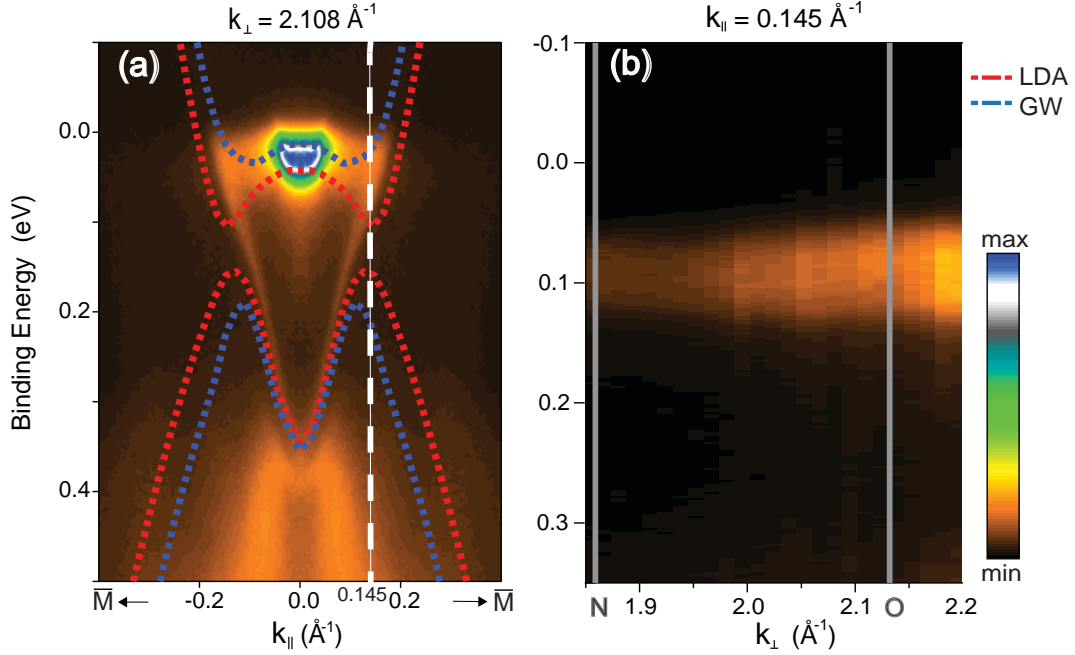


Figure 3.6: (a) Photoemission intensity along the $\bar{M}-\bar{\Gamma}-\bar{M}$ direction for the k_{\perp} value where LDA predicts the minimum of the conduction band with the calculated band dispersion in the LDA (red dashed line) and GW (blue dashed line) approximations superimposed. (b) Photoemission intensity for the k_{\parallel} value of the conduction band minimum as predicted by LDA as a function of binding energy and k_{\perp} . The corresponding k_{\parallel} value is marked in (a) by a vertical dashed line. We define here points N and O as the projections of Γ and Z on the $k_{\parallel}=0.145 \text{ \AA}^{-1}$ line. The only discernible feature is caused by the topological surface state. Fermi level of theoretical data is shifted by $+0.13 \text{ eV}$ respect to midgap.

3.3 Summary

We investigated the bulk electronic structure close to the Fermi level of Bi_2Te_3 . We acquired ARPES using different photon energies to probe the 3-dimensional band dispersion. We compare the bulk band structure obtained by ARPES with the calculated one using both LDA and GW approach. The GW demonstrate an overall better agreement with the experimental results even if still lacking the perfect description. In particular, the quasi particle effects, incorporated in GW , produce three main effects: increasing the size of the SOC band gap, smoothing the CB and VB dispersion around $\bar{\Gamma}$ conferring a more convex shape and relocating, as a consequence, the CBM into $\bar{\Gamma}$, increasing the size of the projected band gap below VB1. The comparison with the experimental data demonstrate that these effects all work in the correct direction (increasing the gap and relocating the band extrema) even if the magnitude of the correction is not perfect. The better agreement of ARPES with GW strongly points towards strong many-body effect that renormalise the low energy band structure in Bi_2Te_3 as in other topological insulators [75, 81].

Chapter 4

Surface modifications and new electron states in bismuth tellurides

In Chapter 1 it was seen how in-gap states can exist at the surface (interface) of a semiconductor because of the breaking of the translational symmetry. Interestingly, the same broken symmetry is required for the Rashba effect to appear, making the creation of Rashba split states a feasible option. Tailoring the properties of the surface of semiconductors can pave the way to new electronic physical properties. One way to achieve this is through surface modification.

4.1 Two dimensional electron gasses at surfaces

The surface is particularly sensitive to the change in the local electric potential. It is well known that a change in the potential at a surface (interface) induces the so-called band bending. The first time the band bending was modelled for the case of the interface between a metal and a semiconductor [99, 100] where, because of the difference in the work function, there is an electron exchange in the contact region. In equilibrium condition the chemical potential is constant through the interface. This electron exchange provokes the “bending” of the semiconductor bands [101] (Fig. 4.1(a)). The band bending model applies every time a charge transfer occurs at the interfaces (surfaces are an interface with vacuum). The charged interface induces an electric field that provokes the rearrangement of the carriers over a length on the order of the Thomas-Fermi screening length. When a downward band bending occurs, a surface accumulation of electrons in the depletion layer can be created, populating metallic states called two dimensional electron gas (2DEG). This can be achieved by directly applying a gating bias, such as in metal-oxide-semiconductor interfaces.

A 2DEG derives from the confinement of the conduction band of the semiconductor in two dimensions by the interface potential and behaves as a free electron state confined in a plane. The 2DEG becomes quantized in discrete levels because of the small confinement region. The situation is represented in Fig. 4.1(b) where the confinement creates well defined quantum well states on a surface. The shape of the surface potential V is related to the charged density (ρ) through the Poisson equation $d^2V(x)/dz^2 = -\rho/\epsilon_0\epsilon_r$ where ϵ_0 and ϵ_r are the vacuum and the relative dielectric constants. Each of these confined states

is quasi two dimensional and disperses at a different energy, with the state found at highest binding energy being in the steepest part of the potential and most localized on the surface (interface).

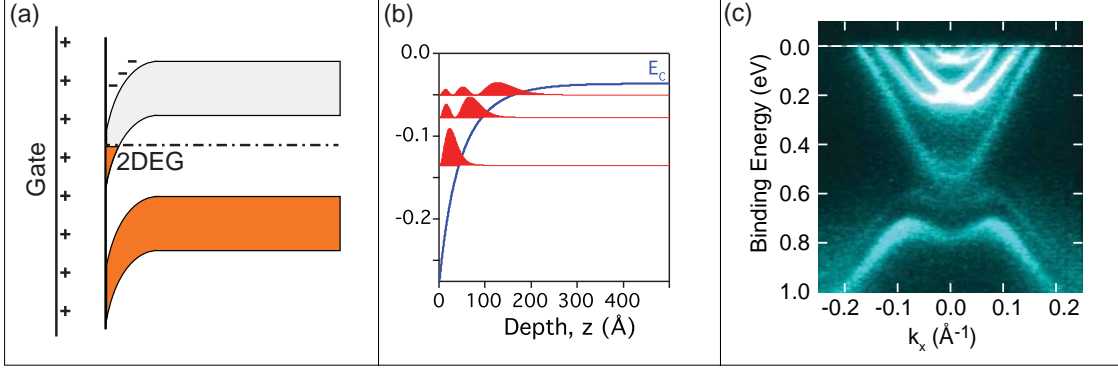


Figure 4.1: (a) Sketch of downward band bending, a gate is applied on the material surface creating a band bending, when the conduction band drops below the Fermi level quantized 2DEGs are populated. (b) Example of near-surface band bending (blue) with the calculated energy levels and modulus-squared envelope wave functions of the quantum-confined states (red). After Ref. [102]. (c) ARPES on Bi_2Se_3 with Rb surface doping. Two 2DEGs with strong Rashba splitting are induced on the surface. After Ref. [103].

2DEGs are normally found in semiconductor heterojunctions [104] and are nowadays one of the fundamental phenomena in semiconductor electronics. 2DEGs are vastly exploited in transistor components [105] and can display a great amount of exotic properties, such as superconductivity [106], fractional quantum Hall effect [107] and spin-degeneracy lifting [102]. While the 2DEG have been well known in semiconductor hetero-structures for long time, only recently it has been possible to directly resolve the electronic dispersion of 2DEG states. This can be achieved with the use of ARPES combined with the observation of 2DEGs in very shallow layers of the material [108] or directly on the material's surface. Intrinsic 2DEGs on surfaces have been resolved by ARPES in InAs [109] and InN [110] and CdO [111]. In alternative a 2DEG can be induced by chemical gating, dosing electron donor atoms on the surface of the semiconductor in order to induce a local charge transfer and populate the 2DEG.

This approach was used in previous works on the topological insulator Bi_2Se_3 [103]. Interestingly, Bi_2Se_3 develops a 2DEG with lifted spin degeneracy because of the Rashba effect [102, 112], as shown in Fig. 4.1(c). The strong spin-orbit coupling, key ingredient of topological insulators, pushes the two sub-bands far apart reaching a momentum splitting of 0.08Å^{-1} . The value of spin splitting is 4-5 times higher than in the surface state of gold, placing Bi_2Se_3 as optimal candidate for spintronic applications. The 2DEG on Bi_2Se_3 is appropriately described by a simple first-order Rashba model for a free electron state.

In this work we investigate the 2DEG on topological insulators $\text{Bi}_2\text{Te}_2\text{Se}$ and Bi_2Te_3 by chemical gating using Rb atoms. We find that the induced 2DEG is strongly spin split and the combination of crystal symmetry and Rashba coupling generates an exotic 2DEG with anisotropic spin-splitting of the bands.

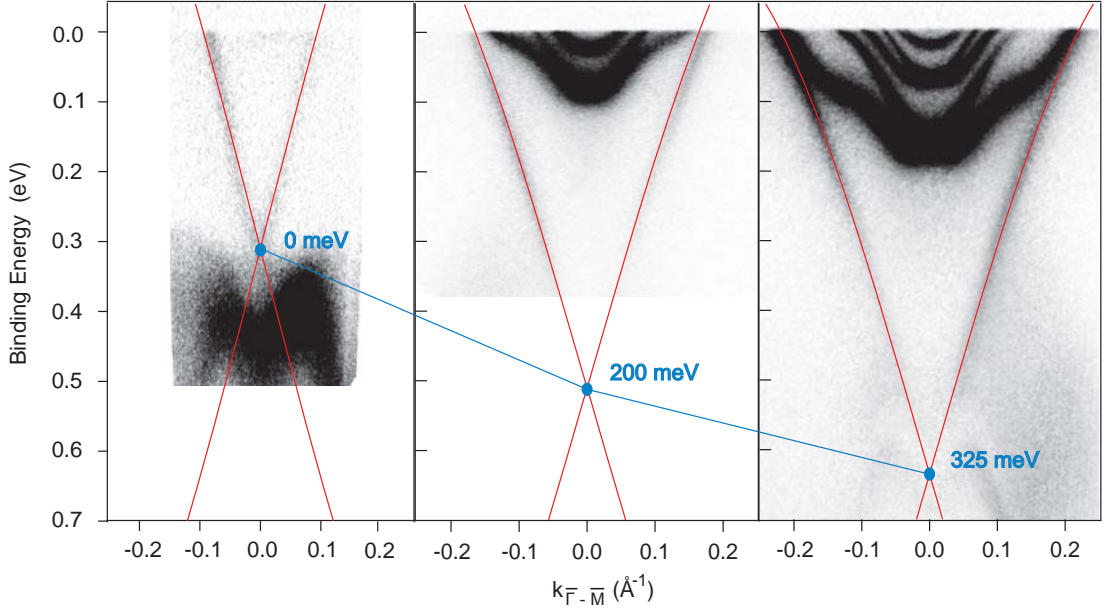


Figure 4.2: Evolution of the Dirac point of $\text{Bi}_2\text{Te}_2\text{Se}$ with Rb doping. ARPES spectra of the in-gap region at different doping levels are shown. The red lines show the fit of the Dirac cones. On the left: Sample after cleave. In the middle: Low doping case, the Dirac point is shifted to higher binding energy by 200 meV. On the right: High doping case, the Dirac point is shifted to higher binding energy by 325 meV with respect to the freshly cleaved sample.

4.2 Anisotropic 2DEGs on topological insulators

4.2.1 Rb-surface doping of $\text{Bi}_2\text{Te}_2\text{Se}$

$\text{Bi}_2\text{Te}_2\text{Se}$ samples have been cleaved in UHV conditions at low temperature using top-post technique. The cleaving plane is the (111). Experiments were performed at the I05 beamline at the Diamond light source. The samples were placed in the measurement manipulator, cleaved and Rb was dosed on the surface at around 10 K. Depending on the time of Rb deposition, we could achieve a lower or higher doping level of the surface. Thanks to its low ionization energy rubidium is a good in-situ n-dopant for the surface, moreover rubidium was already used in past works on Bi_2Se_3 [102, 103] so our choice allows for a better comparison between the two systems. $\text{Bi}_2\text{Te}_2\text{Se}$ is an optimal TI candidate for transport measurements and devices; this is due to the low bulk carrier density at the Fermi level. Differently from the homologous Bi_2Se_3 , $\text{Bi}_2\text{Te}_2\text{Se}$ is less intrinsically n-doped and the conduction at low temperature can be considered 2-dimensional and passing through the topological state [113]. Data from two different amount of Rb doping are measured. The photon energy used is $h\nu=21$ eV, energy and angular resolution are better than 10 meV and 0.2° , respectively. The photon energy has been chosen to minimize matrix element effects in the spectral intensity in different directions due to the orbital character of the topological state and the 2DEG. Spectra for the doped cases are acquired with both circular right and circular left polarized light and the two spectra are summed together simulating a non-polarized light probe.

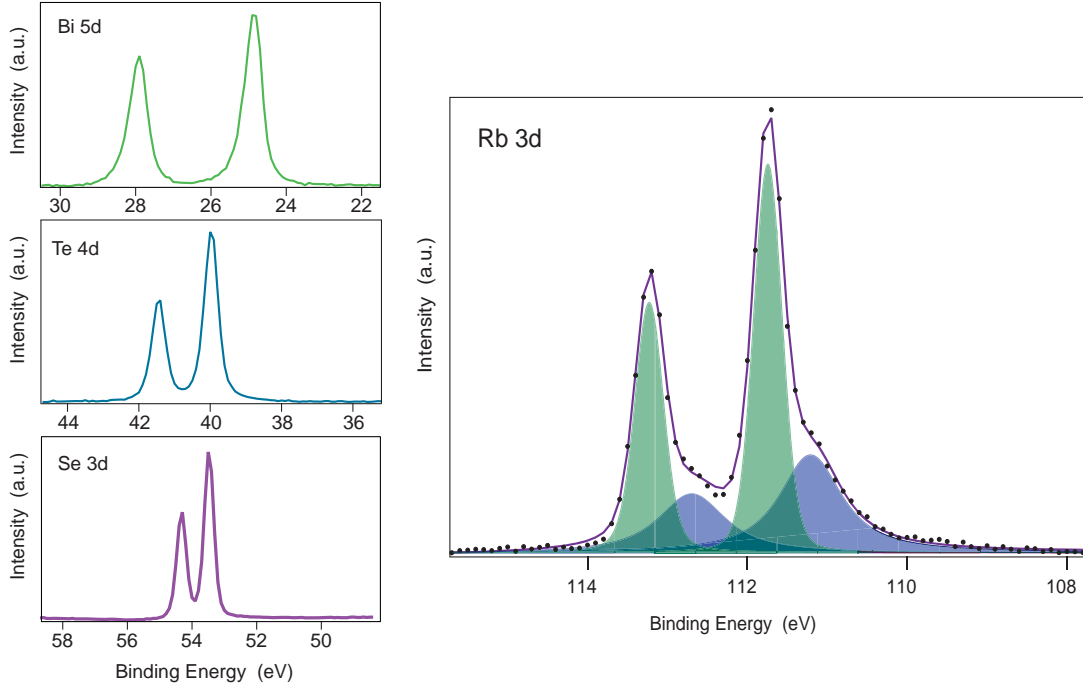


Figure 4.3: Core levels spectra for Rb-doped $\text{Bi}_2\text{Te}_2\text{Se}$ after Shirley background subtraction. On the left: spectra of single components Bi 5d, Te 4d and Se 3d levels. The doublet is due to spin-orbit splitting into $d\ 3/2$ and $d\ 5/2$. On the right: Core level spectrum of Rb 3d core level. Black dots represent the data points, the purple line is the fitted peaks profile. In green and blue the four components used for the fitting are highlighted. Green components are attributed to on-surface Rb while the blue are attributed to intercalated Rb.

The evolution of the low energy spectrum upon Rb adsorption is shown in Fig. 4.2. The intensity scale has been saturated to better visualize the topological state. In the left panel the spectrum of freshly cleaved $\text{Bi}_2\text{Te}_2\text{Se}$ around $\bar{\Gamma}$ is shown. Above 0.3 eV of binding energy the valence band assumes the characteristic M-shape. The in-gap state is the topological state, no sign of conduction band is detected at the Fermi level, confirming the good insulating behaviour of this material. From first inspection, a strong downward shift of the spectrum upon Rb adsorption is evident. The position of the Dirac point has been found by fitting the topological state with the $\mathbf{k} \cdot \mathbf{p}$ model described in Ref. [73] including anisotropic and isotropic third order terms to take into account of the non-linearity of the TS far from the DP. The red line shows the shape of the Dirac cone model after fitting. The $\mathbf{k} \cdot \mathbf{p}$ parameters are kept for the three cases with no relevant loss of accuracy in the fitting, showing that the doping acts merely shifting rigidly the state. The rubidium on the surface acts as a front gate on the sample because of its electron donor quality. In the low doping case the surface localized topological state is shifted by 200 meV. New spectral features at the Fermi level are ascribed to the population of conduction band-like states at the surface, creating a 2DEG. By further doping, the high doping case is achieved. The DP undergoes a total shift of 325 meV.

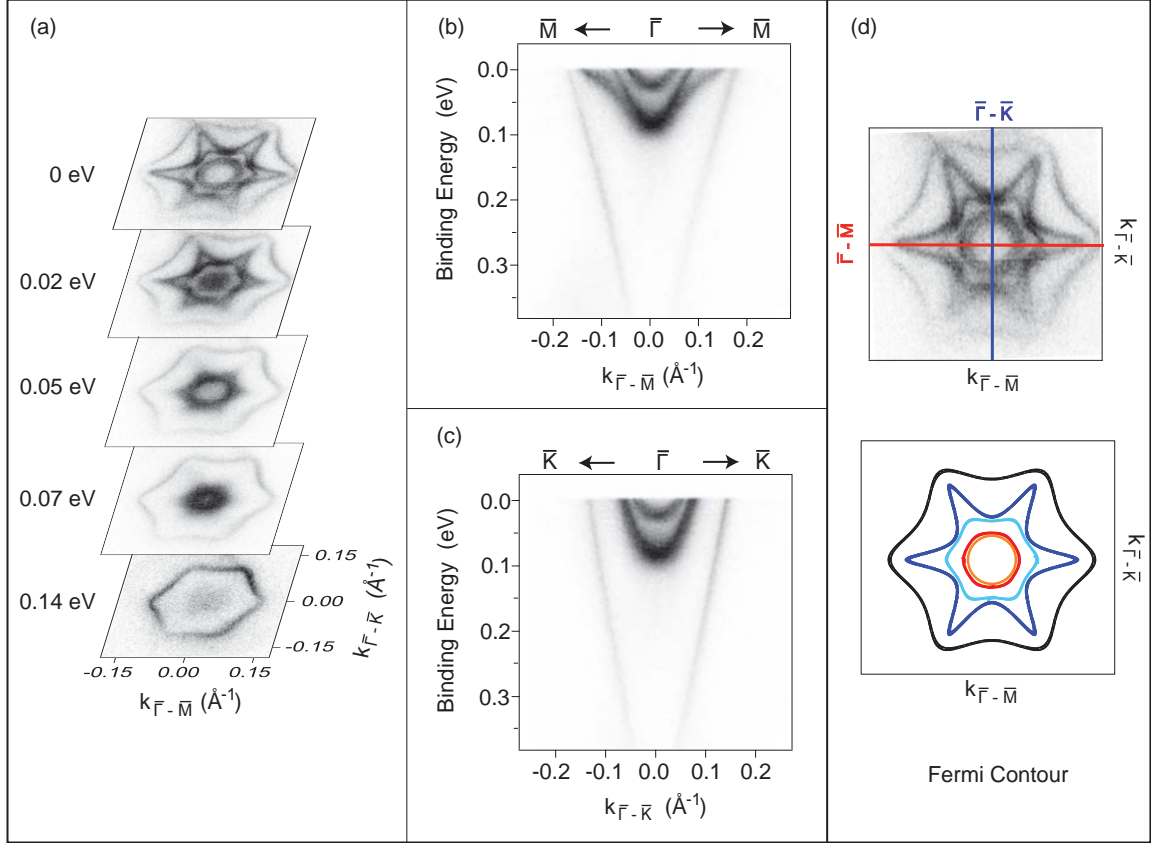


Figure 4.4: Electronic structure of electron doped $\text{Bi}_2\text{Te}_2\text{Se}$ for the low doping case as obtained by ARPES. (a) Constant energy surfaces at different binding energies. (b) and (c) Dispersion along the $\bar{\Gamma}\bar{M}$ and $\bar{\Gamma}\bar{K}$ directions, respectively. (d) On the top: Fermi contour of electron doped $\text{Bi}_2\text{Te}_2\text{Se}$. On the bottom: schematic representation of the Fermi contours. In black the topological state, in blue(light blue) the first 2DEG, in red(orange) the second 2DEG.

The acquisition of the Rb 3d core level spectrum, displayed in Fig. 4.3, confirms the presence of the dopant on the surface. The spin-orbit splitting of 1.5 eV is as expected [114]. Two doublets, green and blue in Fig. 4.3, are attributed to the different chemical environment the Rb atoms are sitting in. The green peaks are attributed to the atoms adsorbed on the surface, while the blue components possibly result from the intercalation of the Rb below the surface, likely in the Van der Waals gap of $\text{Bi}_2\text{Te}_2\text{Se}$. This effect was measured and more extensively studied in the case of Rb doping of Bi_2Se_3 in Ref. [103], where it was shown that subsequent annealing would lead to the Rb intercalation and to the intensity enhancement of the lower binding energy doublet. We obtain a very rough estimation of the adsorbed Rb amount from the comparison of Rb and Te core level intensities for the high doping case. This is around 10% of a monolayer.

4.2.2 An exotic 2DEG

The overview of the band structure obtained by ARPES is shown in Fig. 4.4 for the low doping and in Fig. 4.5 for high doping level. In both cases 2DEGs are induced at the

surface; a strong spin-orbit splitting clearly splits the 2DEG in two branches. In the low doping case two 2DEGs are induced. For convenience we enumerate these quantum well states according to their energy minimum, "first 2DEG" being the one that disperses at the highest binding energy, and so on. Panel (a) shows the evolution of the constant energy contours at different binding energies for the low doping case. It can be observed that the first 2DEG evolves in complex contours inside the hexagon of the topological state. At the Fermi level this assumes the shape of an hexagon inside a star. Remarkably these contours arise from the two branches of the same 2DEG. A better insight on the bizarre shape of the contour can be found by looking at the energy dispersion of the states, shown in panels (b) and (c) along the two high symmetry directions $\bar{\Gamma}\bar{M}$ and $\bar{\Gamma}\bar{K}$. Along $\bar{\Gamma}\bar{K}$ both 2DEGs have a fairly parabolic shape, like a free electron state. Along the $\bar{\Gamma}\bar{M}$ direction, on the other hand, the first 2DEG strongly diverges from the parabolic shape with the lower branch assuming a negative curvature and giving rise to the "tips" of the star-contour. Even more interestingly, the spin splitting in the $\bar{\Gamma}\bar{K}$ direction is so small to be barely detectable in our experiment, while the momentum splitting along $\bar{\Gamma}\bar{M}$ is strongly enhanced, as shown in the schematics of the Fermi surface in Fig. 4.4(d).

The high doping case (Fig. 4.5) is achieved by stronger Rb-doping: here the higher electron density populates a third 2DEG. The splitting is even bigger than in the low doping case because of the increased slope of the electric potential at the surface [102]. The basic shape of the constant energy contours remains the same, both branches of the first 2DEG are strongly hexagonally warped with the outer branch almost touching the TS. The second 2DEG now shows an anisotropic splitting too. The $\bar{\Gamma}\bar{K}$ dispersion, depicted in Fig. 4.5(c), presents in this case a relevant splitting while still remaining parabolic in shape. The $\bar{\Gamma}\bar{M}$ dispersion reveal now a even more complex shape: around 0.1 eV of binding energy the dispersion diverges outward, similarly to the low doping case, reaching a singularity point, a minimum in the slope. The curvature of the branch becomes again positive closer to the Fermi level. The situation here depicted is the one of a strongly anisotropic two dimensional electron gas where the anisotropy influences not only the shape of the bands but also the actual spin-splitting between the two branches. It is clear that a quasi-free-electron description for these 2DEGs will be inadequate.

4.2.3 The "warped" effective Rashba Hamiltonian

We attempt to describe the dispersion and the splitting of the 2DEGs on Bi₂Te₂Se by employing a $\mathbf{k}\cdot\mathbf{p}$ phenomenological approach. We start from the most simple model, vastly utilized to describe spin-orbit splitting in surface states and 2DEGs.

$$E(\mathbf{k}) = E_0 + \frac{\hbar^2 k^2}{2m^*} \pm \alpha k, \quad (4.1)$$

for a state of effective mass m^* , where α is the so called Rashba term. The energy splitting $\Delta E = 2\alpha k$ is linear in \mathbf{k} and the k -splitting $\Delta k = 2\alpha m^*/\hbar^2$ is constant. An anisotropic splitting of the bands is predicted when higher order Rashba terms are included in the effective Hamiltonian. These terms are dependent on the point group symmetry of the system. The Hamiltonian was developed up to the third order for the topological state in Ref. [73]. This proved that the topological state can also be described by the Rashba Hamiltonian for a linear dispersion. This approach successfully described the hexagonal warping found in Bi₂Te₃ TS. In order to have a more complete and extensive picture we

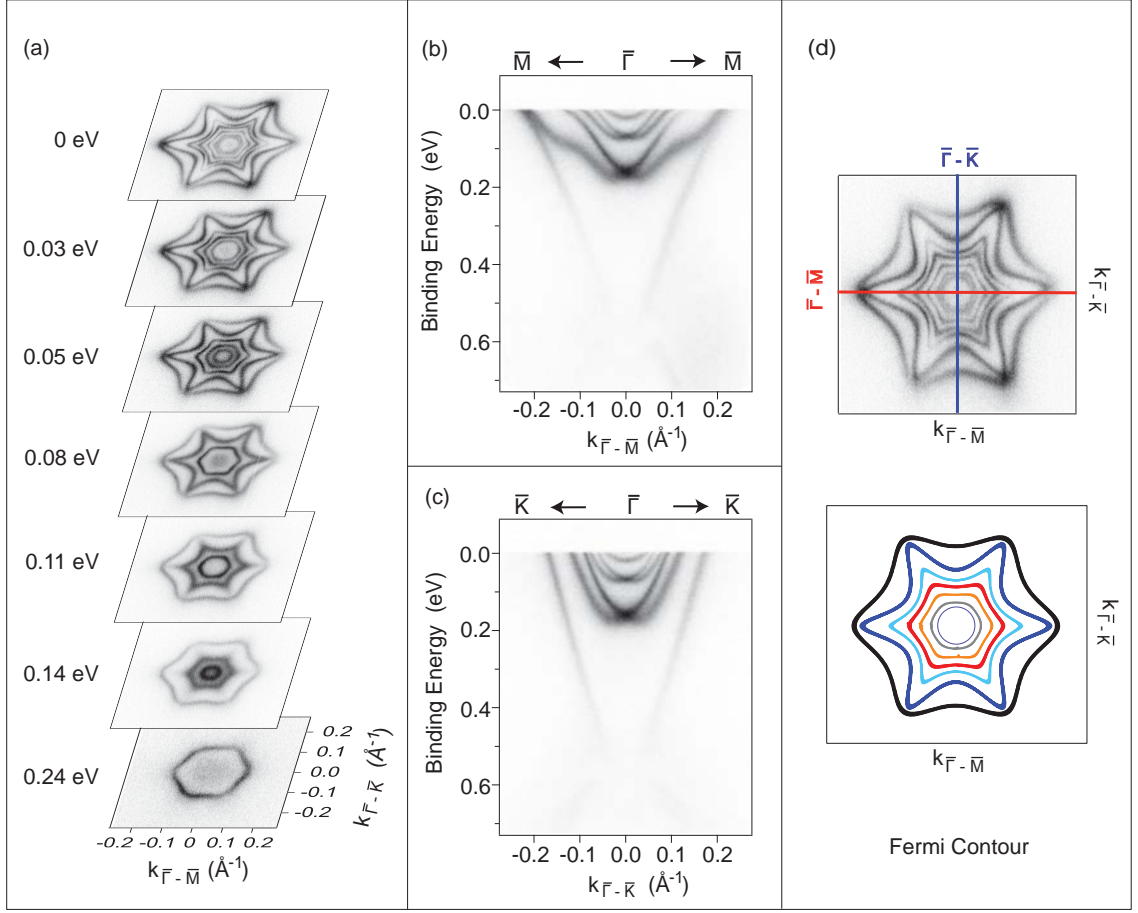


Figure 4.5: Electronic structure of electron doped $\text{Bi}_2\text{Te}_2\text{Se}$ for the high doping case as obtained by ARPES. (a) Constant energy surfaces at different binding energies. (b) and (c) Dispersion along the $\bar{\Gamma}\bar{M}$ and $\bar{\Gamma}\bar{K}$ directions, respectively. (d) On the top: Fermi contour of electron doped $\text{Bi}_2\text{Te}_2\text{Se}$. On the bottom: schematic representation of the Fermi contours. In black the topological state, in blue(light blue) the first 2DEG, in red(orange) the second 2DEG, in grey the third 2DEG.

develop the $\mathbf{k} \cdot \mathbf{p}$ Hamiltonian for the C_{3v} point symmetry up to the third order for a free-electron like band. Details on this operation are taken from Ref. [115]. The starting effective Hamiltonian is the following:

$$H(\mathbf{k}) = E_0 + \frac{\hbar^2 k^2}{2m^*} + \alpha(k_x \sigma_y - k_y \sigma_x) + \beta k^2 (k_x \sigma_y - k_y \sigma_x) + \frac{\gamma}{2} [(k_x + ik_y)^3 + (k_x - ik_y)^3] \sigma_z, \quad (4.2)$$

where σ_i are the Pauli matrices. The terms α , β , γ are the Rashba parameters up to the third order. This Hamiltonian has the maximum complexity up to the third order for this symmetry. Solving for the eigenvalues we find:

$$E(\mathbf{k}) = E_0 + \frac{\hbar^2 k^2}{2m^*} \pm \sqrt{(\alpha k + \beta k^3)^2 + \gamma^2 k^6 \cos^2 3\phi}, \quad (4.3)$$

the " \pm " sign generates the outer and inner branches and ϕ is the angle between the \mathbf{k} vector and the $\bar{\Gamma}\bar{K}$ direction. We look into the details of the effect of the different Rashba terms: α is the isotropic first order term; β is a third order isotropic term. Fig. 4.6(a-c) shows the effect of the different terms on the constant energy contour (CEC) of an isotropic free-electron-like state. The CEC is a circle before the application of the spin-orbit coupling (panel (a)). The isotropic terms splits the CEC into two concentric circles (panel(b)), as for standard surface states. The β term, acts similarly to α on the CEC but modifies the dispersion introducing a \mathbf{k}^3 asymmetry to the parabolic dispersion. Finally the introduction of the anisotropic γ term introduces the warping in the CEC (panel (c)).

From a physical point of view the α term is given by the coupling of the electron motion on the surface plane with the electric field gradient perpendicular to the surface. As discussed in Section 4.1 this gives rise to an in-plane chiral spin texture, observed in topological states and surface states. On the other hand the γ term is due to the coupling of the electron motion with the potential gradient in the plane of the surface. This gives rise to an out of plane spin component. Hence, stronger warping of the CEC is expected along with stronger out of plane polarization of the state. For the present geometry C_{3v} the warping effect has its maximum effect along the $\bar{\Gamma}\bar{K}$ direction but it must always vanish along $\bar{\Gamma}\bar{M}$, as demonstrated by the $\cos^2 3\phi$ modulation in Eq. 4.3. This is because a mirror line is present along the $\bar{\Gamma}\bar{M}$ direction and any out of plane (or radial) component of the spin is forbidden by symmetry. Inspecting the Fig. 4.6(c) the effect of the warping indeed only happens along $\bar{\Gamma}\bar{K}$. In this direction the outer branch stretches outward assuming a star shape while the inner branch compresses inward assuming an hexagonal shape. Different examples of Rashba split states can be reconnected to this geometry and shape, such as Ag/Bi [116], BiTeI [117] or the topological state of $\text{Bi}_2\text{Te}_2\text{Se}$ itself (with only one branch).

In contrast with this, the case we report of the $\text{Bi}_2\text{Te}_2\text{Se}$ 2DEG offers quite a different scenario: the two branches of a 2DEG are warped in the same direction but with different magnitude. A likely explanation of the observed dispersion is that band structure effects play a role together with spin splitting. In particular the shape of the state from which the 2DEG is generated is going to influence the dispersion of the 2DEG itself and possibly the spin splitting. To see this Fig. 4.6(d-f) present the case of an anisotropic band where the effective mass along $\bar{\Gamma}\bar{M}$ is higher than along $\bar{\Gamma}\bar{K}$. This is also the case for the bulk conduction band of $\text{Bi}_2\text{Te}_2\text{Se}$ [70]. The introduction of the isotropic Rashba term to this CEC creates again two concentric contours. Since the contour is already warped, the spin-orbit coupling actually creates a larger momentum splitting at the "tips" of the star ($\bar{\Gamma}\bar{M}$). This is justified by the fact that the momentum splitting is proportional to the effective mass of the state, even when acting isotropically. The inclusion of the anisotropic term γ (panel (f)) merely enhances the splitting far from the $\bar{\Gamma}\bar{M}$ direction as for the isotropic contour case. In the end the warping is qualitatively the same for the two branches. This picture is indeed qualitatively similar to the observed case of the $\text{Bi}_2\text{Te}_2\text{Se}$ 2DEG in Fig. 4.4(d) and Fig. 4.5(d).

To describe this quantitatively we modify the Rashba Hamiltonian of Eq. 4.2 by implementing an effective mass which is dependent of the 2D \mathbf{k} vector. Solving the eigenvalues problem for the energy, similarly to Eq. 4.3, we find:

$$E(\mathbf{k}) = E_0 + \frac{\hbar^2 k^2}{2m^*(\mathbf{k})} \pm \sqrt{(\alpha k + \beta k^3)^2 + \gamma^2 k^6 \cos^2 3\phi}, \quad (4.4)$$

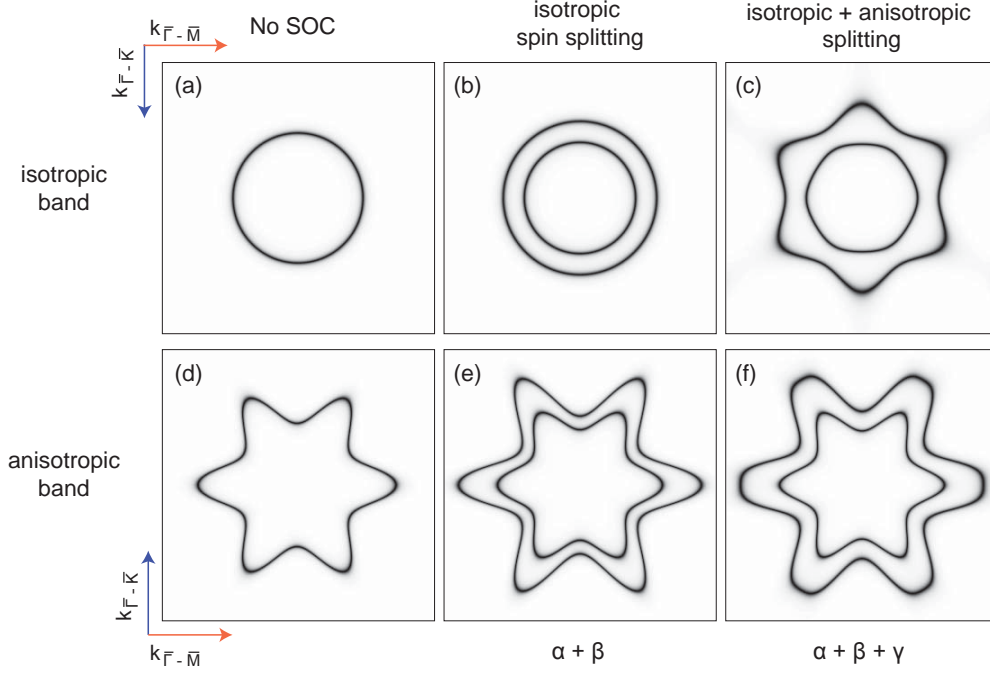


Figure 4.6: Model spectral functions of constant energy contours of a 2DEG centered at $\bar{\Gamma}$. The two cases of a isotropic original state (a-c) and anisotropic original state (d-f) are represented. (a,d) CEC with no SOC and consequently no Rashba effect. (b,c) CEC after inclusion of isotropic Rashba terms α and β . (c,f) CEC after inclusions of the anisotropic term γ .

The effective mass in the kinetic energy term is expanded as a polynomial of \mathbf{k} as

$$m^*(\mathbf{k}) = m_{0\bar{\Gamma}\bar{K}} + poly(k)\sqrt{\sin^2(3\phi)}, \quad (4.5)$$

where $m_{0\bar{\Gamma}\bar{K}}$ is the effective mass at $\bar{\Gamma}$ along $\bar{\Gamma}\bar{K}$ and $poly(k)$ is a polynomial of order 3. The $\sin^2(3\phi)$ term introduces the 6-fold anisotropy of the system maintaining the invariance under the symmetry transformations of the C_{3v} point group. In principle the form of the effective mass could acquire any complexity, i.e. with terms of non-parabolicity along the $\bar{\Gamma}\bar{K}$ direction: the present form was chosen as the simplest to reproduce the experimental data. With the expansion of the effective mass, effects of non-parabolicity and anisotropy are included while still maintaining a parametric form of the energy eigenvalues. This model results extremely useful for an easy fitting of the experimental data.

4.2.4 Analysis of the splitting

The Equation 4.4 is used to fit the 2DEGs band dispersion. The dispersion of the band is obtained by fitting energy distribution curves (EDC) and momentum distribution curves (MDC) of the ARPES data with Lorentzian functions, following the peak position throughout the bands. Given the many free parameters the direct fitting of the dispersion can give very different results. We approach the analysis by looking only, at first, at the energy splitting between the two branches of the 2DEG. The energy splitting, in fact, does not

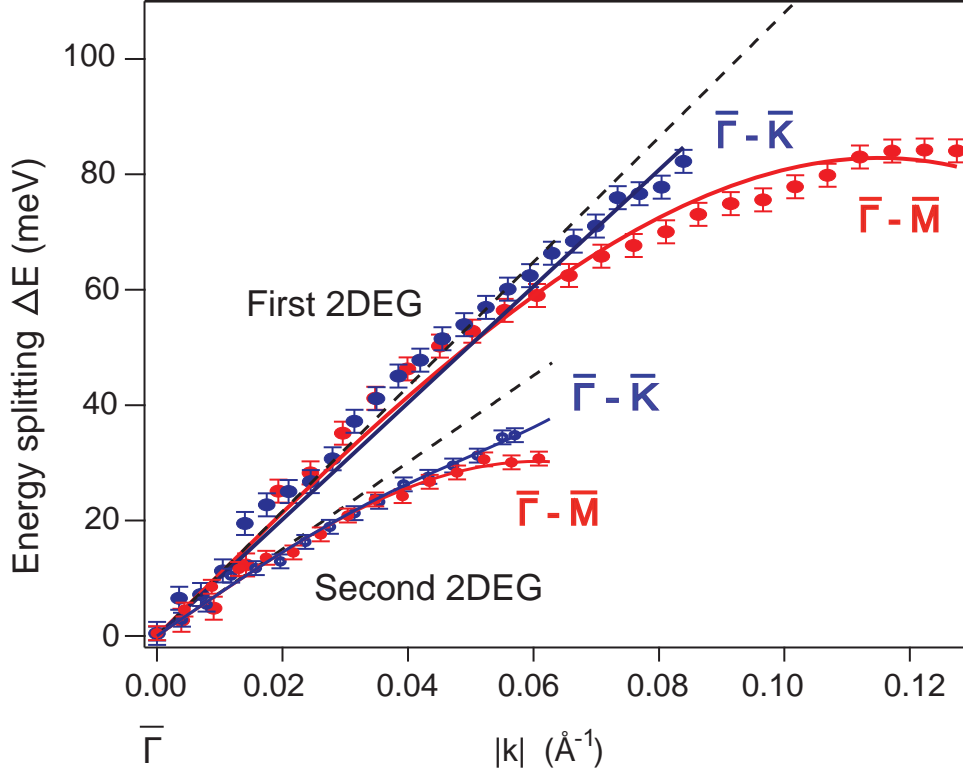


Figure 4.7: Energy splitting for the first and second 2DEGs as a function of k for the high doping case. Dispersion shown by symbols is extracted from the photoemission intensities. Solid lines represent the best fit to the splitting dispersion using Eq. 4.4. Dashed lines represent the splitting extrapolated to first order. The actual dispersion deviates from linearity decreasing at higher momentum. Both isotropic and anisotropic third order contributions are necessary for a precise description of the energy splitting.

depend on the band dispersion, but solely on the spin terms of the Rashba Hamiltonian. This reduces to

$$\Delta E(\mathbf{k}) = 2(\alpha k + \beta k^3), \quad (4.6)$$

along $\bar{\Gamma}\bar{M}$, and

$$E(\mathbf{k}) = 2\sqrt{(\alpha k + \beta k^3)^2 + \gamma^2 k^6}, \quad (4.7)$$

along $\bar{\Gamma}\bar{K}$. The α and β parameters are obtained fitting the splitting along $\bar{\Gamma}\bar{M}$. These are later kept fixed in the fit along $\bar{\Gamma}\bar{K}$ which allows for the univocal determination of γ . The result of this fit for the first and second 2DEG in the high doping case is shown in Fig. 4.7. The dashed line represents the linear contribution. The deviation of the data points at higher k from this line is quite strong and attests the importance of the inclusion of third order terms. Along $\bar{\Gamma}\bar{M}$ this deviation is solely represented by the isotropic β term. Interestingly this higher order term has negative value and acts reducing the energy splitting at higher k . The same was found in the case of the Bi/Ag(111) surface alloy from the theoretical dispersion [115]. On the other hand the diversity in the splitting between the two high symmetry directions (red and blue line in Fig. 4.7) is due to the anisotropic spin

	α (eVÅ)	β (eVÅ ³)	γ (eVÅ ³)
First 2DEG	0.54(1)	-13.1(2)	34(3)
Second 2DEG	0.37(1)	-34(1)	45(3)

Table 4.1: Values of the Rashba parameters for first and second 2DEG in the high doping case. The values are obtained by fitting the energy split of the 2DEGs

term γ which enhances the splitting at high \mathbf{k} along $\bar{\Gamma}\bar{K}$. Values of the Rashba parameters obtained are found in Table 4.1. The values are similar to the ones found for the case of the giant Rashba splitting in Bi/Ag(111) [115].

The experimental band dispersion is then fitted with Eq. 4.4 using the Rashba parameters obtained from the analysis of the energy splitting. This model is indeed able to fit the data well, as shown in Fig. 4.8. Red bands overlaid on the ARPES spectra represent the model for the two high symmetry directions. Unfortunately an accurate determination of the splitting in the low doping case was not possible because of the small energy difference and the short \mathbf{k} range available for the analysis. The model for the low doping case (Fig. 4.8(c,d)) is consequently determined by sole visual inspection. An apparent discrepancy between the model and the ARPES data can be found just above the Fermi level. In the high doping case the splitting goes to zero around $k=0.2 \text{ \AA}^{-1}$ because of the negative β term; most likely this crossing is avoided with the expansion of the $\mathbf{k} \cdot \mathbf{p}$ Hamiltonian to even higher order.

It must be noted that the aim of this model is not the perfect description of the data, but mostly to verify that the inclusion of high order band structure effects can describe the observed anisotropy, especially in the momentum splitting. This seems indeed to be the case.

We now look at the splitting in the momentum axes: the anisotropy does not look particularly pronounced in energy but it becomes very strong on the \mathbf{k} axes. Fig. 4.9 shows the k splitting Δk of the first 2DEG as a function of energy for low and high doping levels. The zero energy point is set to be the degeneracy point of the branches. Red (blue) symbols correspond to the Δk extracted from the ARPES data along $\bar{\Gamma}\bar{M}$ ($\bar{\Gamma}\bar{K}$) direction. The dashed lines represent the Δk extracted from the model.

We focus first on the high doping case (Fig. 4.9(b)). The anisotropy is small close to the bottom of the band up to ≈ 0.05 eV. Above this energy the anisotropy increases up to 0.08 \AA^{-1} of difference between the two high symmetry directions and it seems to saturate closer to the Fermi level. This effect is related to the non-parabolicity of the band: Along $\bar{\Gamma}\bar{M}$ the dispersion deviates from the parabolic behaviour assuming a negative effective mass, while the inner branch maintains the positive curvature. For this reason the k splitting is greatly enhanced, reaching 0.09 \AA^{-1} . Closer to the Fermi level the outer branch assumes again a positive curvature. This effect is even more striking in the low doping case: here the Fermi level is tuned to barely reach the point of divergence. At the Fermi level the Δk along $\bar{\Gamma}\bar{M}$ is as high as 0.06 \AA^{-1} while it remains almost zero in $\bar{\Gamma}\bar{K}$, as shown in the inset of Fig. 4.9(a).

The case presented here represents a new way to enhance the spin-orbit splitting. The combination of non-parabolicity of the states and spin-orbit coupling pushes the two branches far apart in the momentum space, yet maintaining the energy splitting constrains

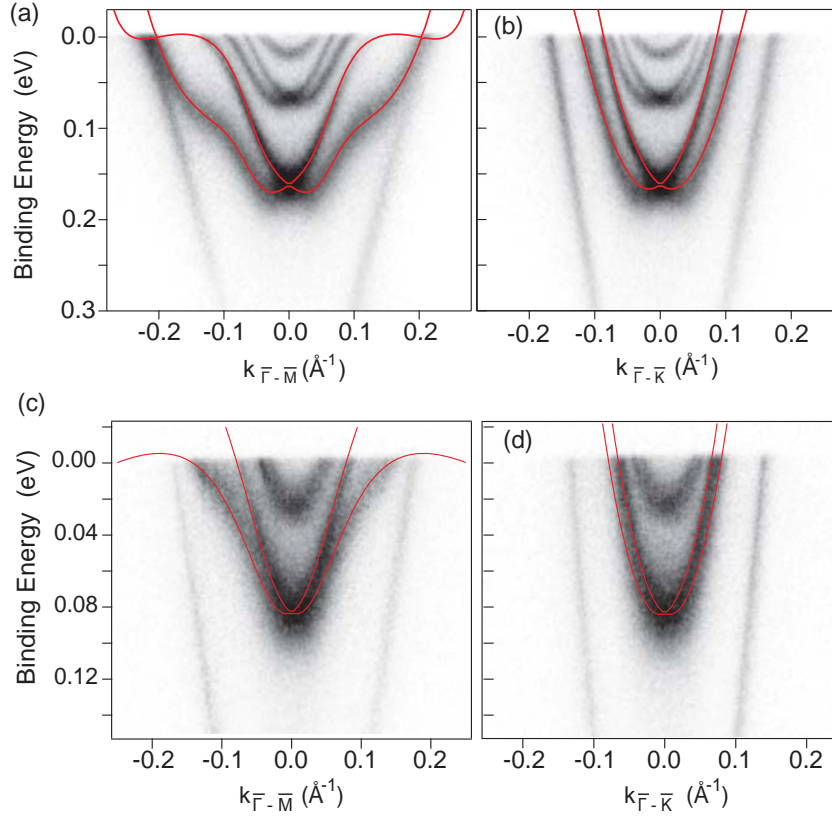


Figure 4.8: Photoemission intensity cuts of the 2DEG in the high doping (a,b) and low doping (c,d) cases along (a,c) $\Gamma\bar{M}$ and (b,d) $\Gamma\bar{K}$. The red lines show the fitting of the first 2DEG branches using the model described in Eq. 4.4.

of the Rashba effect. While the energy splitting is used as a measure of the spin-orbit coupling strength, it is the k -splitting at the Fermi level that matters for transport experiments or for devices, such as the Datta-Das spin transistor [24]. In principle the 2DEG could be controlled directly through gating, allowing to finely tune the population of the state and, in this case, the Fermi surface shape and the k -splitting. Moreover the creation of two bands with opposite spin that behave as electrons and holes, respectively, could provide a way to create spin cumulation in devices, i.e. through the Hall effect. This could give rise to interesting and tunable spin-dependent transport phenomena in these systems paving the way to a new kind of anisotropic spin transport and a new way to enhance the spin splitting at the Fermi level.

4.3 The case of Bi_2Te_3

Similar experiments and analysis have been performed on the Bi_2Te_3 material. A 2DEG is induced at the surface of Bi_2Te_3 by rubidium deposition. The experimental procedure is the same as for $\text{Bi}_2\text{Te}_2\text{Se}$, but the experimental conditions differ as described below.

ARPES data are collected at SGM3 beamline at ASTRID2. Bi_2Te_3 samples are cleaved

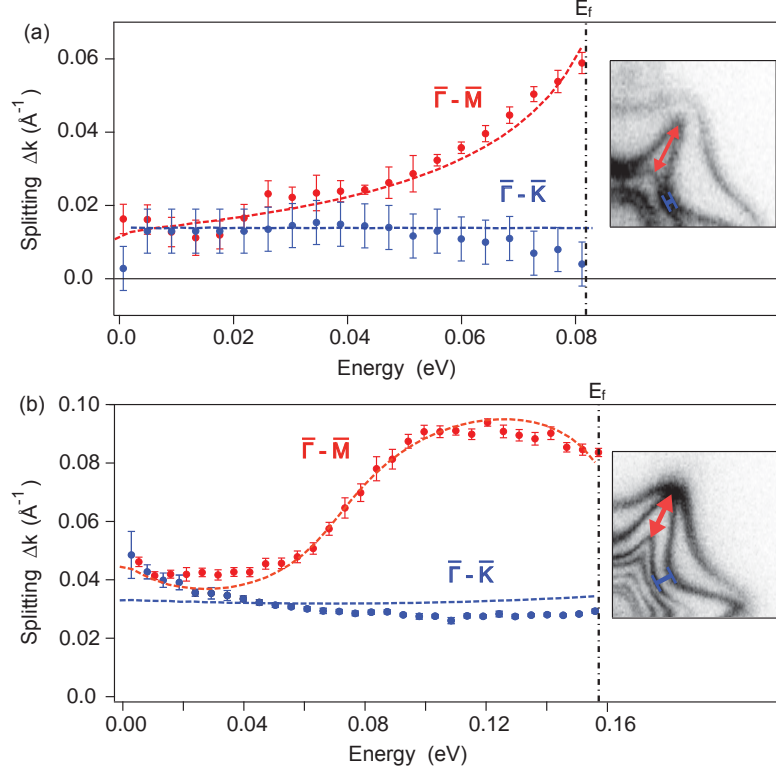


Figure 4.9: k splitting of the first 2DEGs as a function of energy for the low doping (a) and high doping (b) case. The zero energy is set to be at the degeneracy point of the two branches. Symbols represent the splitting amplitude obtained by fitting of the photoemission spectra. Dashed lines represent the k splitting extracted from our model (dispersion shown in Fig. 4.8). In both cases the combination of anisotropic band structure and Rashba spin splitting well describes the experimental results. In the insets: section of the Fermi surface that shows the anisotropy of the spin splitting at the Fermi level.

in vacuum. The Bi_2Te_3 appears to be slightly p-doped (note that the samples used here are different from the ones used in Chapter. 3). The chemical potential of the as-cleaved sample is found to be strongly dependent on the cleave conditions. For a "good" cleave the Fermi level cuts through the top of the valence band, while for other cases this would cross at the bottom of the conduction band. This is ascribed to the band bending, probably related to the presence of adsorbates on the surface [102]. The temperature during deposition varies for different trials but is maintained below 170 K. The measurement temperature is lower than 90 K. The photon energy used is 19.1 eV. The light has linear horizontal polarization. In this setup this is perpendicular to the rotation axes. The out of plane component of the polarization is zero for normal incidence geometry.

Fig. 4.10 shows the ARPES of the Rb-doped Bi_2Te_3 for the highest doping level reached. Very similarly to the $\text{Bi}_2\text{Te}_2\text{Se}$ case two 2DEGs are created at the surface because of the localized electron donation. These 2DEGs reside inside the topological state contour. The shape of the constant energy contours (Fig. 4.10(a)) resembles the case of $\text{Bi}_2\text{Te}_2\text{Se}$: the warping of both branches is in the same direction with the tips of the hexagonal stars along $\bar{\Gamma}\bar{M}$. A strong trigonal symmetry of the photoemission intensity is due to matrix elements

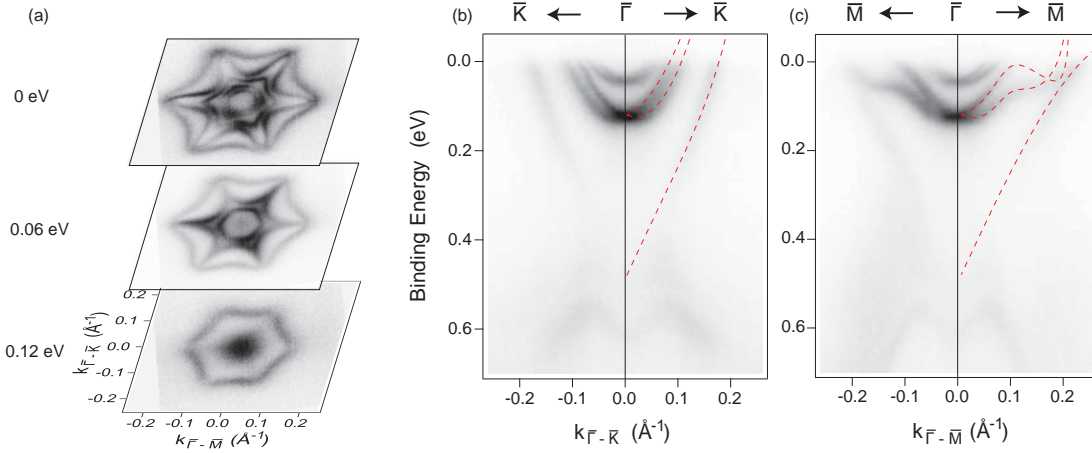


Figure 4.10: Electronic structure of electron-doped Bi_2Te_3 for the high doping case as obtained by ARPES. (a) Constant energy surfaces at different binding energies. (b),(c) Dispersion along the $\bar{\Gamma}\bar{M}$ and $\bar{\Gamma}\bar{K}$ directions, respectively. On the right side red dashed lines represent the dispersion of topological state and first 2DEG as obtained from Eq. 4.4 fitted to the ARPES data.

effects dictated by the orbital character of the states.

The data are analysed in the same way as thoroughly explained for $\text{Bi}_2\text{Te}_2\text{Se}$ and similar conclusions can be drawn. The electric field on the surface is calculated by looking at the shift of the Dirac cone. The shift with respect to the freshly cleaved sample is 0.20 eV. This value is specific for the attempt shown here. Different attempts started with much lower chemical potential and after doping the shift of the Dirac cone can be as high as 0.38 eV.

A more complex parametric formula was necessary to fit the $\bar{\Gamma}\bar{M}$ dispersion, expanding the polynomial in Eq. 4.5 to the sixth order. The result of the fitting is partially shown in Fig. 4.10 over-imposed on the ARPES data. Again the lack of higher order spin-orbit interaction terms induces a degeneracy around 0.18 \AA^{-1} along $\bar{\Gamma}\bar{M}$. The values of the Rashba parameters are $\alpha = 0.46(2) \text{ eV\AA}$, $\beta = -17(4) \text{ eV\AA}^3$, γ is not definable in such short k -range. The β parameter is negative reducing the splitting. Inspecting the dispersion in Fig. 4.10(c) the effect of non-parabolicity is here even stronger than for $\text{Bi}_2\text{Te}_2\text{Se}$: along $\bar{\Gamma}\bar{M}$ the outer branch of the first 2DEG warps outward at 0.06 eV of binding energy assuming an almost horizontal dispersion. The dispersion of the outer branch has the same qualitative shape of the bulk conduction band projected on the (111) surface at Z as shown by red line in Fig. 3.2(c). This effect can be better described by looking at the k -splitting shown in Fig. 4.11. The splitting along $\bar{\Gamma}\bar{K}$ remains constant because of the parabolic shape. The Δk at the Fermi level is $0.0247(4) \text{ \AA}^{-1}$. The evolution of Δk along $\bar{\Gamma}\bar{M}$ is even more drastic than for $\text{Bi}_2\text{Te}_2\text{Se}$. From 60 to 70 meV above the degeneracy point, the Δk increases with a steep slope from $0.025(4)$ to $0.093(4) \text{ \AA}^{-1}$ while it remains constant in the regions above and below. The Δk at the Fermi level is even greater than for $\text{Bi}_2\text{Te}_2\text{Se}$ ($0.084(1) \text{ \AA}^{-1}$) despite the weaker effective doping.

The step increase in anisotropy suggests that Bi_2Te_3 could be a even better candidate for anisotropic spin transport. It provides the possibility to tune the chemical potential around the singularity point within only 10 meV. To evaluate the possibility of fine tuning

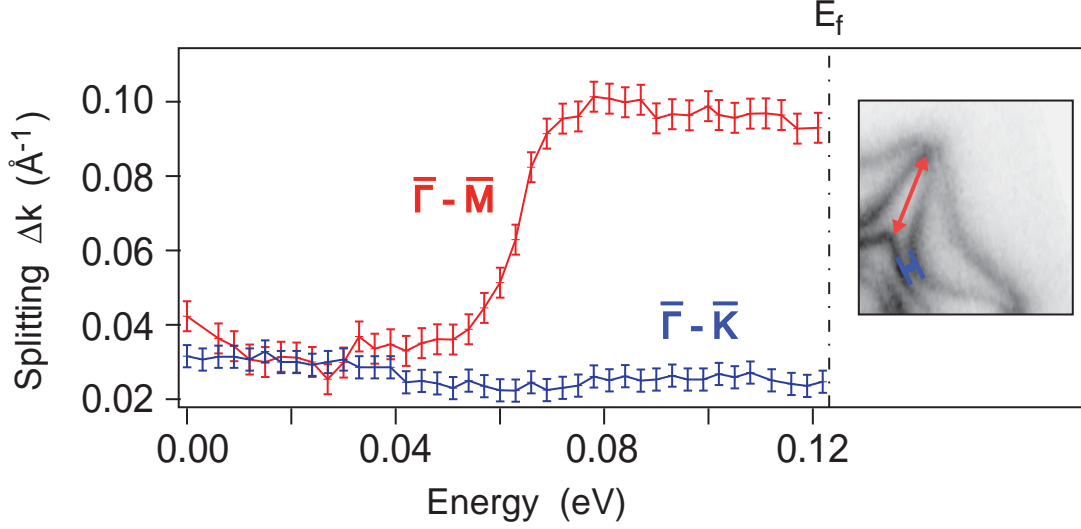


Figure 4.11: k -splitting of the first 2DEGs as a function of energy. The zero energy is set to be at the degeneracy point of the two branches. Symbols represent the splitting amplitude obtained by fitting of the photoemission spectra. In the insets: section of the Fermi surface that shows the anisotropy of the spin splitting at the Fermi level.

around the singularity point a low doping case for Bi_2Te_3 is presented in Fig. 4.12. Panel (a) shows the Fermi surface. Due to time effect (i.e. radiation damage, adsorbates) in the quality of the sample, the image has been symmetrized around the $k_{\bar{\Gamma}-\bar{K}} = 0$ line. Two 2DEGs are populated. The Fermi level is tuned to be just above the singularity point as visible from the dispersion along the high symmetry directions in panels (b) and (c). The model dispersion (red dashed lines in Fig. 4.12) has been built by visual inspection. The linear Rashba constant α is enough to describe the dispersion in this small k range. The k splitting at the Fermi level is $0.08(1) \text{ \AA}^{-1}$, only slightly lower than for the high doping case. This value is extremely big for such low doping and it is similar to the one obtained for $\text{Bi}_2\text{Te}_2\text{Se}$ in the high doping case. The application of a gate voltage that leads to an effective energy shift as small as 10 meV can here switch on and off a 0.08 \AA^{-1} spin splitting at the Fermi level.

We define the spin splitting anisotropy quantity as following:

$$\text{Anisotropy} = \frac{\Delta k_{\bar{\Gamma}\bar{M}} - \Delta k_{\bar{\Gamma}\bar{K}}}{\Delta k_{\bar{\Gamma}\bar{M}} + \Delta k_{\bar{\Gamma}\bar{K}}} \cdot 100. \quad (4.8)$$

The high and low doping case for $\text{Bi}_2\text{Te}_2\text{Se}$ have anisotropy equal to 48(2)% and 70(16)% respectively. For Bi_2Te_3 we find the values 58(6)% and 76(20)%. The anisotropy itself is systematically larger for Bi_2Te_3 than for $\text{Bi}_2\text{Te}_2\text{Se}$, as expected by the larger effective mass along $\bar{\Gamma}\bar{M}$. Moreover the lower the 2DEG filling, the higher is the anisotropy, if the singularity point in the dispersion is reached. In the case of Bi_2Se_3 the anisotropy is very small, in the order of 8-9% [102].

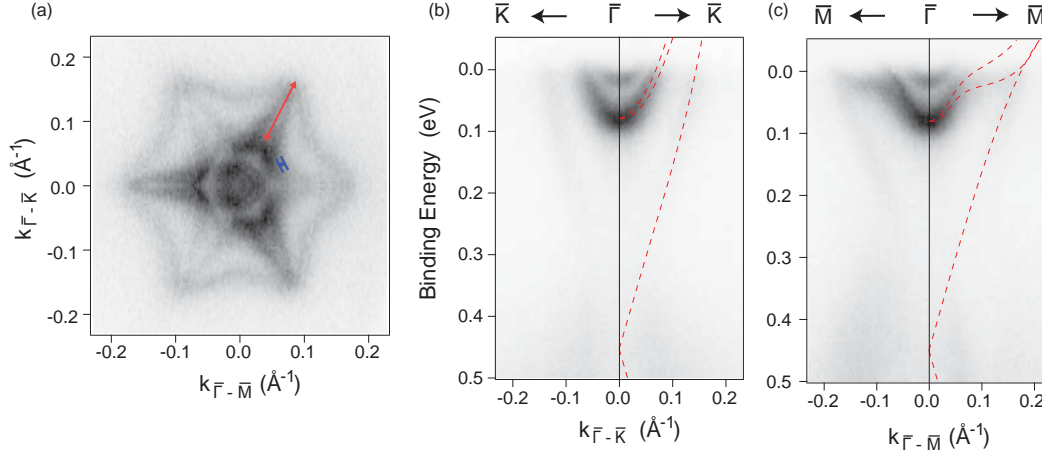


Figure 4.12: Electronic structure of electron-doped Bi_2Te_3 for the low doping case as obtained by ARPES. (a) Fermi surface. Red and blue markers point out the different spin splitting along $\Gamma\bar{M}$ and $\Gamma\bar{K}$. (b),(c) Dispersion along the $\Gamma\bar{M}$ and $\Gamma\bar{K}$ directions, respectively. On the right side red dashed lines represent the dispersion of topological state and first 2DEG as obtained from Eq. 4.4 by fitting the parameters to the ARPES data.

4.4 An outlook

So far we have simply described the dispersion of the 2DEGs on telluride TIs and the splitting in energy and momentum. This has been modelled by simple $\mathbf{k} \cdot \mathbf{p}$ Hamiltonian expanded to the third order where we included anisotropy and non-parabolicity. This model efficiently described the states' dispersion and unveiled the interplay of band structure and spin-splitting. Despite its effectiveness the model Hamiltonian is implemented "ad-hoc" and mostly serves the purpose of understanding and fit experimental results in an easy way but it cannot be used for *a priori* predictions. An important point to discuss is the spin texture that derives from such unconventional 2DEGs. The spin orientation is strongly connected with the electron momentum and, hence, its dispersion. Knowledge of spin-texture is of extreme importance for spin-transport experiments or devices. Spin resolved ARPES on these systems are very desired for this purpose. Unfortunately this is very challenging from an experimental point of view: a system like the 2DEG of the $\text{Bi}_2\text{Te}_2\text{Se}$ requires to resolve up to seven different bands in only 0.2 \AA^{-1} . Momentum resolution of 0.015 \AA^{-1} is the minimum estimated necessary. Such characteristics are still rare to be found in spin-ARPES systems. Efforts in performing spin-resolved experiments are presently ongoing.

In the 2DEGs of the tellurides the spin texture has the potential to be very complex. In a Rashba coupled system the spin and the momentum directions are locked together. The interplay of band structure effects and high order Rashba coupling will surely influence the spin texture. A few considerations can be expressed on the basis of the observed spin splitting. The spin components of an electron can be calculated from its expectation value given the electron wave function. In the case of a free electron state the first order Rashba induces a chiral spin texture with only in-plane radial component. The constant energy

contours of the two branches have opposite chirality (see Fig. 1.3). The first order derives from the interaction between the electron motion in plane and the gradient of the electric field perpendicular to the plane. While this is true for the free electron state, the spin texture can be very different in an anisotropic state. We can imagine this in the very simple terms of effective magnetic field. In the reference frame of the moving electrons the perpendicular electric field is "felt" as an effective magnetic field through the simplified Lorentz transformation $B'_{\perp} = -v \times E_{\perp}$. As a result of the vector product the B field is perpendicular to both the electric field and the electron velocity. In the Fermi surface picture the velocity ($v \propto \nabla_k E$) is always perpendicular to the contour in k -space. In this simple picture the electron spin, aligning with the effective magnetic field, will always be tangential to the constant energy contour.

For the strongly anisotropic states, as the 2DEGs on the tellurides, this can induce a component radial respect to the \mathbf{k}_{\parallel} vector. In the case of our 2DEGs this has an additional effect. As we have seen the non-parabolicity in the dispersion affects the constant energy contours such that the contours for inner and outer branch are very different (i.e. the image of an hexagon inside a star in $\text{Bi}_2\text{Te}_2\text{Se}$). Hence the two spin split branches can carry spin directions non-opposite to each other, collapsing the usual convention of spin-up/spin-down states. We can speculate that this effect will increase the interband scattering outside the high symmetry directions.

It was also discussed how the description of the 2DEGs dispersion requires the inclusion of third order terms, β and γ in the Rashba Hamiltonian for the C_{3v} point symmetry. It is known that the γ term introduces an out of plane spin component S_z [73]. This is modulated in \mathbf{k}_{\parallel} with the radial angle as $\cos(3\theta)$. The out of plane component is maximum along $\bar{\Gamma}\bar{K}$ and vanishes at $\bar{\Gamma}\bar{M}$. To have a better insight in the role of the third order terms one can develop the $\mathbf{k} \cdot \mathbf{p}$ calculation to find an explicit expression for the coefficients. These expressions can be found in Ref. [115] in Eq.22 and 23 for β and γ respectively. The isotropic term derives again from the interaction with the electric field gradient perpendicular to the plane. On the other hand the anisotropic term is related to the in-plane gradient of the field. Indeed the characteristic features in the dispersion and in the spin-texture introduced by this term reflects the pseudo-6 fold symmetry of the surface plane. It is well know that this is an important factor for Bi_2Te_3 and $\text{Bi}_2\text{Te}_2\text{Se}$. For these materials the spin warping has been extensively studied on the topological states [73, 118, 119]. Because of the linear dispersion and the nature of the topological state the pure Rashba Hamiltonian for a Dirac state can efficiently describe the state dispersion. The reason of the anisotropy of the 2DEGs is instead mostly due to the anisotropic effective mass. Thinking of a tight binding approach, one can think of the band structure anisotropy in plane due to the interaction of one atom with the first six neighbours. It is intuitive to think that the band structure anisotropy is qualitatively related to the same in-plane potential that provokes the strong spin warping, present both in the 2DEG and the topological state. Hence the presence of strong out of plane component in the 2DEG is expected. The value found for the $\text{Bi}_2\text{Te}_2\text{Se}$ 2DEG is one order of magnitude bigger than for the Bi/Ag surface alloy [115].

An additional point of interest is the role of the orbital character and its relation to the spin texture. The third order Rashba parameters are obtained from the admixture of orbitals of p_z and p_{xy} character. The role of orbital character in the spin texture was already highlighted for the topological states [120]. Recent work on the Rashba-like system BiTeI showed how the Rashba splitting can be orbital-character dependent [117, 121]. This

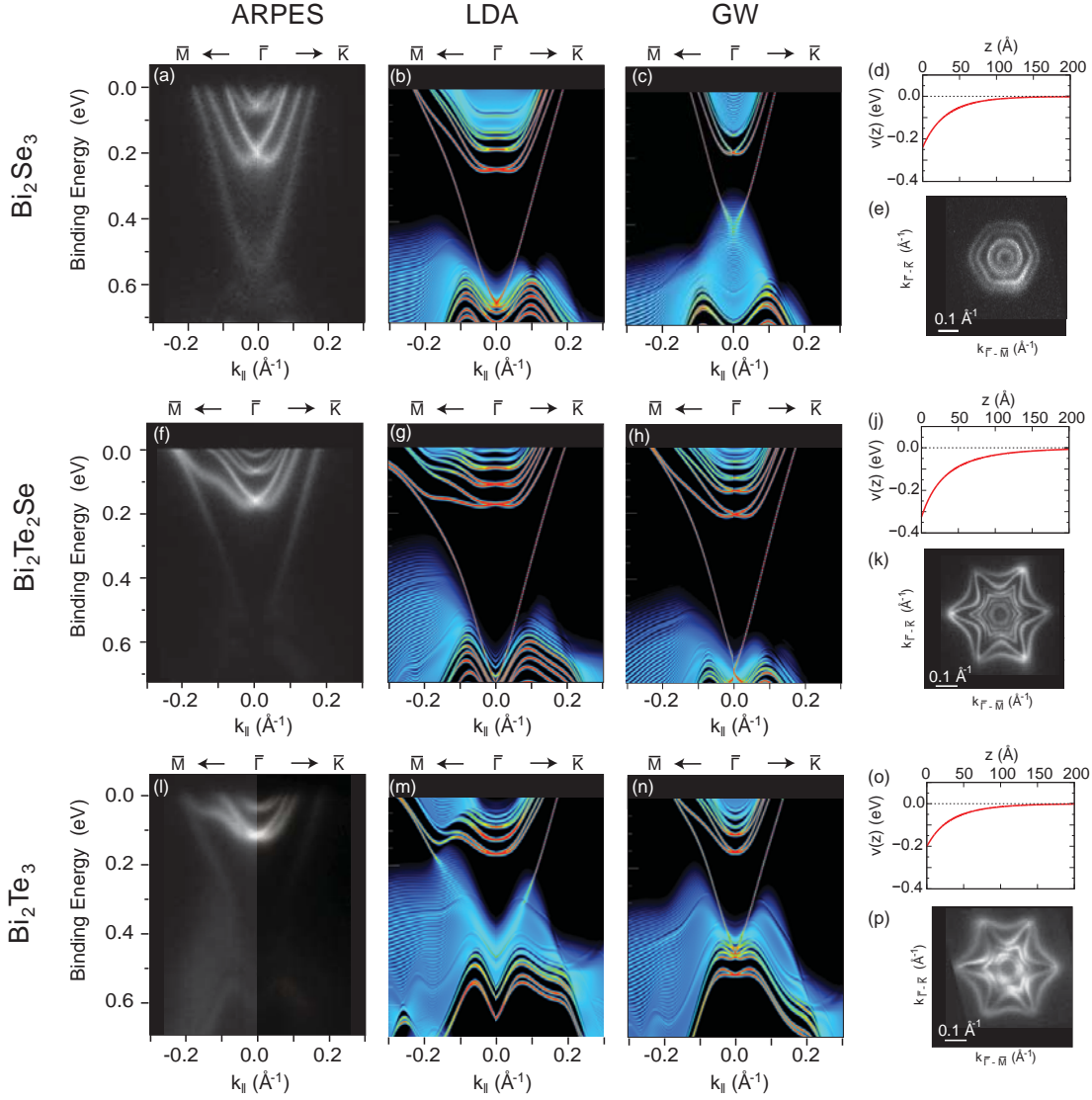


Figure 4.13: Low energy electronic structure of gated Bi_2Se_3 (a-e), $\text{Bi}_2\text{Te}_2\text{Se}$ (f-k) and Bi_2Te_3 (l-p) along the high symmetry directions. 2DEGs are populated close to the Fermi level. (a,f,l) ARPES dispersion along $\bar{\Gamma}\bar{M}$ (left) and $\bar{\Gamma}\bar{K}$ (right). Data on Bi_2Se_3 from concession of Marco Bianchi [103] (b,g,m) Surface tight binding calculation for TIs with surface potential, obtained within the LDA framework. The surface potential used, shown in (d,j,o), is chosen to compare directly with ARPES results. (c,h,n) Surface tight binding calculations using the GW Hamiltonian matrix. (e,k,p) ARPES Fermi surfaces.

studies revealed that the spin-orbit coupling promotes orbital hybridization and locks a specific spin-texture to specific orbitals. This enriches the spin texture away from the normal predictions of the simple Rashba model. Spin-ARPES and dichroism data, coupled with *ab initio* calculations, are strongly desired.

We obtained some preliminary results from *ab initio* calculations. The result is summarized in Fig. 4.13. The calculations were performed using both LDA and GW. The slab

Hamiltonian derived from DFT calculations has been used to create a surface tight binding calculation with band bending. The method is similar to the one used in Ref. [122]. The potential gradient was calculated via coupled Schrödinger-Poisson equation. [Calculations performed by P.King, St Andrew University, M.S.Bahramy, RIKEN-ASI, Saitama and I. Aguilera, FZ Jülich] The surface potential for the three TIs (Fig. 4.13(e,k,p)) is chosen to match with the ARPES data. The value of the electric field at the surface is obtained by fitting the shift of the Dirac point upon Rb adsorption. The dispersion for the series Bi_2Se_3 , $\text{Bi}_2\text{Te}_2\text{Se}$ and Bi_2Te_3 is shown along $\bar{\Gamma}\bar{M}$ and $\bar{\Gamma}\bar{K}$ as obtained by ARPES (panels(a,f,l)), by LDA (panels(b,g,m)), and by GW (panels(c,h,n)). The experimental Fermi surfaces are also shown for comparison (panels(e,k,p)). The comparison of the ARPES data reveal a coherent increase in the anisotropy towards the Bi_2Te_3 , as previously discussed. In particular for Bi_2Se_3 the anisotropy is very small. The same trend is seen for the warping of the topological state. This seems to prove that the in-plane potential affects similarly the spin warping and the bulk band structure. The comparison of the experimental results with the calculations reveals an overall better agreement with GW with respect to LDA. The GW consistently reduces the effective mass of the 2DEG along $\bar{\Gamma}\bar{M}$ and at the same time it reduces the anisotropy. In particular in the cases of Bi_2Se_3 and $\text{Bi}_2\text{Te}_2\text{Se}$, the quasi particle correction introduced by GW properly corrects the dispersion of the 2DEG and it appears much more similar to the experiments. This might indicate a strong contribution of quasi particle renormalisation for these materials, which is not accounted for in LDA. In Bi_2Te_3 the GW fails to reproduce the nearly horizontal dispersion at the singularity.

Further orbital and spin calculation are in progress. It is our hope that the complementary experimental efforts will help drawing a complete picture of the spin-orbit role in the anisotropic 2DEGs found on TIs.

4.5 Exploring the magnetic properties with magnetic surface doping

The topological properties of TIs rely on the presence of time reversal symmetry in the system. As discussed in Chapter 1.3 the topological state is said to be protected by TRS. When this is broken the spin degeneracy at $\bar{\Gamma}$ can be lifted, creating an energy gap and generating massive fermions. TRS also protects spin-polarized currents from backscattering. The intrinsic tie between topological insulators and time reversal symmetry raises the interest in coupling the magnetic degree of freedom, odd under TRS, with TIs. In specific a magnetization in the direction perpendicular to the surface is predicted to open the gap at the Dirac point [123, 124]. Magnetic atoms on the surface or embedded in the bulk of topological insulators have been extensively studied for their magnetic orientation, magnetic interaction mechanism and effect on the electronic structure [125–127]. Attempts in creating a net out of plane magnetization have been made incorporating Mn atoms in the bulk of Bi_2Se_3 , which created spectroscopic evidence of a gap opening in the TS [128]. However structural disorder from impurities also acts towards a gap opening [129] and the matter remains unclear. Under these circumstances a local magnetic doping on the surface appears to be a simpler way to study the magnetic interactions on the TS. Experiments where Fe atoms are deposited on the surface of Bi_2Se_3 showed contrasting results, where the issue of surface quantization of valence band states plays a major role in the definition of a energy gap at the Dirac point [130, 131]. It was then found out by X-ray magnetic

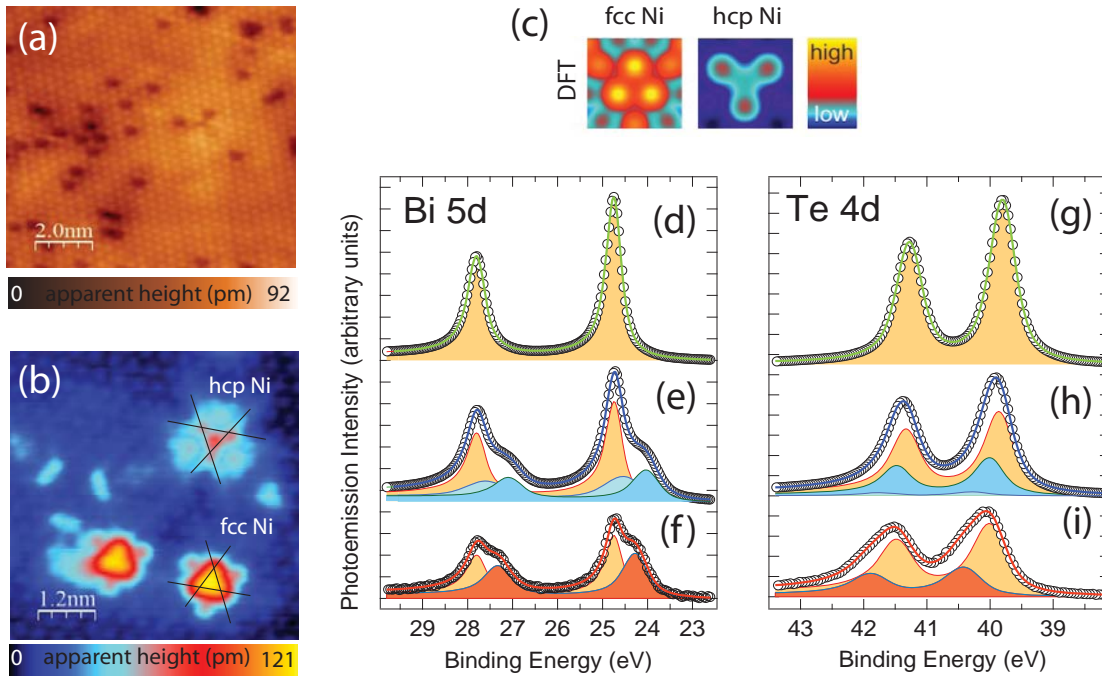


Figure 4.14: (a) STM topograph of the pristine Bi₂Te₂Se surface ($U = 150$ mV, $I = 50$ pA). (b) Atomically resolved image of 1% Ni (red dots) on Bi₂Te₃, with single Ni atoms occupying two different adsorption sites ($U = 350$ mV, $I = 400$ pA, composite of original and Fourier altered topograph in order to enhance atomic contrast). The lines trace the surface Te atom rows. (c) Calculated STM topographs of Ni fcc and Ni hcp using the Tersoff-Hamann-model ($U = 400$ mV). For both stackings, the z-scale covers the same range. (d-i) XPS core level spectra for Bi 5d (left column) and Te 4d (right column) for pristine Bi₂Te₂Se (d) and (g), as well as after deposition of 0.6 ML Fe [(e) and (h)] and 0.6 ML Ni [(f) and (i)], respectively. Fits represent decompositions into Bi and Te doublets. Upon 3d metal deposition, a chemical shifted component develops with respect to the main pristine peak. For Fe two components are visible on Bi 5d.

circular dichroism (XMCD) that Fe assumes in-plane magnetization on Bi₂Se₃ [132].

Here we probe the magnetic and electronic properties of magnetic doping on the topological insulator Bi₂Te₂Se by locally depositing d-shell elements Ni and Fe with the combined use of XMCD, STM, ARPES and DFT calculations. Similar experiments were also performed on Bi₂Te₃; these yielded basically the same conclusions as for Bi₂Te₂Se and we will therefore focus only on the latter. STM experiments were performed and analysed in the Wiesendanger Group at Hamburg University. XMCD and photoemission core-levels analysis were performed by Jan Honolka and Martin Vondráček at Prague University. The author performed XMCD and photoemission experiments and analysed the photoemission data.

4.5.1 Adsorption sites

A Bi₂Te₂Se single crystal was cleaved in vacuum by scotch-tape technique and cooled down to the measurement temperature ($T = 1.5$ K for XMCD, $T = 7$ K for STM and $T \approx 90$ K for ARPES). Nickel and iron were deposited in diluted concentrations on the cleaved surface using outgassed EBE evaporators. The low temperature is necessary to avoid clustering of

the adatoms. The evaporation rate was calibrated for ARPES and XMCD by depositing sub-monolayer (ML) quantities of adatoms on clean Pt single crystal and pyrolytic graphite and determining the coverage with STM topography.

Fig. 4.14(a) shows a STM image of the as-cleaved surface; atomic resolution reveals the hexagonal lattice of the Te-terminated surface, because the cleave happens in the VdW gap. Darker spots with apparent height of 20 pm are attributed to Se_{Te} antisite defects [133]. Except for the sparse Se_{Te} defects Bi_2Te_2Se exposes the same termination of Bi_2Te_3 . Fig. 4.14(b) shows a high resolution topograph of Ni atoms adsorbed on the Bi_2Te_3 surface. The Ni atoms assume two distinct appearances because adsorbed into two different hollow sites of the Te surface. Terser-Hamann-model calculation of the STM topography (Fig. 4.14(c)) confirm the observed apparent heights and shapes for the Ni adsorbed on the hcp and fcc sites.

Core level spectra and ARPES are acquired at the SGM3 beamline at ASTRID2. Bi_{5d} and Te_{4d} core levels are acquired on pristine Bi_2Te_2Se and after 0.6 ML of Fe and Ni using photon energy $h\nu = 100$ eV. The results are shown in Fig. 4.14(d-i), the spectral features are fitted with Doniach-Šunjić functions convoluted with a Gaussian. Both Bi and Te related spectra develop strong shoulders upon deposition of Ni and Fe, consistent with the picture of the Ni and Fe to sit between the two topmost layers giving strong chemical shift to both Bi and Te. Se_{3d} peaks (not shown) do not develop additional components because they are too deep in the bulk to interact with the adatoms. On the Bi core levels the Ni generates a single component shifted by 0.46 eV, while Fe generates two distinct components at 0.23 eV and 0.72 eV respect to the pristine position. This findings reveal the tendency of iron to sit on both hcp site, above the Bi atom with stronger chemical shift, and fcc hollow site with weaker chemical shift. Ni on the other hand strongly favours the fcc sites. Defect analysis in STM reveals a Ni_{hcp}/Ni_{fcc} ratio of 0.2 and the Fe_{hcp}/Fe_{fcc} ratio of 0.6, confirming the conclusions drawn by XPS.

4.5.2 Magnetic properties

The magnetization of the adatoms is investigated by XMCD. XMCD experiments have been performed at the X-Treme beamline at Swiss Light Source [134]. The XMCD technique is based on the selection rules in the photon absorption using circular polarized light. X-ray absorption spectra (XAS) using circular right ($\sigma+$) and left ($\sigma-$) polarised light are acquired while imposing a magnetic field B in the same direction as the light. The photon energy is varied around an adsorption edge so to excite electrons from a core level to the empty valence states. The absorption intensity profile is a probe of the empty valence states. Selection rules dictate that ($\sigma+$) and ($\sigma-$) light excite electrons with opposite spin-orbital texture. In the case of Fe and Ni we use a range of photon energy to probe the $L_{2,3}$ absorption edge from p states to the empty d-states. The XMCD signal is the difference between the absorption spectrum acquired with ($\sigma+$) and ($\sigma-$) light. This difference reflects the asymmetry in the spin and orbital character of the d states, and hence, its magnetic ground state.

A magnetic field of 6.8 T is used to align the spin direction of the transition metals. The sample is first aligned with the surface normal parallel to the B field and the light. Absorption and XMCD for Fe and Ni on Bi_2Te_2Se are summarized in Fig. 4.15. The amount of adsorbates is in the order of 1% which is in the single impurity limit, when each single impurity can open an energy gap around itself [123]. Spectra are acquired in current drain

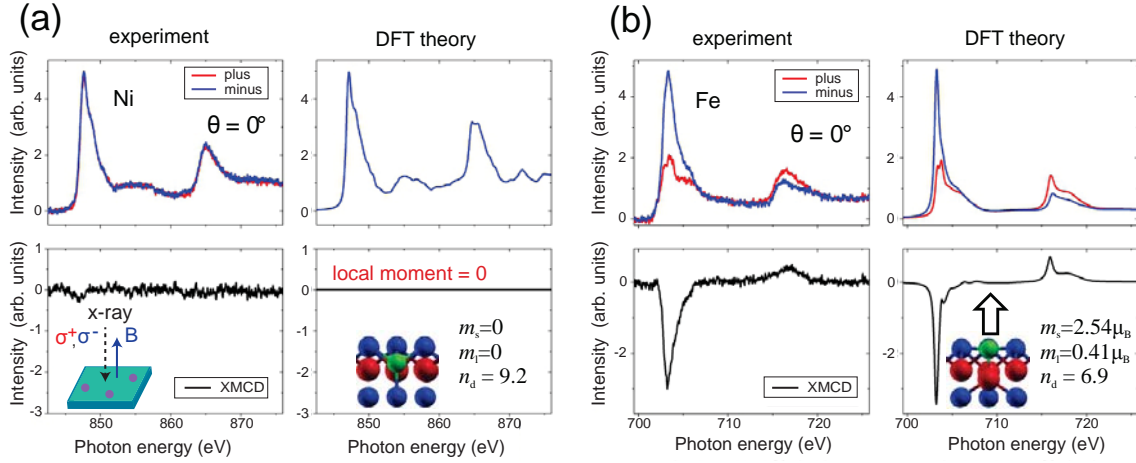


Figure 4.15: (a) and (b): Ni and Fe $L_{2,3}$ XAS data for positive ($\sigma+$) and negative ($\sigma-$) circular polarization in polar geometry and resulting XMCD signals below (left panels). Measurements were done in the impurity regime at low temperatures of $T = 2\text{K}$ and polar fields of $B = 6.8\text{ T}$. Right panels show respective spectra simulated from DFT theory using the relaxed geometry shown as insets showing exceptional agreement with our experimental results. Although both Ni and Fe show partially filled d-shells with occupancies $n_d = 9.2$ and $n_d = 6.9$, respectively, only Fe develops finite local orbital and spin moments, while the vanishing Ni XMCD signal reflects efficient moment quenching as predicted by theory.

mode. The absence of oxygen is tested with XAS on the O K-edge. Both Ni and Fe XAS spectra reveal clear absorption edges with fine structure, typical of half filled d-shells weakly hybridized with the environment. The two principal peaks derive from absorption from the two spin-orbit split initial p-states. Interestingly Ni does not show any net magnetization. The $\sigma+$ and $\sigma-$ signals are equal leading to zero signal in the XMCD (Fig. 4.15(a)). Ni is a borderline element between high-spin $3d^8 4s^2$ and low-spin $3d^9 4s^1$ configurations and thus magnetic ground state configuration is highly sensitive to interaction with the surface. The magnetization of Ni is quenched on the surface of $\text{Bi}_2\text{Te}_2\text{Se}$. The DFT calculations of the XAS spectrum is in excellent agreement with the experiment. The occupancy of the d-shell is $n_d = 9.2$.

Different is the case of iron (Fig. 4.15(b)): the strong asymmetry in the XAS spectra leads to a significant XMCD signal. Fe develops a net magnetization contrarily to Ni. Repeating the same experiment rotating the sample surface 60° from the light and magnetic field yields the same results for Ni but a dampened XMCD signal for Fe unveiling the out of plane nature of the magnetization. Comparison with the DFT calculation gives an occupancy factor $n_d = 6.9$. We find a situation where magnetic adatoms have a out-of-plane easy axes of magnetization on top of TI $\text{Bi}_2\text{Te}_2\text{Se}$.

4.5.3 Effect of magnetic adatoms on the electronic structure

In order to study the effect of the magnetic adatoms on the electronic structure of $\text{Bi}_2\text{Te}_2\text{Se}$ ARPES experiments are performed. Data presented in Fig. 4.16(a,b,d) are acquired using photon energy of $h\nu = 21\text{ eV}$ at the SGM3 beamline at ASTRID2. Photoemission spectra of the Dirac cone of $\text{Bi}_2\text{Te}_2\text{Se}$ are shown at different coverages for Ni (panel (a)) and Fe (panel (b)). The effect of both metal atoms is a consistent electron doping of the surface,

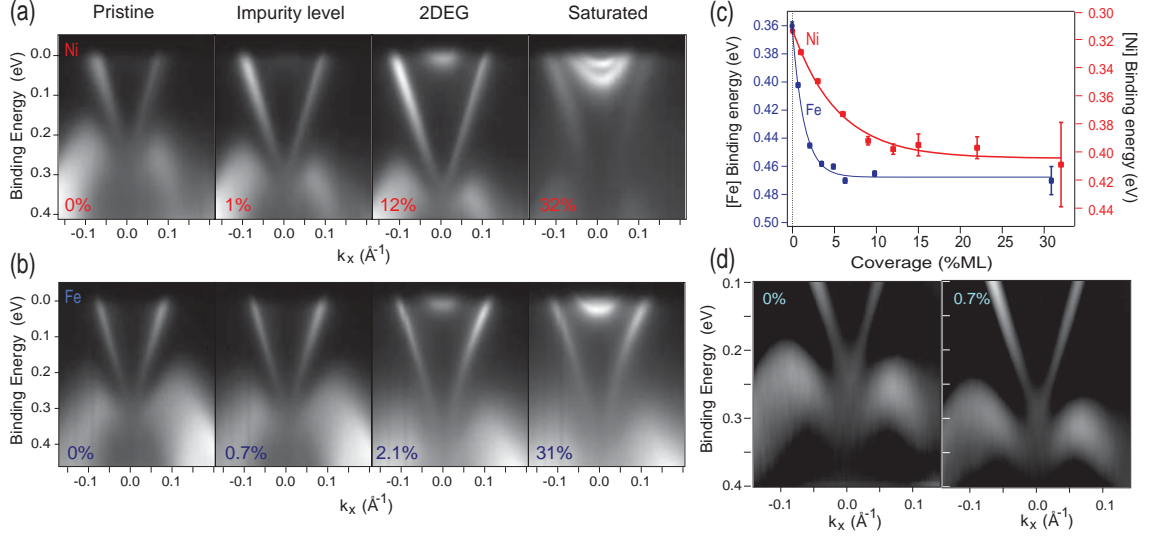


Figure 4.16: (a) Photoemission intensity of Bi₂Te₂Se for the pristine sample (left) and for an increasing amount of Ni(1%,12%,32%) on the surface. (b) Photoemission intensity of Bi₂Te₂Se for the pristine sample (left) and for an increasing amount of Fe(0.7%,2.1%,31%) on the surface. In the impurity level regime the Fermi level is exclusively crossed by the topological state. A 2DEG appears at higher coverages up to saturation. The evolution of the Dirac point for the two cases is shown in (c). (d) Second derivative of the photoemission spectra for Fe-doped Bi₂Te₂Se around the Dirac point. Pristine sample and 0.7% coverage are shown. No modification of the Dirac point is detectable.

not dissimilarly to the effect of Rb seen in Section 4.2.1. Images are chosen to present the different stages in the adsorption of the metal atoms. In the pristine sample the Fermi level cuts through the Dirac cone and no bulk carriers is detected. In the single impurity level stage, at around 1%(0.7%) of coverage, the material is still a good semiconductor. At this stage the sample is representative of the system studied with XMCD, we can conclude that Fe on Bi₂Te₂Se is an excellent system to study the interaction of electronic and magnetic properties in TIs. In fact the iron has an out of plane easy axes of magnetization and the charge carriers purely come from the topological state making the study of topological state mediated magnetic interaction, such as RKKY, a real possibility [123].

When the amount of metal adatoms becomes bigger, a 2DEG is populated on the surface. Further doping results in a saturation state where the spectrum blurs up because of disorder and impurity states. The doping efficiency has been estimated by following the position of the Dirac point for different coverages, the result is shown in Fig. 4.16(c). The use of different scales for the case of Ni and Fe doping is due to the different initial position of the Dirac point (which depends on each cleave). In both cases the doping magnitude follows an exponential law, shown with a line, that brings it to fast saturation. The Fe saturates faster after only 6% of coverage while Ni has lower electron doping power and saturation is achieved after 12% of ML.

One open question that remains is the lifting of degeneracy at the DP by magnetic ordering. Thanks to the XMCD results we do not expect the Ni to have an impact on the TS. More interesting is the case of Fe. Unfortunately the DP in Bi₂Te₂Se lies sunken in the bulk valence bands rendering the detection of the Dirac point an arduous task. We plot the

second derivative of the ARPES spectra for pristine $\text{Bi}_2\text{Te}_2\text{Se}$ and for the iron doped case at single impurity level in Fig. 4.16(d). The Dirac point is found in both cases very close to the valence band. No gap opening is detectable in the limits of our resolution. Similar analysis on higher coverages also never hints towards a gap opening.

We must point out that this does not exclude a gap from being opened but simply that this is not detected. The temperature might be not low enough to develop a ferromagnetic order on the surface. Also any gap smaller than the experimental resolution will not be visible. A recent theoretical study reports that the detection of a magnetic doping induced energy gap in the TI would be made virtually impossible by the presence of resonant impurity state in the gap [135].

At last we report that similar experiments have been carried out by us using copper as adatom as well. However XMCD results revealed that the Cu assumes a filled shell d10 configuration making it fairly uninteresting for magnetic properties. The effect of copper on the low energy electronic structure is similar to the Ni and Fe, acting as electron donor.

Chapter 5

Interfacing a 2D and a 3D topological insulator - Bi/Bi₂Se₃

Elementary bismuth is one of the most studied materials for its remarkable electronic structure. It is a natural semimetal with giant carriers mobility and strong spin-orbit coupling. Similarly to Bi₂Se₃ it has rhombohedral structure $R\bar{3}m$. There are two atoms per unit cell. Along the [111] direction it can be pictured as a stacking of more strongly bonded bilayers which gives easy access to the the (111) surface by cleaving, as illustrated in Fig. 5.1(a-b). Our interest is to see what happens when the dimensionality of the system is reduced. The lowest practically feasible dimension is achieved by building a single bilayer of bismuth. This shall be treated here as a two dimensional system as there is no translational symmetry in the perpendicular direction. The single bilayer has buckled honeycomb structure

In 2006 Murakami proposed that a single bilayer bismuth would be a quantum spin Hall insulator (or 2-D topological insulator) by using the Kane-Mele model for honeycomb lattice with strong spin-orbit coupling [3, 137]. In order to host a quantum spin Hall phase (QSH) three main ingredients are needed: time reversal symmetry, band inversion and insulating phase (band gap). Koroteev *et al.* studied the thickness dependent electronic band structure of the Bi(111) by first principle calculation. According to their results a gap opening is possible only for a single bilayer while adding a second bilayer already closes the gap. The gap in the bilayer is opened at Γ and it is about 0.2 eV [138]. The band inversion was studied by Murakami first and by Wada *et al.* later: Since the inversion symmetry remains in the bilayer itself, the topological considerations can be again simplified by looking at the parity of the occupied bands. Similarly to Bi₂Se₃, a single inversion at Γ is found (see Fig. 5.1(c)), resulting in an odd \mathcal{Z}_2 invariance $\nu = 1$, predicting the presence of helical Dirac states confined at the edges [136, 137]. In Fig. 5.1(d) the calculated dispersion of the metallic edge state is shown.

The theoretical prediction for this material are remarkable but its experimental realization is not an easy task: The research for a good substrate capable to host a well ordered structure and that can give access to the electronic properties and maintains the topological properties of the Bi bilayer is necessary. The first realization of the bilayer has been reported by Hirahara *et al.* in 2011 by using the three-dimensional strong topological insulator Bi₂Te₃ as substrate. In that work the surface/interface electronic structure is characterized by ARPES and supported by DFT calculations [139]. Higher quality of

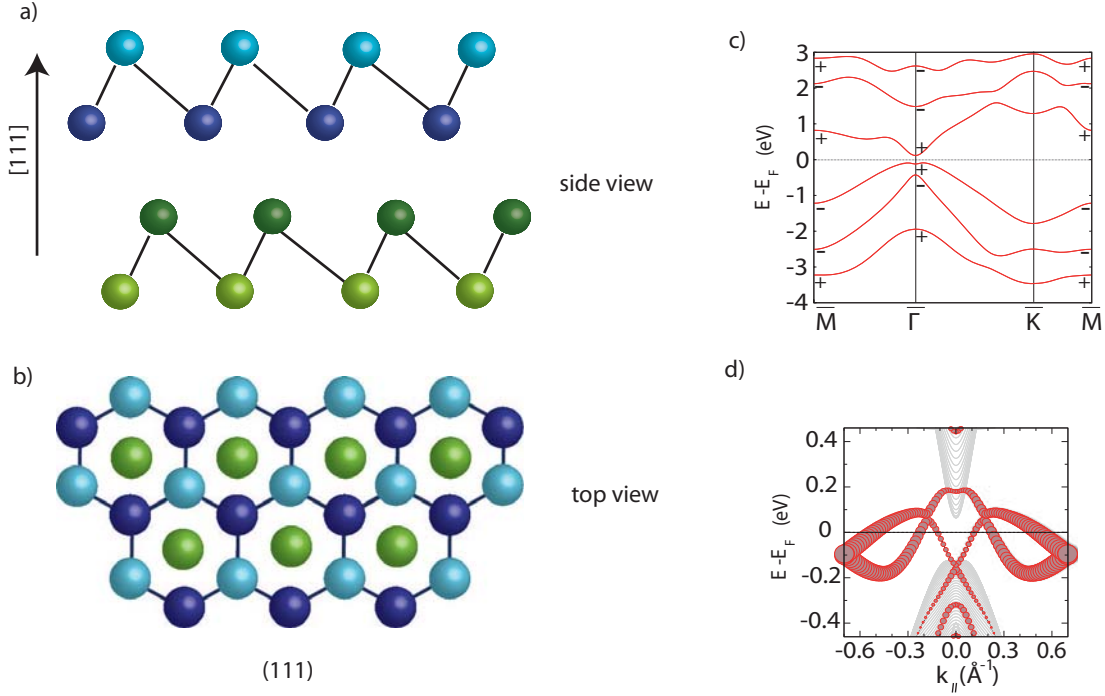


Figure 5.1: Schematic representation of the structure of bismuth in side view along the [111] direction (a) and top view ((111) surface) (b). Blue spheres represent atoms in the top bilayer and green spheres, the bottom bilayer. (c) Calculated band structure for the single bismuth bilayer with calculated parity (+ even, - odd) at TRIMs. A single band inversion at $\bar{\Gamma}$ is present. After Ref. [136]. (d) Calculated dispersion of the topological edge states of Bi bilayer. After Ref. [136].

ARPES data was then collected by Miao *et al.* who investigated both the Bi/Bi₂Se₃ and Bi/Bi₂Te₃ systems [140].

5.1 The electronic structure of the interface

This work is dedicated to the study of the electronic structure at the interface between the two dimensional topological insulator Bi bilayer and the three dimensional TI Bi₂Se₃. The reason for studying this system (Bi/Bi₂Se₃) is principally two-fold: 1- The first objective is mainly application-oriented: 2-dimensional materials can obviously not be simply synthesized as bulk but they must be grown on a substrate. The choice of the substrate turns out to be of crucial importance. Depending on the interaction between the substrate and the material the surface electronic properties can be drastically changed; a strong interaction can lead to high states hybridization at the interface while for "free-standing" films the electronic structure is not affected by the substrate. One of the primary experimental objectives would be obtaining the "free standing" bilayer, where the influence of the substrate is virtually zero, in order to gain easy access to the topological helical edge states. Unfortunately up to date there is not a clear idea on how to decouple the bilayer from any substrate. Yet the use of a semiconducting substrate can still grant the access to the eventual edge states as long as the energy gap of the bilayer does not close. In order to

grow the Bi in the [111] direction, the substrate should have a similar lattice structure, this is the case of Bi₂Se₃. 2- The second objective has more general physical interest: what happens to the surface states and the topology when two TIs are interfaced is still not fully understood and the theories are sometimes contrasting [141–143]. It was shown that a selective elimination of the topological states can occur at the interface according to the states' position in the reciprocal space and to the helicity. In the Bi/Bi₂Se₃ system we couple two strong TIs, both with parity inversion at Γ , but the topological considerations for the two materials lie in two different dimensions.

We perform ARPES, STM and FT-STs on the system. We use DFT calculations to help unravelling the electronic structure. The connection between theory and experiments is obtained by performing Joint Density of State simulations. This work is a collaboration with Hamburg University and the Forschungszentrum in Jülich. All the STM-STs experiments have been performed in Hamburg in the Wiesendanger group by Andreas Eich and collaborators, the DFT calculations are carried out in Jülich by Gustav Bilmayer. ARPES results and the Joint density of States simulations have been carried out and computed by the author.

5.1.1 ARPES characterization

The ARPES measurements have been performed at the SGM3 beamline at ASTRID synchrotron in Aarhus. As first step we measure the ARPES spectrum on the cleaved substrate (Fig. 5.2(a-b)). Data are acquired using 18 eV photon energy. The sample is cleaved at room temperature and measured at $T \sim 80$ K. The main feature is the topological surface state that assumes the classical Dirac cone like shape. The Dirac point is situated at $E_B = 0.49(0.04)$ eV. The bulk valence band is visible as a shaded area above $E_B = 0.7$ eV. A 2DEG appears below the Fermi level up to $E_B = 0.21$ eV. The Fermi surface in Fig. 5.2(b) is circular for the 2DEG while the topological state shows a hint of hexagonal warping.

The Bi bilayer is grown by MBE using a commercial electron beam evaporator. The deposition temperature is set around 200-240 K. The as grown surface is too disordered and the sample was then post-annealed to $T \sim 453$ K to let the film rearrange its structure. The annealing has a positive effect on the surface quality but evaporates part of the bismuth leaving the surface terminated with both the bilayer and the pristine Bi₂Se₃.

Fig. 5.2(c) shows the angle-integrated core level spectrum of Bi 5d and Se 3d peaks before (blue line) and after (red line) the deposition. The higher energy doublet stems from the selenium; the peaks simply decrease in intensity with the deposition due to coverage of the substrate surface. The doublet of Bi 5d also is reduced in intensity with the growth of the film but two new red-shifted peaks appear. These additional features are naturally attributed to the respective 5d core levels of the Bi bilayer. In order to obtain a rough estimation of the coverage we look at the relative intensities of the Bi 5d(3/2) peaks assigned to bilayer and substrate in the red curve. Using the bilayer height obtained from STM (see section 5.2) and an inelastic mean free path λ of 4.5 Å (the electrons' kinetic energy is around 50 eV) we estimate a coverage of 10%

Fig. 5.2(d-e) show the ARPES signal for the Bi/Bi₂Se₃ system along the two high symmetry directions cuts: $\bar{\Gamma}-\bar{K}$ and $\bar{\Gamma}-\bar{M}$. The spectrum is a superimposition of two different signals, the substrate and the bilayer islands, as expected. The signal from the Bi₂Se₃ is still very clear, in particular the topological state and the M state. Some of the features that rise from the bilayer are clearly identifiable off normal emission: in particular

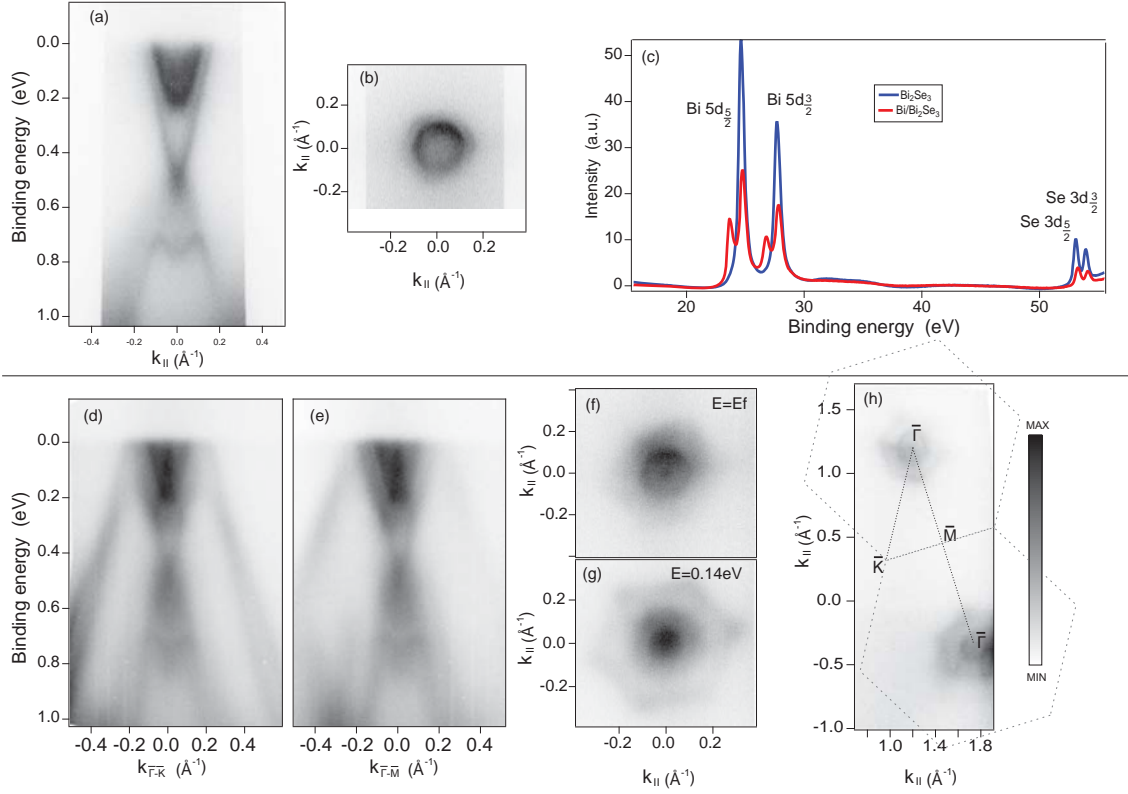


Figure 5.2: (a) Photoemission intensity of Bi₂Se₃ around $\bar{\Gamma}$. (b) Fermi surface of Bi₂Se₃. (c) Core levels photoemission of Bi₂Se₃ and Bi/Bi₂Se₃ as a function of binding energy. (d,e) Photoemission intensity of Bi/Bi₂Se₃ around $\bar{\Gamma}$ along $\bar{\Gamma}\bar{K}$ and $\bar{\Gamma}\bar{M}$ directions. (f,g) Constant energy contours at $E_B=0$ and 0.14 eV for Bi/Bi₂Se₃. (h) Cut at constant energy $E_B=0.37$ eV for two consecutive Brillouin zones shows that the CEC is hexagonally warped along the $\bar{\Gamma}\bar{K}$ direction.

two sets of outer bands are dispersing downwards. As it will be discussed in Section 5.1.2 these bands stem from the upper valence band of the Bi bilayer. These lateral bands are split in two branches with different group velocities and cross each other along the $\bar{\Gamma}\bar{K}$ direction around 0.32 eV. We inspect the isotropy of these states by the constant energy cuts of Fig. 5.2(f,g): The CEC is hexagonally shaped and gets larger at higher binding energies. Fig. 5.2(h) shows a constant energy cut of a big dataset with two adjacent Brillouin zones acquired with photon energy 70 eV. By connecting the two $\bar{\Gamma}$ points we can find the Brillouin zone boundaries and define the high symmetry directions. The corners of the hexagonal CECs are pointing in the $\bar{\Gamma}\bar{M}$ direction.

Looking at the ARPES data, we can identify an additional band around the $\bar{\Gamma}$, crossing the Fermi level at $\mathbf{k}_{\parallel} = 0 \text{ \AA}^{-1}$. The low spectral weight makes it difficult to distinguish but it can be seen in the Fermi surface as a single higher intensity point at $\bar{\Gamma}$. A careful inspection of constant energy contours reveals a linear dispersion for this state. This result will be more clear when looking at the DFT calculations.

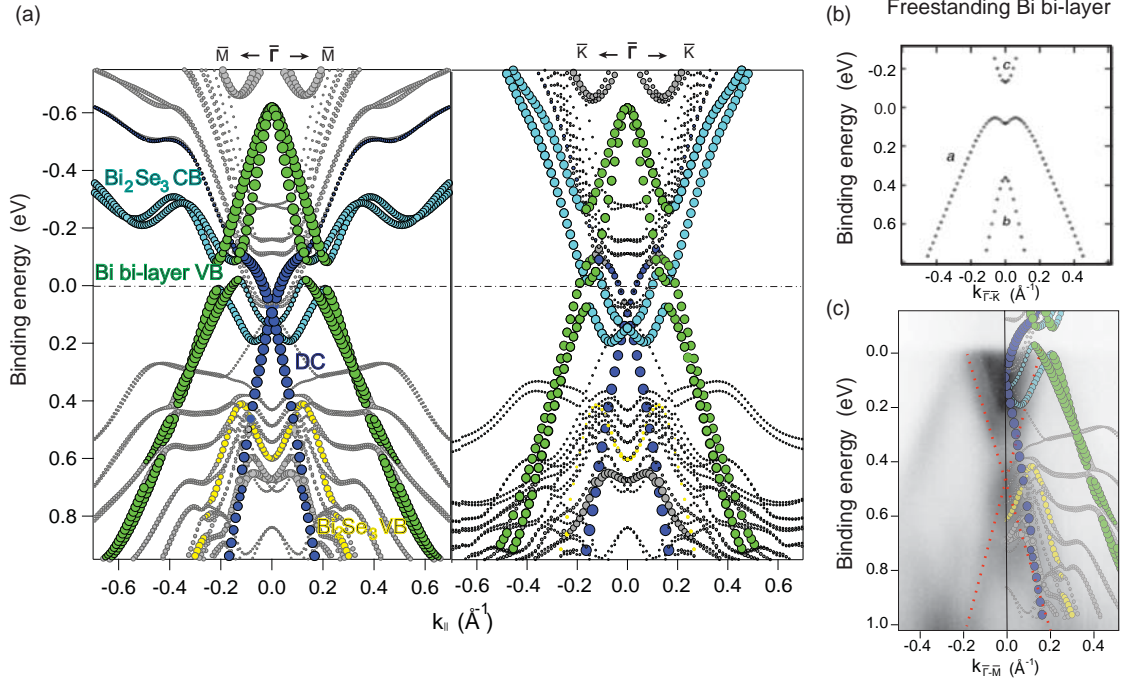


Figure 5.3: (a) DFT slab calculation for Bi/Bi₂Se₃ along $\bar{\Gamma}-\bar{M}$ and $\bar{\Gamma}-\bar{K}$ directions. The size of the data points is proportional to the localization of the state on the bilayer, different colours are used in relation to the origin of the bands. (b) Electronic structure of the free-standing Bi-bilayer from first principle calculations. After Ref. [139]. (c) ARPES spectrum of Bi/Bi₂Se₃ compared to the DFT calculations. The red dotted line is a guide for the eye representing the TS of the pristine substrate.

5.1.2 DFT calculations

In order to unravel the origin of the electronic structure at the interface between the Bi bilayer and the Bi₂Se₃, we perform DFT slab calculations. The DFT calculations were performed using the full-potential linearised augmented plane wave method. The sample was modelled with a slab made of six QL plus the Bi bilayer on top. The distance between the bilayer and the substrate was relaxed to match with the experimental dispersion. Further details are given in Ref. [6].

We plot the results for the electronic structure around $\bar{\Gamma}$ along the two high symmetry directions in Fig. 5.3(a). Each energy eigenvalue is plotted as a circle of finite size, the size is proportional to the wave function localization of the state on the Bi bilayer. This type of data visualization helps to distinguish the bands localized on the surface/interface from the bands buried in the bulk. To facilitate in the recognition of the states the main bands (with high surface localization) are plotted with different colours according to the origin of the states itself. The band in green is the Bi bilayer upper valence band, it displays a slight spin split. The light blue band stems from the Bi₂Se₃ conduction band and it shows a pronounced splitting below the Fermi level. In yellow we outline an M-shaped state coming from the Bi₂Se₃ valence band. And at last we highlight in blue a Dirac cone-like state. In order to fully understand what happens at the electronic structure at the interface we can picture the following real space scenario: The bilayer is strongly influenced by the coupling with the substrate. From the free standing Bi bilayer, whose band structure is pictured in

Fig. 5.3(b), the bilayer is here interfaced with Bi₂Se₃, in this situation we assist to a strong charge transfer from the film to the substrate; this charge transfer results in a p-doping of the bilayer and the subsequent n-doping of the substrate. By looking at the electronic structure this effect is expressed in the position of the maximum of the bilayer valence band: for the free standing case, the VB maximum is localized few meV below the Fermi level, for the interacting system it is found more than 0.6 eV above the Fermi level. The opposite effect is visible for the substrate conduction band whose minimum drops to 0.2 eV below Fermi level. A similar charge transfer effect was already proposed by Chen *et al.* for the Bi bilayer grown on Bi₂Te₃ and was attributed to the difference in work function between the film and the substrate [144]. Further indication of this phenomenon comes from the Rashba-like splitting found for the Bi₂Se₃ CB and the Bi bilayer VB.

The band outlined in light blue is a two dimensional electron system at the interface that derives from the substrate conduction band. From the calculations it appears that VB and CB are interpenetrating each other around the Fermi level and they hybridize around the crossing point, creating a small gap in $\bar{\Gamma}\bar{M}$ direction. It must be noted that there is no actual absolute hybridization gap opening because the gap is closed along $\bar{\Gamma}\bar{K}$.

We focus our attention on the band marked in dark blue. The appearance of the new Dirac cone state at the interface was already observed in previous works on similar systems [139, 140, 145, 146] and it was described as an interface spin-polarized Dirac cone that coexists with the Bi₂Se₃ (Bi₂Te₃) topological state. We argue here that the formation of this state is due to the hybridization of the bismuth lower valence band with the Bi₂Se₃. The strong spin-orbit coupling splits the Bi state in two spin polarized bands. The Bi₂Se₃ topological state is merged at the interface with this interface Dirac cone, or is shifted downward (the Bi₂Se₃ topological state that appears as light open marker belongs to the opposite face of the slab). If the two were to coexist, an even number of states would encircle the $\bar{\Gamma}$ TRIM and the non-trivial topology of the system would be phenomenologically broken. Since the topological considerations for a 3D and a 2D material lie in different dimensions the surface topology is expected to remain non trivial.

The ARPES data are compared to the result of the DFT calculations for the occupied states in Fig. 5.3(c): The bilayer valence bands show the same dispersion behaviour and a band crossing occurs in fact at ~ 0.2 eV below the Fermi level. The blue Dirac cone gives rise in the spectrum to the high intensity point seen on the Fermi surface. Because of the large spectral broadening it is not possible to disentangle the Rashba split of the conduction band.

5.2 FT-STs and JDOS simulations, an indirect probe of complex structures

STM topography on the system reveals a flat film surface with sparse impurities (Fig. 5.4(a)). The bismuth growth is confirmed to be coherent on the substrate along the [111] direction. The in-plane lattice constant results compressed of about 10% and the film thickness is 6.3 Å. Theoretical predictions confirm that the strained bilayer grown on Bi₂Se₃ maintain the non trivial topology [147]. The distance between the bilayer and the substrate (4.4 Å) is found to be markedly higher than the inter-layer distance in bulk bismuth.

In order to further clarify the electronic structure of the system and to better confirm the theoretical prediction brought forward by the DFT calculations, we study the electronic

structure via FT-STs.

5.2.1 Quasi particle interferences

Differential conductance maps have been acquired in the presence of few point impurities for different energies from -1 eV up to +0.4 eV (energies are here referred as $E-E_F$ as they are negative for occupied states and positive for positive biases and unoccupied states). The spectroscopic maps are acquired in presence of a finite number of point impurities, these scattering centres are mostly crystal imperfections or single adsorbates.

Fig. 5.4(b-i) shows the differential conductance maps acquired in the same region of the topography in panel (a), for positive and negative biases. In all the maps quasi-particle interference patterns around the impurities are visible. At high negative bias the QPI assumes the form of localized wrinkles with hexagonal geometry around the impurities. At low bias the hexagonal geometry is maintained but the QPI signal is much stronger. The wavelength of the modulation is also larger, symptom of smaller scattering vectors. The situation is a bit different at positive bias where the modulation pattern is less discernible. As discussed in Section 2.2 by performing the Fourier transform of the differential conductance maps the QPI is mapped in the reciprocal space and it can be related to the electronic structure of the surface at constant energy. By carrying the information into the k -space we can make a signal analysis disentangling all the frequencies (scattering vectors) present in the modulation pattern.

The Fourier transformed images of the differential conductance maps are shown in Fig. 5.4(j-q). The images have been symmetrized according to the 6-fold symmetry of the surface. We analyse at first the general trend of the features: All negative bias QPIs have two or more distinct concentric regular hexagonal features. In general the outer hexagon decreases its size closer to the Fermi level. For positive biases the regular hexagonal shape is replaced by a more warped contour. This star-like shape generally increases in size increasing the bias while in the inner part there is a flower-like shape feature. Disentangling all the possible features is a very arduous task. The band structure of the interface is complicated indeed and the bands descend both from the film and the substrate. Moreover not all scattering events are possible or detectable by the STS. A better understanding requires the use of some computational model.

5.2.2 The simulation procedure: the Joint Density of States

We compute joint density of states (JDOS) simulations for the system [148]. The procedure is the following: The main Fourier component of the LDOS is

$$g(E, \mathbf{q}) = \frac{1}{4\pi^2} \int_{E(k)=E(k')} \int f(\mathbf{k}, \mathbf{k}') \delta(\mathbf{q} - \mathbf{k} + \mathbf{k}') d^2\mathbf{k} d^2\mathbf{k}', \quad (5.1)$$

which is basically a delta function around the possible scattering vectors times a matrix element factor corresponding to the probability of the scattering event to occur and/or be detected ($f(\mathbf{k}, \mathbf{k}')$) [149]. First we map all possible scattering vectors for the system without taking into account the scattering probability. To do this one must know (or have an idea of) the constant energy contours of the material's electronic structure. The JDOS simulation approach consists in computing the self-correlation function of the band structure's 2D CEC in k -space at a given energy. This process, schematised in Fig. 5.5,

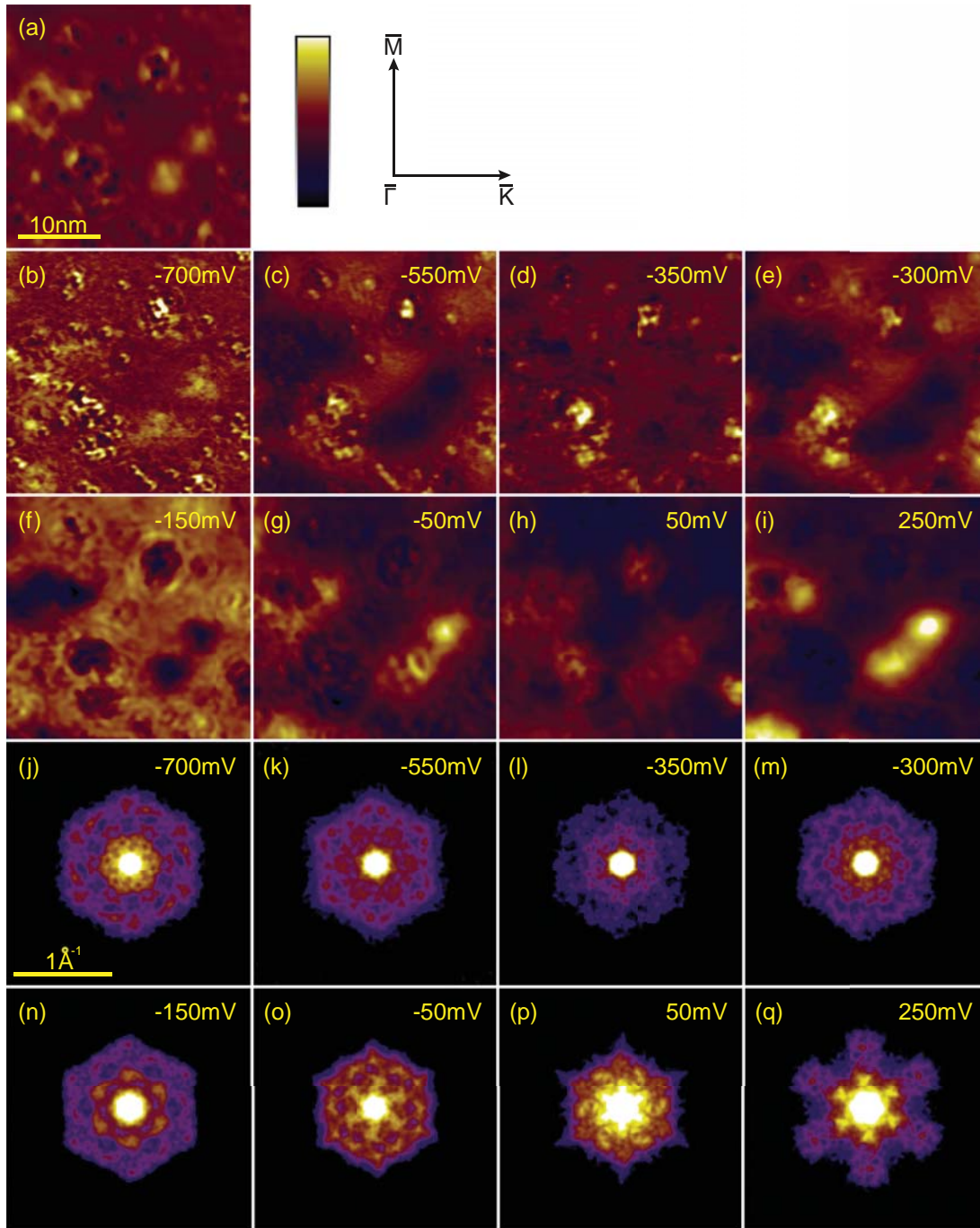


Figure 5.4: (a) Constant-current STM image of an area of the bismuth bilayer ($V=-50$ mV, $I=3$ nA; scale from 0 to 80 pm). The crystallographic directions are indicated. (b)–(i) STS images of the same sample area as in (a) measured at the indicated sample biases ($I=3$ nA). The colour range covers the following ranges of conductances: (b) 0.09 to 0.13 nS, (c) 0.09 to 0.17 nS, (d) 0.17 to 0.29 nS, (e) 0.23 to 0.4 nS, (f) 0.4 to 0.7 nS, (g) 1.2 to 2 nS, (h) 0.46 to 1.8 nS, (i) 0.23 to 0.79 nS. (j)–(q) FT-STIS images resulting from Fourier transformation of (b)–(i) and image processing as described in the text.

actually counts the number of all possible scattering vectors within the same CEC. The resulting number for a particular scattering vector is then plotted in a scattering vector space (q-space) in analogy with the FT of the standing waves. This approach has been successfully utilized to help the interpretation of QPI patterns, it was pioneered for the case of high temperature superconductors [150, 151] and more recently used in the field of topological insulators [152, 153].

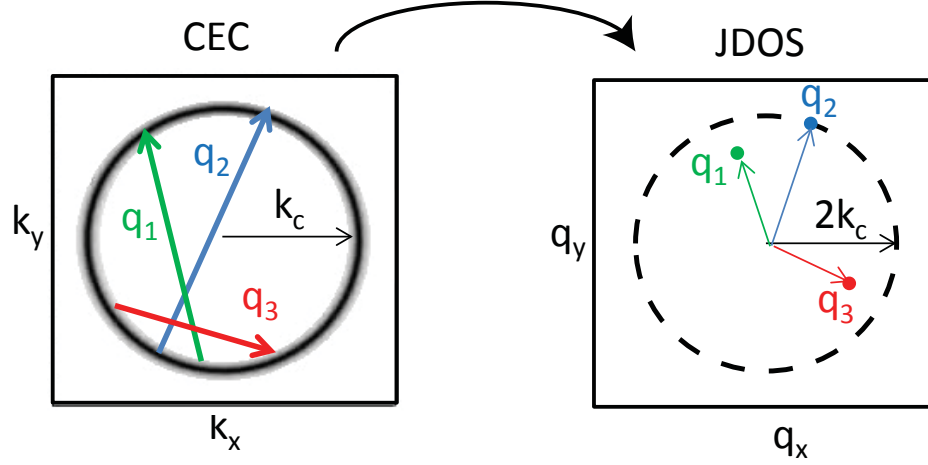


Figure 5.5: (a) Schematic representation of the joint density of state approach: all possible scattering vectors are counted and mapped into q-space.

In order to gain access to the shape of the CECs the FT-STs technique is usually used in symbiosis with ARPES. Displaying iso-energy images from ARPES datasets provides a direct observation of the CECs. The ARPES intensity, in its spectral function shape, is proportional to the density of states of the detected state. This means that it is possible to use the intensity of the spectral function signal $I(\mathbf{k}_{\parallel})$, proportional to the DOS(\mathbf{k}_{\parallel}) at a particular crystal momentum, to compute the joint density of states. The self correlation function is calculated from the spectral function intensity I as:

$$\int I(\mathbf{k}_{\parallel}) M(\mathbf{k}_{\parallel}, \mathbf{k}_{\parallel} + \mathbf{q}_{\parallel}) I(\mathbf{k}_{\parallel} + \mathbf{q}_{\parallel}) d\mathbf{k}_{\parallel}, \quad (5.2)$$

where I is the spectral intensity and M is a scattering matrix element.

Before describing the results of the simulations on the Bi bilayer, we spend few words on the computational details of the JDOS procedure and the main characteristic feature encountered. The code for calculating the JDOS has been written in the IGOR software environment [154]. Each CEC consists of a quadratic 150x150 grid of intensities. The intensity of the signal in the JDOS at the point \mathbf{q} is calculated as the sum of the intensities of all possible scattering vectors \mathbf{q} in the CEC grid as schematically represented in Fig. 5.5; each scattering vector intensity is calculated as the product of the intensities of the spectral function in the two points \mathbf{k} and \mathbf{k}' being $\mathbf{q}=\mathbf{k}'-\mathbf{k}$ times an eventual matrix element. This means that only the vectors connecting two points on the CEC actually contribute to the JDOS signal. The code is written in such a way that the different bands can be separated and the specific contributions of the JDOS features can be easily disentangled by computing specifically selective self and cross correlation between any couple of bands.

Moreover, in order to take into account the spin splitting of the bands, we construct spin matrix elements M . [152, 155] The matrix elements are created following standard Fermi's golden rule as overlap integral of the two spin states at \mathbf{k} and \mathbf{k}' . The spin states are represented by normalized spinors $\Psi_k = \frac{1}{\sqrt{2}}[1, \pm i \exp(i\theta_k)]$. As long as the scattering impurity does not carry a magnetic moment the impurity potential V can be brought out of the integral $\langle \mathbf{S}_{k'} | V | \mathbf{S}_k \rangle$ and the matrix elements are calculated as

$$M(q) = | \langle \mathbf{S}_{k'} | \mathbf{S}_k \rangle |^2 = \frac{1}{2}(1 \pm \cos \theta_q), \quad (5.3)$$

where θ_q is the angle between \mathbf{k}' and \mathbf{k} and \pm takes care of the identity of the two band branches. The spin factor depends on the angle between the directions of the spins in \mathbf{k} and \mathbf{k}' . With these spin considerations the scattering between two states of opposite spin polarization is forbidden and the respective signal in the JDOS with spin matrix elements (s-JDOS) is suppressed. By looking at the factor $1/2 (1 \pm \cos \theta_q)$ it turns out that not only the backscattering is suppressed but the intensity of the signal varies as the $\cos(\theta)$ and a certain degree of signal suppression is expected for a wider range of angles.

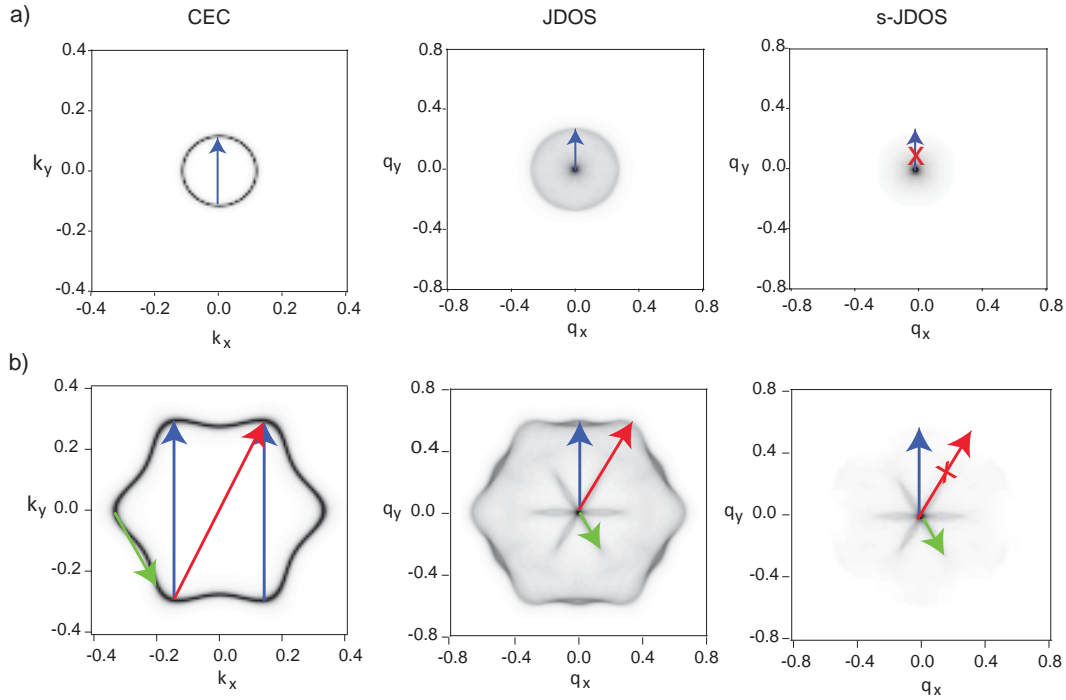


Figure 5.6: JDOS and s-JDOS examples for (a) a circular CEC and (b) for an hexagonally warped CEC. The main scattering vectors are represented by arrows, The s-JDOS are calculated assuming an in-plane helical spin texture, in this case the backscattering is suppressed.

Fig. 5.6 is a pedagogical representation of the results of JDOS and s-JDOS simulations for two examples of simple CECs: The circle and the warped hexagon with helical spin texture. Backscattering is suppressed in the s-JDOS.

It must be noted that the JDOS simulations are not an *ab initio* model and should not be used for fitting the experimental results but rather as a phenomenological platform

for comparison with the QPIs. In fact the JDOS shows all possible scattering vectors and provides information on their origin; the introduction of physical matrix elements, like the spin probabilities used here, are to be used to compare features that get suppressed or enhanced but do not provide a full description of the QPI intensity. On the other hand the JDOS are a very practical, simple, and somehow efficient approach for understanding the QPI patterns.

The CECs can be obtained by creating a model-spectral functions with arbitrary small broadening from the bare band energy dispersion obtained by fitting the ARPES signal, when possible. An other approach consists in calculating the constant energy surfaces by computing the material tight binding Hamiltonian, when this is known [156]. Given the complexity of the system here under study the tight binding approach would be a too simple model. We develop a semi-theoretical approach to model the complex band structure spectral function. This will provide us a rather precise model for the electronic structure and the possibility to study unoccupied states as well. The entire procedure that starts from the model spectral function creation to the computation of the JDOS is graphically represented in Fig. 5.7:

LDA slab calculations for the Bi bilayer/Bi₂Se₃ system around $\bar{\Gamma}$ are computed along three different directions in a 0.7 Å⁻¹ range in the surface Brillouin zone. We specifically chose the $\bar{\Gamma}-\bar{K}$, $\bar{\Gamma}-\bar{M}$ and $\bar{\Gamma}-\bar{B}$ directions where \bar{B} is defined as the point along the perimeter of the surface Brillouin Zone that sits at equal distance between \bar{K} and \bar{M} (Fig. 5.7(a)). The relevant eigenvalues $E(\mathbf{k})$ for each band have been isolated and symmetrized in \mathbf{k} -space according to the pseudo 6-fold symmetry of the system, which resulted in the description of the band structure along 12 different directions. We used a 3-dimensional interpolation of the data to obtain a full profile of the single electron bare energy. Note that this method does not require to fit the dispersion profile with any functions but uses a Voronoi natural neighbours interpolation of scattered data points [157]. Thanks to the interpolation procedure we can avoid using functions to model the bare energy dispersion; this would indeed be a hard task, and very un-precise given that the dispersion of these bands is far from being free-electron-like. In the end we create a full 3-dimensional spectral function in the energy range [-1.00,+0.65] eV using the interpolated dispersion data-points as bare-energy term $\epsilon(\mathbf{k})$ and by implementing a modified version of the spectral function Equation 2.8:

$$A(E, \mathbf{k}) = \frac{|\Sigma''(E, \mathbf{k})|}{[E - \epsilon(\mathbf{k}) - \Sigma'(E, \mathbf{k})]^2 + \Sigma''(E, \mathbf{k})^2} * W(E, \mathbf{k}), \quad (5.4)$$

where E is the electron energy, Σ' and Σ'' are real and imaginary part of the electron self-energy here arbitrarily set to 0 and 0.001 eV. We introduce a localization weight term $W(E, \mathbf{k})$ as a weighting factor of the spectral intensity. This term is proportional to the wave function localization of each state $|E, \mathbf{k}\rangle$ on the Bi-bilayer surface. The W factor is computed through all the 3D grid with the same symmetrisation-interpolation procedure used for $\epsilon(\mathbf{k})$ starting from values associated to the individual points of the DFT calculations. Fig. 5.7(b) displays a three-dimensional prospect of the model-spectral function. The intensity for different bands changes with the localization wave factor. Thanks to this trick we take care of the surface sensitivity of the STS technique and in the same time it sets to zero all the bands that result from the slab calculation which have low contribution on the bilayer surface and will be unlikely to contribute to the QPI pattern. The spectral function is cut at different binding energies above and below the Fermi level to obtain the constant energy contours as shown in Fig. 5.7(c). A good match is found in the comparison with

the ARPES CECs for the occupied states. Once isolated the constant energy contours, we

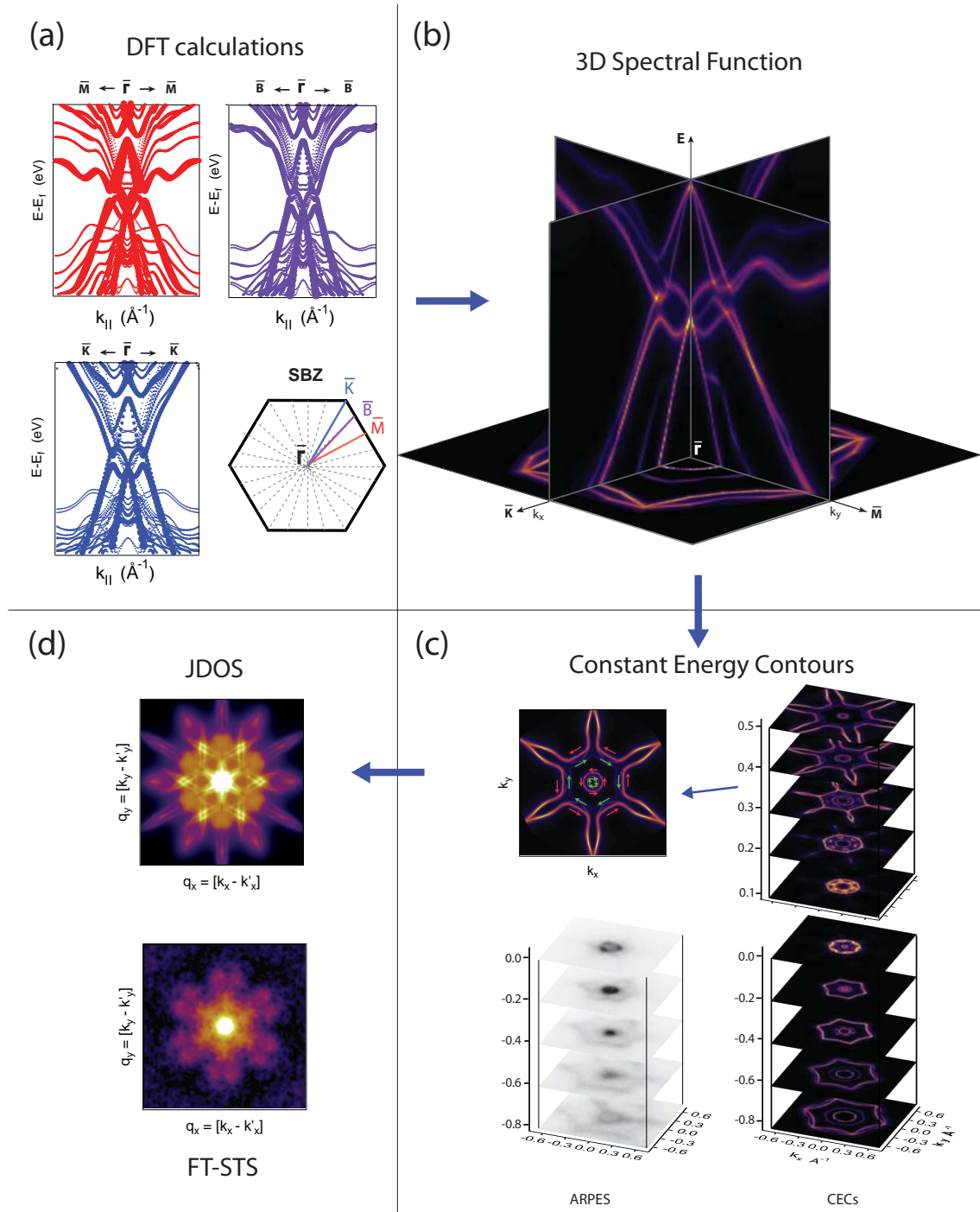


Figure 5.7: Spectral function modelling and JDOS simulation: (a) DFT calculations along three high symmetry directions in the surface Brillouin Zone ($\bar{\Gamma}$ - \bar{M} , $\bar{\Gamma}$ - \bar{K} and $\bar{\Gamma}$ - \bar{B}). (b) three dimensional spectral function modelled by 3D- interpolation of the DFT calculations. (c) Constant energy cuts through the spectral function and comparison with ARPES for occupied states. (d) comparison between QPI and JDOS.

perform as final step the JDOS simulation as described in Eq. 5.2 (Fig. 5.7(d)).

The spin texture of the system is simplified as follow: We assign to the interface Dirac cone the typical chiral spin texture of the topological states [145]. We approximate the spin texture of the Bi₂Se₃ interface conduction band and of the Bi bilayer upper valence band (both spin split) with a Rashba-like in-plane spin polarization

Spin directions in an example constant energy contour are represented in Fig. 5.7(c). For most of the energies introducing the spin matrix elements do not results in a clear suppression of some feature because the bands are often close to degeneracy, nevertheless s-JDOS results in an improvement of the relative intensities (more similar to experimental data) respect to normal JDOS. To quantify the effect of the spin polarization on the JDOS we compute the cross correlation between experimental data and JDOS/s-JDOS. We obtain 71% in the case of JDOS and 80% in the case of s-JDOS.

5.2.3 QPI vs JDOS

We analyse now the results obtained and the comparison with the experiments. We focus on five energies that are representative of the overall electronic structure. Fig. 5.8 shows a direct comparison at -0.80 eV, -0.35 eV, -0.15 eV, +0.25 eV and +0.35 eV: on the top row the CECs are shown, in the middle row the s-JDOS resulting from the CECs are displayed, at the bottom row the experimental QPI are reported. The main scattering vectors are displayed by arrows on the CECs, to each vector correspond interference features highlighted by small features of the same colour in the s-JDOS and QPIs.

We find an overall good agreement in the shapes and features: Below the Fermi level the hexagonal shape comes from a warped hexagon CEC, by approaching the Fermi level the hexagon becomes smaller. For the unoccupied states the overall shape is star-like with 6-fold branches along $\bar{\Gamma}-\bar{M}$.

We explore the features more into detail following the schematics of the figure. For the energies -0.8 eV and -0.35 eV the CEC is a double hexagon (Bi VB) and a circle (interface Dirac cone) inside. The following scattering signatures are found, referred to their colour in the figure:

Green - Bilayer valence band (intraband): This is the backscattering within the hexagonal contour, since the two VB are spin polarized the actual backscattering is suppressed; nevertheless the two VBs are almost degenerate in a long energy range in the calculations and therefore the backscattering direction still provides strong intensity. The intraband scattering creates the outer hexagonal contour in the s-JDOS. This outer feature is present in the QPI at -0.35 eV but it is absent at lower energies, i.e. at -0.8 eV. The absence of these feature at low energy can be due to two factors: no intraband scattering happen at -0.8 eV or the sensitivity of the technique for large k-values becomes too low to detect such short wavelengths. By switching off this channel in the simulations a very good agreement with the QPI is found (not shown) The dark green vector represents scattering alongside of the hexagon. This gives rise to six sharp features starting from the centre in the JDOS and it appears in some QPI as six high intensity dots

Orange/Red - Bilayer/Dirac cone (interband): An interband scattering event that occurs between the outer hexagon (Bi VB) and the inner circle (DC). From a purely geometrical point of view, the self-correlation of a CEC composed by a concentric hexagon and a circle gives rise to a bulky hexagonal shape hollow in the centre. The two extrema of this hexagonal crown are the forward (red vector) and backscattering (green vector) between

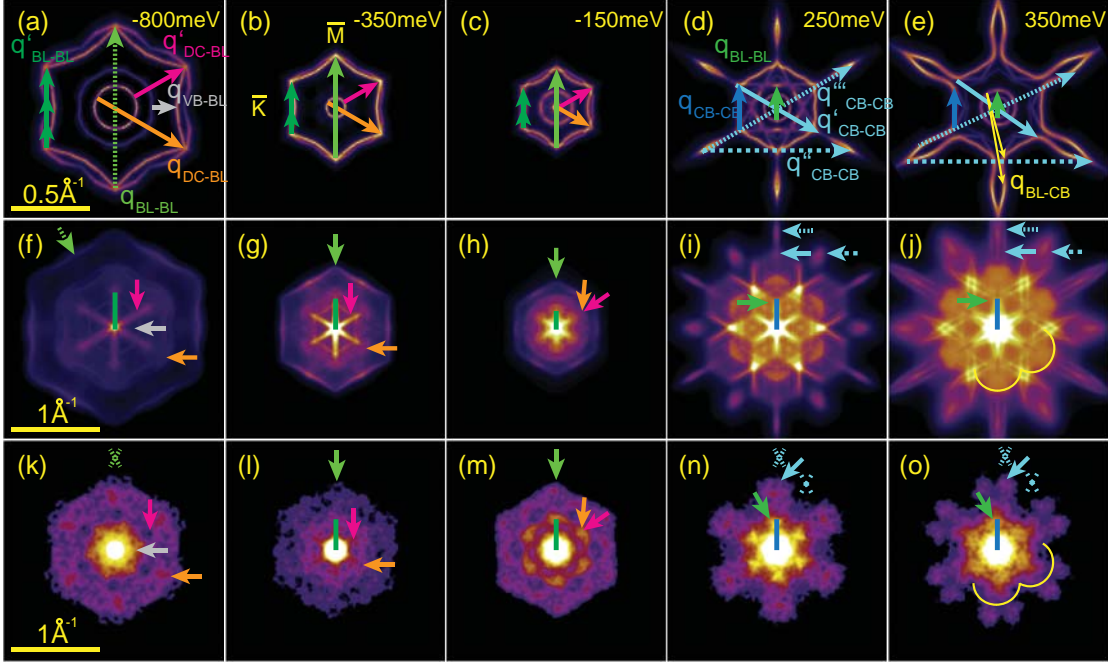


Figure 5.8: Comparison between calculated CECs (a)–(e), resultant JDOS (f)–(j), and measured FT-STs (k)–(o) at the indicated energies. The arrows in the CECs represent scattering vectors \mathbf{q} , and the arrows or crosses of the same colour indicate the resulting features present or absent, respectively, in the JDOS or FT-STs images.

the two geometrical objects. This is exactly what appears in the QPI and the s-JDOS. In particular at -0.8 eV the QPI, the hexagonal crown is well discernible as simulated by the s-JDOS.

For the CEC at -0.15 eV the Dirac cone is close to the Dirac point. Qualitatively there is a good match between the JDOS and the QPI but the radius of the outer feature in the QPI is quite larger than for the simulation. It appears that the DFT calculation fails in quantitatively predict the correct dispersion around the Fermi level where the hybridization between the bismuth and the Bi₂Se₃ bands occurs. This can be caused by the approximation in the LDA-slab framework but it can also be due to a slightly stronger or weaker interaction with the substrate with respect to what it is computed. The presence of the conduction band in this region is not easily detectable yet because of the low spectral weight and the too small interband scattering vector. A clear signature of the role played by the interface Bi₂Se₃ conduction band appears right above the Fermi level.

As last step we look at the scattering channels in the region above the Fermi level. In this region we have clear evidence of the opening of a new scattering channel, the Bi₂Se₃ conduction band at the interface. Right above the Fermi level the bismuth band penetrates and hybridizes with the Bi₂Se₃ band so that the latter becomes the most external contour. More in details we analyse the contours at 0.25 eV and 0.35 eV. The CECs consists of an hexagonal snowflake that stems from the CB and two almost circular contours from the bilayer VB. The warping on the VB is here small close to the maximum of the band. The s-JDOS presents many features that are not present in the QPI but it also reproduces the

main features.

We can identify 2 main features: Blue - CB scattering (intraband): the blue vectors represents the intraband scatterings in the CB. The corresponding features in the QPI (and JDOS) are the outer branches that appear along the $\bar{\Gamma}\bar{M}$ direction. The dark blue is used for the scattering along the side of the snow-flake shape, giving rise to the small features around the centre. Yellow - Bilayer/CB (interband): This interband scattering gives rise to a bulky flower shape, characteristic for the scattering between the snowflake CEC of the CB and a circular CEC. This feature proves the coexistence of the two bands in the unoccupied states region. The electrons at the interface scatter from the Bi_2Se_3 state to the Bi bands.

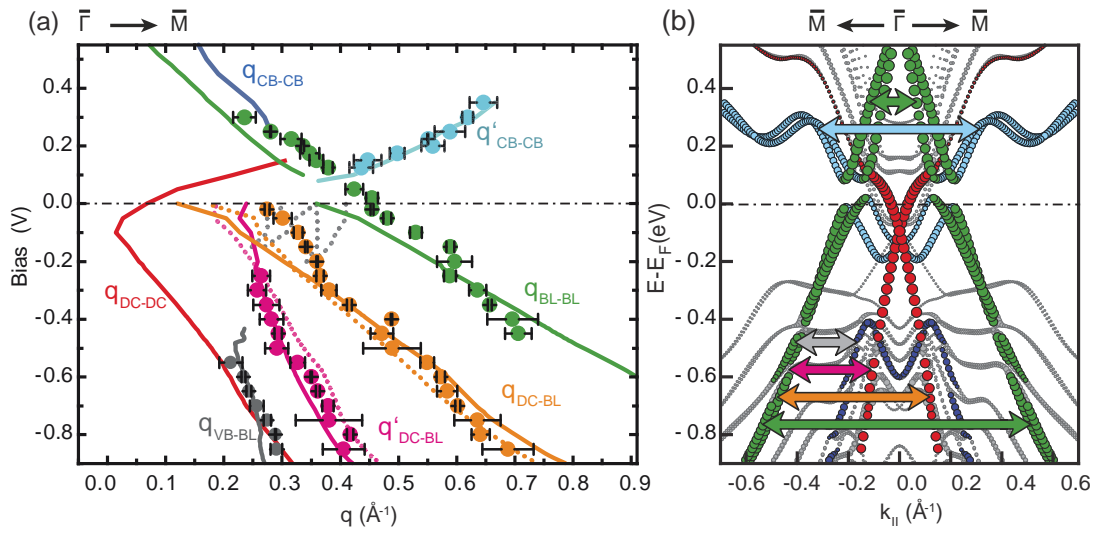


Figure 5.9: Comparison of the dispersion of the scattering vectors from FT-STs (dots) and JDOS simulation (lines) along $\bar{\Gamma}\bar{M}$ corresponding to the following \mathbf{q} as indicated: Bi bilayer intraband scattering (green), Bi_2Se_3 CB intraband scattering (light blue), interband scattering between Bi bilayer and Bi_2Se_3 VB (grey), and between Bi BL and DC (pink and orange). The dotted pink and orange lines are the corresponding interband scattering channels of the DC into the second branch of the Bi bilayer band of equal spin helicity, which are forbidden by spin conservation. Dark blue line, scattering alongside the hexagonal part of the Bi bilayer CEC; grey dotted lines, Bi_2Se_3 CB intraband scattering vectors. The red line indicates the dispersion of the DC intraband scattering which is not observed (b) DFT-calculated band structure including the observed scattering vectors \mathbf{q} as arrows with the same colours as the corresponding dispersions in (a).

By analysing the scattering vectors in a long range of energy below the Fermi level, we can track back the electronic structure of the system and compare it with the structure we used for the simulations. In Fig. 5.9(a) the scattering vectors' lengths obtained from the QPI features along $\bar{\Gamma}\bar{M}$ are plotted against the electron energy. Symbols are the experimental features and lines derive from the simulations (dotted lines from the homologous spin split bands). In Fig. 5.9(b) the main backscattering vectors are displayed on the calculated band structure to help the reading. We notice a remarkable agreement of the simulations with the experiments. The VB intraband scattering is displayed in green. A good agreement in the dispersion is found but it diverges above -0.2 eV as previously discussed. Any signature of the VB intraband backscattering disappears below -0.5 eV. The interband scattering channels represented in dark red and orange carry useful information:

first of all we obtain convincing signature that the Dirac cone state is present for a wide energy range at the interface between the bilayer and the substrate. Being an interface state that mainly comes from the 2-dimensional bismuth film, the state does not need to merge into the bulk bands as it is common for the 2D topological states in three dimensional systems, hence it can be quite extended. The state has a linear dispersion as predicted by the DFT calculations. While the state is protected from intraband backscattering, we obtain here direct proof that the state is not protected from interband scattering. A clear signature of interband scattering with the bilayer bands persist in the QPIs along all the investigated energy range. Note that, according to the calculation, no absolute gap is opened around the Fermi level in the Bi and Bi₂Se₃ bands, which would make the Dirac cone accessible. Nevertheless one could think of opening the hybridization gap by, for example, increasing the interaction with the substrate. Above the Fermi level the channels involving the conduction bands are opened. The grey symbols, below -0.4 eV, represent dispersing features detected in the QPI. Arguably these features, from the dispersion and size, could be attributed to intraband scattering in the Dirac cone. However this is more likely due to scattering events between the bismuth valence bands and the Bi₂Se₃ valence bands, since the feature disappears above the top energy of the Bi₂Se₃ VB.

We note that the presence of the bilayer VB so high in energy does not only demonstrate the strong doping due to the charge transfer effect but it also has very important consequences from an application's point of view. We have argued that the bilayer film can be grown on top of Bi₂Se₃ without losing the topological properties, this allows the existence of helical dissipationless states on the edges. But we need to consider that the topological edge states can only be found within the bilayer gap. The gap is obviously located right above the upper valence band. In order to be able to access the edge states the gap, and therefore the valence band, must be brought down to the Fermi level. The QPI demonstrates the existence of the VB up to 0.3 eV above the Fermi level and, according to the calculation, the valence band maximum is located above 0.6 eV. Even if the existence of the edge states for such a system was proven it will not be possible to directly exploit them. The most obvious solution would be to decouple the film from the substrate. Unfortunately it is still not clear how this can be accomplished. Another solution would be to selectively populate the bilayer states with local doping with surface adatoms.

We can summarize the main achievement obtained by the combined analysis of FT-STs and s-JDOS simulation: We confirmed for most regions the electronic structure predicted by DFT. We found the signature of the existence of an extended Dirac cone-like topological state created at the interface between the Bi bilayer and the Bi₂Se₃. Even if the intraband scattering is forbidden interband scattering occurs from the Dirac state. For most of the energy range investigated, we observe co-presence of intraband and interband scattering. The bilayer gap in this system is located higher than 0.4 eV above the Fermi level because of the charge transfer from the film to the substrate.

5.3 Conclusions

We have studied the electronic structure at the interface between a single Bi bilayer (111) and the surface of Bi₂Se₃ (111). The Bi bilayer is a 2D topological insulator and Bi₂Se₃ is a 3D topological insulator. We have grown the bismuth film by MBE in vacuum on a cleaved substrate surface. The bilayer grows coherently on the substrate with small in-

plane squeezing of the unit cell to accommodate on the Bi_2Se_3 . The electronic structure has been studied by ARPES, DFT calculations and FT-STs. The ARPES data show the presence of two new states created by the presence of the bilayer: the Bi upper valence band and a new Dirac-cone like state. The FT-STs show a complicated pattern of possible scattering vectors. In order to fully understand the experimental results we perform joint density of states simulations taking into account the spin texture of the system starting from three-dimensional spectral functions modelled on the DFT calculations. We find a remarkable good agreement between the simulations and the FT-STs. Thanks to the JDOS simulations, we can assign a physical meaning to each FT-STs feature. Our results confirm the presence of an extended Dirac state around $\bar{\Gamma}$. This band is generated by the coupling of the two surfaces in a strong spin-orbit coupling regime. The interaction between the bilayer and the substrate hybridizes the Bi bands and gives rise to the new chiral state. The overall topology of the system is maintained. FT-STs analysis confirms the linear dispersion of the Dirac cone and demonstrates the existence of Coulomb-impurity driven interband scattering between the Dirac cone and the bismuth valence bands. By interfacing the two materials, a charge transfer from the film to the substrate occurs causing the bilayer gap to lie several hundred meV above the Fermi level. At the interface a local electric field stimulates the creation of 2DEG-like quantum well state with high surface localization. Inter-band scattering between bilayer and Bi_2Se_3 bands is allowed and demonstrated.

The use of s-JDOS simulations modelled on DFT calculations has proven to be most useful to obtain information about electronic structure and scattering channel, for both occupied and unoccupied states. This new approach, based on the creation of a 3D spectral function, from DFT calculations, that can be easily manipulated, revealed to be a powerful tool of analysis with potential for future applications of the kind.

In terms of possible electronic application, this study shows that the Bi bilayer can be grown on Bi_2Se_3 . Unfortunately the hybridization causes the bilayer gap to be inaccessible for transport and the Fermi level must be tuned to be in the midgap if the 1D edge states should be exploited.

Chapter 6

Electronic structure of rare earth diantimonides: LaSb_2 and NdSb_2

6.1 An overview

Light rare earth (r.e.) diantimonides share the same SmSb_2 -type crystal structure. After being overlooked by the scientific community for several decades, the work of Bud'ko *et al.* in 1998 on the magnetoresistive properties of diantimonides, produced a renovated interest in these materials [7]. Bud'ko *et al.* measured several transport and magnetic properties of light r.e. diantimonides LaSb_2 , CeSb_2 , PrSb_2 , SmSb_2 and NdSb_2 . Many diverse physical properties were found, with particular remark on the magnetoresistance and magnetic phases at low temperature. In particular for LaSb_2 , NdSb_2 and PrSb_2 an anisotropic linear and non-saturating magnetoresistance was found. While all the other compounds presented several magnetic phases, LaSb_2 is the only one which is diamagnetic at all temperature. The absence of magnetic phases strongly simplifies the study of this material, specially for low temperature measurements, making it preferable to the others as sandbox to investigate physical properties.

LaSb_2 crystallizes in orthorhombic structure with space group Cmca [158]. The crystal structure is sketched in Fig. 6.1(a). The lattice is layered, with planes perpendicular to the [001] axes. Two Sb-terminated quintuple layers fit in one unit cell. Within the quintuple layers two LaSb sheets are separated by a planar sheet of Sb atoms. The size of the unit cell parameters along [100] and [010] is quite similar, while along [001] it is three times higher (details in the Section 6.3). Given this crystal structure, strong anisotropy in the physical properties is expected. In the work of Bud'ko *et al.* LaSb_2 was found to have almost isotropic linear magnetic susceptibility, linear in-plane resistivity with metallic behaviour and linear magnetoresistance. Curiously the application of a magnetic field produces a singularity in the ρ/T curve, whose origin is still unknown and subject to debate [7]. The most surprising behaviour is the linear magnetoresistance which does not saturate to high fields. These results were later reproduced and confirmed by Young and DiTusa who show the magnetoresistance does not saturate up to 45 T [160, 161]. Fig. 6.1(b) shows the transverse magnetoresistance behaviour for currents in the a-b plane with magnetic field parallel and perpendicular to the a-b plane. The resistance increases up to 90 times in the parallel geometry but it is one order of magnitude lower for the perpendicular measurement. Values of magnetoresistance are also significantly higher than for silver

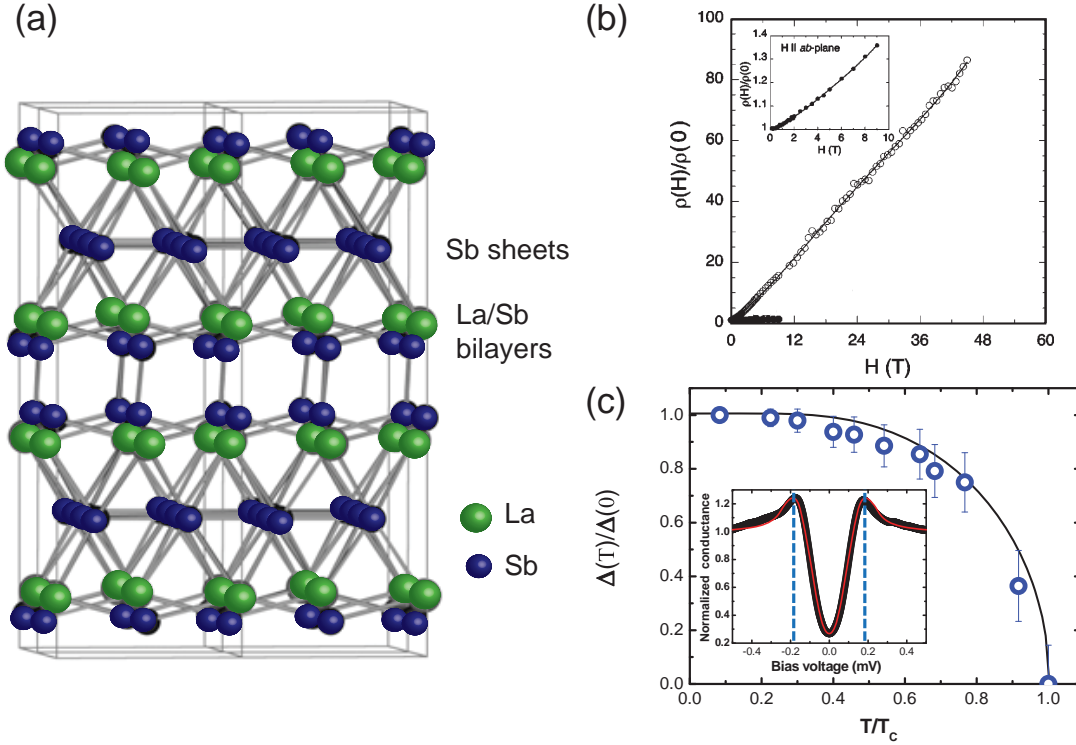


Figure 6.1: (a) Orthorhombic structure of LaSb_2 , belonging to the space group Cmca . The crystal possesses a highly layered structure with planar Sb sheets and Sb-terminated quintuple layers. Adapted from Ref. [159]. (b) Transverse magnetoresistance of LaSb_2 at $T=2$ K with the current in the ab plane and magnetic Field oriented parallel (closed circles) and perpendicular (open circles) to the ab plane. Inset: Low field magnetoresistance with $H \parallel ab$ plane. Adapted from Ref. [160]. (c) Temperature dependence of the position of the quasiparticle peak in the density of states. The black solid line is the temperature dependence of the superconducting gap in BCS theory. Inset shows the tunnelling conductance curve at $T = 0.15$ K. After Ref. [8].

chalcogenides compounds, largely studied as promising magnetic sensors materials [162]. The strong anisotropy and the large linear magnetoresistance has put LaSb_2 under the spotlight for directional magnetic sensor material [160].

The semi-classical description of the magnetoresistance predicts the resistance to be saturating, for close orbits, or to be varying quadratically with the magnetic field for open orbits. The co-presence of linear behaviour and non-saturation is therefore unusual. Many theories on linear magnetoresistance have been discussed for these materials. A comprehensive review of all the possible factors inducing such behaviour was given by Bud'ko *et al.* but none of these was conclusive [7]. Among the most accredited and discussed theories are the quantum linear magnetoresistance and the possible presence of charge density wave (CDW) order. The former was brought forward by Abrikosov in 2003 [44]. The quantum theory can account for the reported behaviour but it requires the presence very small carrier densities and effective masses and possibly a Dirac cone-like dispersion close to the Fermi level. In the effort to explain the linear magnetoresistance of rare earth diantimonides, knowing that the electron density is "non-small", but without knowledge of the electronic

structure, Abrikosov postulates that the secret for linear magnetoresistance lies in the presence of small linearly dispersing pockets in the energy spectrum coupled with interband transitions [44].

The hypothesis of charge density waves and magnetic field induced CDWs have also attracted a lot of attention. The CDW is a periodic modulation of the electron wave function in one or two dimensions, typically accompanied by a lattice distortion of the same wavelength, and it drives the metal in an insulating state. Linear magnetoresistance can be ascribed to this [163]. The strong two-dimensionality of this layered materials and the possible presence of strong nesting vectors at the Fermi surface in LaSb₂ seem like a fertile ground for CDW presence. Prototypical materials for CDW, TaSe₂ and NbSe₂, present a similar crystal structure [164]. The presence of CDW in LaSb₂ was investigated and discussed by different authors [8, 159, 161, 165]. Contrasting findings do not provide a convincing prove for either case but most recent results through optical conductivity seem to more strongly rule-out the CDW presence. The cause of the linear magnetoresistance is still unknown.

More recently LaSb₂ has been found to have superconductive properties, with critical temperature typically below 1.2 K [8, 166]. Superconductivity was found to be anisotropic, with anisotropic Meissner effect and potentially two-dimensional, because of the weak coupling between layers in the c-direction. The superconducting gap as measured by low temperature STM and its temperature dependence are represented in Fig. 6.1 (c) [8] and represent the behaviour of a type I superconductor. A wide superconducting transition was found, compatible with a multi-band model of superconductivity.

All the above presented knowledge is often more conjectural than factual. No definite explanation for the magnetoresistance, nor a good theoretical model for the superconductivity is known. This un-decisiveness is arguably attributable the lack of knowledge of the complete electronic structure of the material. Timid attempts in the experimental investigation of the electronic structure were done employing transport measurements and de Haas-Van Alphen oscillation. Goodrich *et al.* found the existence of three Fermi surfaces, two of them with two dimensional character and one, small, with three dimensional dispersion. The comparison with DFT calculations of the Fermi surface gave good agreement with the experimental results in placing the three bands but also revealed the presence of a large portion of the Fermi surface which is not detected by the de Haas-Van Alphen measurements [165]. Previous photoemission results by Acatrinei *et al.* are used to identify spectral features down to several eV below the Fermi level, assigning their orbital origin, but it fails in describing a dispersion relation of the low energy band structure [159]. Further information was obtained by transport experiments which revealed for LaSb₂ medium-low carrier density at the Fermi level ($3.0 \cdot 10^{20} \text{ cm}^{-3}$) [160] and small effective masses ($m^* = 0.20 m_e$) [165]. Hall measurements revealed moreover signatures of co-presence of opposite carriers at low magnetic field values and hole-like behaviour for High magnetic fields [160].

It is clear that to fully understand the promising physical properties of LaSb₂, a clear picture of the electronic structure needs to be formed. The amount of work done on this material is actually quite small and it seems to have never caught the attention of the solid state community despite the very promising premises.

In the attempt o fill a gap in the knowledge of the electronic properties of rare-earth diantimonides we employ in this work angle resolved photoemission spectroscopy coupled with DFT calculations on LaSb₂ to describe the electronic structure of this material. First we will describe the experimental challenges of such an experiment, then we will present and

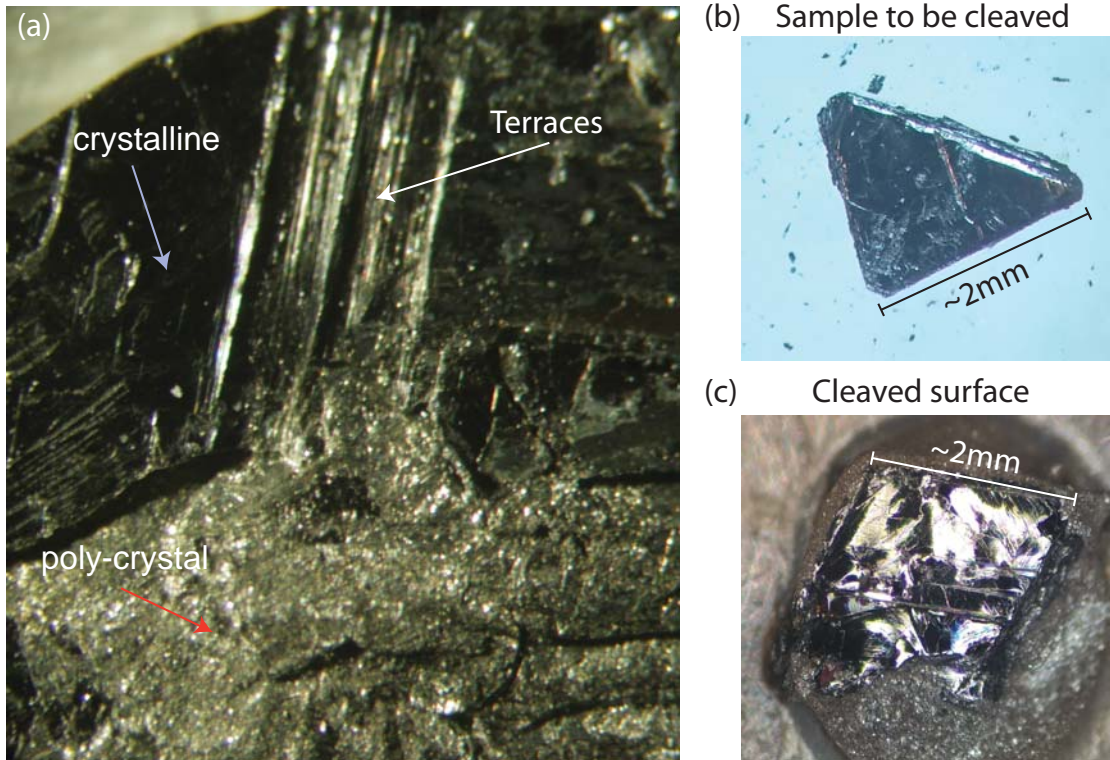


Figure 6.2: Optical microscope images of LaSb_2 samples. (a) Part of a big piece of crystal as coming from the synthesis process, terraces of larger crystallites are alterned with polycrystalline portions. (b) Sample prepared for cleaving, the edges are cut along dislocation lines visible on the surface. (c) Example of surface after cleaving, used for ARPES measurements.

discuss the results on LaSb_2 . In the end the results for NdSb_2 are shown for comparison. LaSb_2 and NdSb_2 samples are grown by Karl Frederik Faerch Fischer at the Iversen lab in the chemistry department at Aarhus University. DFT calculations are performed by Ganapathy Vaitheeswaran at Hyderabad University and with the contribution of Axel Svane from Aarhus University. ARPES and analysis have been performed by the author.

6.2 Synthesis and experimental challenges

LaSb_2 single crystals were synthesized with self-flux method. Lanthanum is cleaned from oxides with an arc melter in argon atmosphere. The self-flux syntheses were carried out in Al_2O_3 crucibles in vacuum-sealed quartz ampoules with a static vacuum of 10^{-4} mbar to prevent oxidation. The two pure elements were mixed in ratio 1:9 lanthanum to antimony. The compound is brought to 1323 K in ten hours. The compound is maintained at that temperature for five hours and successively cooled very slowly ($1^\circ/\text{hour}$) to 913 K and later brought to room temperature. The crystals are then separated from the flux by centrifugation [167]. X-ray diffraction confirms the orthorhombic SmSb_2 structure. From structure refinement we find the lattice parameters $a = 6.321685 \text{ \AA}$, $b = 6.198740 \text{ \AA}$, $c = 18.533371 \text{ \AA}$.

The utilization of the LaSb₂ for ARPES experiments has revealed diverse experimental challenges, mostly connected with the quality of the surface. Since the amount of studies on the surface of these materials is very little, possibly also because of the difficulties in the preparation, we think it is worth to spend few words on the experimental procedure for the surface preparation. The synthesis yields crystals of various sizes. Part of a big crystal is shown in Fig. 6.2(a). Crystal pieces usually have polycrystalline phases and some single-crystal-like surfaces. The crystalline portions present several millimetric terraces visible at bare eye or optical microscope, revealing the layered nature. Micrometric dislocations and domain boundaries, are visible on the flat surfaces. We presume the flat surfaces expose the ab planes, given the layered structure. The standard procedure for surface preparation in layered materials is cleaving. We find that, despite the strongly layered structure, the crystal is quite resistant to the cleavage. This is probably due to both strong interlayer bonds and a high density of defects and dislocations in the crystal. Given the stiffness of the material the cleavage with scotch-tape technique is impracticable. In vacuum cleaving using top-post technique and using a blade to cut pre-prepared samples were attempted. In our experience the best results were obtained with cold top-post technique in accurately prepared samples. The operation is the following: the crystal was examined under optical microscope. It was then properly cut with a surgical blade along the visible dislocation lines so that only one apparent domain, at the surface, was isolated. Rectangular and triangular crystallites about 1-3 mm of dimensions with optically flat and homogeneous surfaces were obtained. The edges must be cut straight and, at times, indented to help the cleavage in a preferential plane (see Fig. 6.2(b)). The post is glued on the surface and the sample is transferred in the measurement chamber. The cleavage is performed in vacuum (high 10^{-11}) at around 100 K. Inspection of the sample surface after the measurements usually reveal a scattered, non-uniform surface with crystallites of different heights. This imprecision must be attributed to the inhomogeneity of the crystallites below the surface, despite the very careful preparation. Because of the stiffness of the material the cleavage removes thick portions of samples. The samples are usually not re-usable after one cleave (see Fig. 6.2(c)). It is unknown whether the sample cleaves preferentially at lanthanum or antimony planes. STM studies have shown surface attributable to both terminations [8]. For cleaves yielding good ARPES quality photoemission, a strong time effect at the surface was found. The ARPES image becomes broad and background increases consistently in less than one minute, making impossible to measure at the best conditions. After few hours the sample surface is inadequate for ARPES experiments. We believe this time effect is due to the strong reactivity at the surface, typical of lanthanum compounds. The rest gas reacts at the surface despite the fact that the cleaved sample only “experiences” a pressure lower than 10^{-10} mbar. Whether this ageing effect is catalysed by the radiation used for photoemission is still unclear.

6.3 The electronic structure

ARPES have been acquired at the SGM3 beamline at ASTRID2 at around 80 K. All the figures shown are acquired with photon energy of 70 eV. All calculations are performed by using the Full-potential linear augmented plane wave method as implemented in wien2k code [168], with the experimental lattice parameters and optimized atomic positions. We have used the 30000 k-points, with 3906 k-points in the irreducible Brillouin zone for both

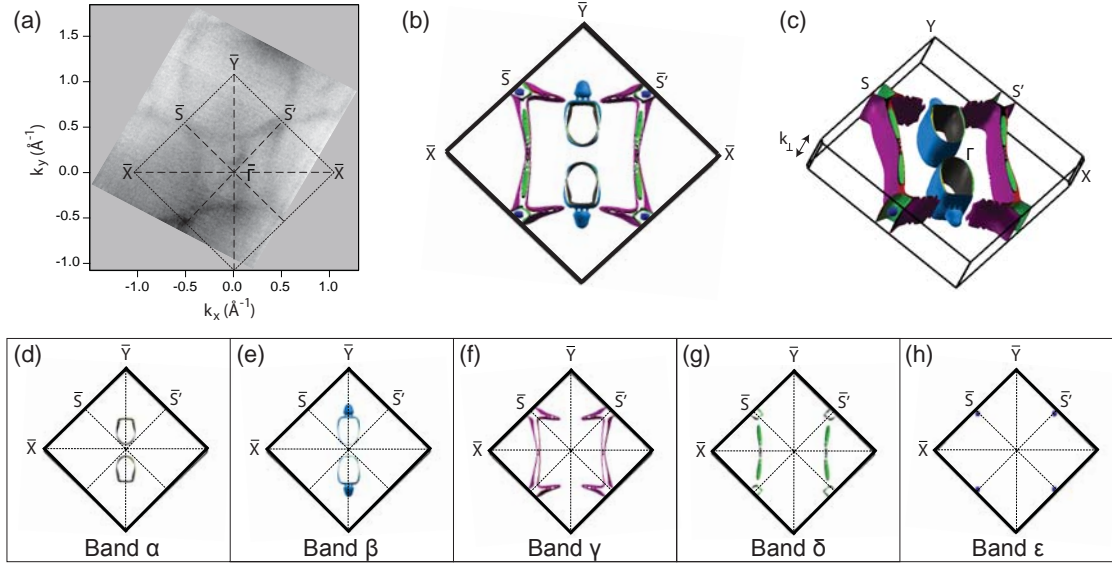


Figure 6.3: (a) Fermi surface of LaSb_2 (001) as obtained by ARPES. The first surface Brillouin zone is sketched on top. Letters refer to the high symmetry points in the surface Brillouin zone. (b,c) Fermi surface of LaSb_2 calculated by DFT: projection of the Fermi surface on the 2-D surface plane (b), and 3D plot in the bulk Brillouin zone where \mathbf{k}_\perp is the direction perpendicular to the \mathbf{k}_x - \mathbf{k}_y plane (c). (d-h) Projections on the \mathbf{k}_x - \mathbf{k}_y plane of the Fermi surfaces originated from the five bands α (d), β (e), γ (f), δ (g), ϵ (h) as labelled in the figure.

band structure and Fermi surface calculations.

6.3.1 The Fermi surface

Fig. 6.3(a-c) shows experimental and calculated Fermi surface of LaSb_2 . The surface, as obtained by ARPES, has a distinctive 2-fold symmetry. The first surface Brillouin zone is sketched on top of the image. The surface Brillouin zone has rhomboidal shape. Because of the similar value of the a and b lattice parameters the rhombus angles are 88.8 and 91.2, making it close to a square shape. It must not be forgotten, though, that the surface only has 2-fold symmetry and not 4-fold. Two mirror planes are projected on the surface in the $\bar{\Gamma}\bar{Y}$ and $\bar{\Gamma}\bar{X}$ directions. \bar{S} and \bar{S}' points are defined as shown in the figure. From the experimental data (Fig. 6.3(a)) we can identify two major parts of the Fermi surface: A surface with the shape of a warped square extends to the edges of the Brillouin zone. The corners of the square are at the \bar{S} and \bar{S}' points where they connect to the squares of the next Brillouin zones. The bands giving origin to these states disperse almost in one dimension (k_x or k_y). The deviation from the one dimensionality is due the slight quadratic warping. Inside the squared contour we can identify two oval pockets along the $\bar{\Gamma}\bar{Y}$ direction.

The calculated total Fermi surface is shown in Fig. 6.3(b,c) as a projection on the \mathbf{k}_x - \mathbf{k}_y plane (panel (b)) and as a 3D plot (panel (c)). A good agreement is found between ARPES and DFT, that shows the same features. The calculations reveal the presence of five bands that give rise to the Fermi surface. These are mapped separately in Fig. 6.3(d-h) and are

labelled according to the figure. The inner ovals come from band α and β . These bands were recognized in some previous work by de Haas-Van Alphen measurements (labelled α and β in Ref. [165]). According to the calculated band structure the outer square contour is also originating from two bands, labelled γ and δ . For both these bands the Fermi contour is actually double, meaning that it is not generated by a unique pocket at the Fermi level, but rather by 2 small directional pockets. The actual dispersion of these states will be discussed later in the text. The quality and resolution of the ARPES Fermi surface does not allow to recognise the double line contour. The band ϵ gives rise to small pockets at the \bar{S} and \bar{S}' points.

It is of great importance to look at the \mathbf{k}_\perp dispersion of the Fermi surfaces (panel (c) shows the \mathbf{k}_\perp dispersion of the Fermi surface, this can also be visualized in the projected surfaces inspecting the thickness of the contours). The surface of LaSb₂ is characterized by an almost exclusively two dimensional dispersion. Bands α, γ, δ have zero or little \mathbf{k}_\perp dispersion leading to open orbits along the c direction in real space. Moreover γ and δ have open orbits also in the ab plane, thus leading to the lack of signature in de Haas-Van Alphen measurements [165]. The band β also has open Fermi surface but, from our calculations, it shows two small \mathbf{k}_\perp dispersing pockets. The small features deriving from band ϵ are the only ones expressing close orbits in all directions. One way to prove this with ARPES is to obtain photoemission maps at different photon energies. Unfortunately the photoemission experiment on this material is a hard task and a relevant energy-scan could not be acquired, also due to the fact that only few photon energies yielded high enough photoemission intensity. Fermi surface maps at few different photon energies have been acquired and no relevant change in the Fermi surface was found (not shown).

6.3.2 The band dispersion

To understand the nature of the Fermi surface we look at the dispersion in energy of the band structure. DFT band structure calculations are shown in Fig. 6.4(a) along high symmetry lines. Symmetry points in the bulk Brillouin zone are identified in Fig. 6.4(b). The bands crossing the Fermi level are drawn in different colours and labelled as in the figure. The bands $\alpha-\epsilon$ give rise to the respective Fermi surfaces $\alpha-\epsilon$ of Fig. 6.3. Wide s-p bands disperse down to 4.7 eV in binding energy. These bands are hybridizing with several more localized bands resulting in the band dispersion observed. What we are most interested in is the small details in the electronic structure around the Fermi level. The electronic properties discussed in Section 6.1 lie in the details of the low energy spectrum.

We focus first on the $\bar{\Gamma}\bar{X}$ direction, where, on the Fermi surface, only features coming from the bands γ and δ are contributing. The photoemission spectrum in Fig. 6.4(c) is taken along the red line shown in the inset. A intense band of s-p character, starting at 4 eV of binding energy, disperses parabolically upward out of normal emission. Here it hybridizes with several other bands creating hybridization gaps. At $\bar{\Gamma}$ at least two hole-like bands disperse close to the Fermi level. The photoemission intensity vanishes close to the Fermi level. In order to compare the ARPES with the calculated dispersion we compute the two dimensional curvature of the ARPES intensity spectrum.

The curvature is obtained using the approach described in Ref. [169]. This is a widely used method to locate the maxima in photoemission intensity profiles. The curvature image has highest intensity where the intensity peak reaches its maximum. This method can be

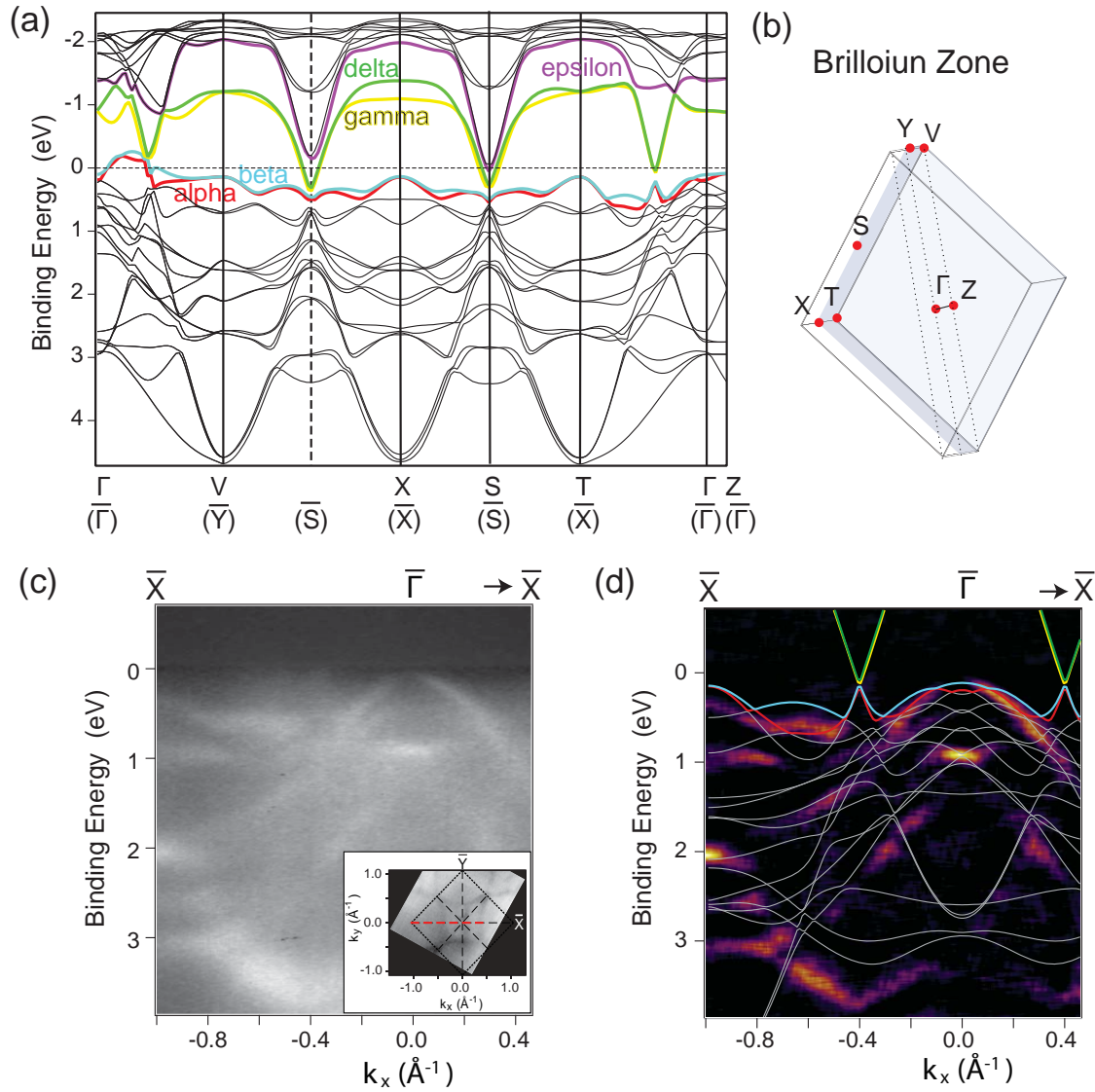


Figure 6.4: (a) Calculated bulk band structure along high symmetry directions. The high symmetry points are identified in the bulk Brillouin zone represented in (b) and their projections in the surface Brillouin zone is labelled in parenthesis. The five bands crossing the Fermi level are drawn in different colors. These are labelled as in Fig. 6.3 according to the Fermi surface to which they give rise. (b) Bulk Brillouin zone with high symmetry points. (c) Electronic structure along the $\bar{\Gamma}\bar{X}$ direction. Inset: the red dashed line represent the cut at the Fermi surface whose dispersion is shown in (c). (d) Curvature plot of the ARPES intensity presented in (c). Calculations of the band structure along the $\bar{\Gamma}\bar{X}$ direction are overlaid on the plot. Coloured lines are the analogous to the bands in (a) with the same colour.

used to display small details and band dispersion in the photoemission spectrum when this is too blurred or the background is too high for a convincing analysis.

The curvature spectrum is shown in Fig. 6.4(d), grey and coloured lines are the calculated band structure along the bulk Γ - X direction. We point out that comparing ARPES results with the bulk calculations is not optimal, because the \mathbf{k}_\perp value (photon energy dependent) in the ARPES data is unknown, and we only have knowledge of \mathbf{k}_\parallel . The band dispersion at different points in \mathbf{k}_\perp can be quite different and the comparison can incur in big mistakes. However, we have discussed how the low energy spectrum is strongly 2-dimensional in LaSb_2 , meaning that the dispersion is invariant in \mathbf{k}_\perp . Given these premises we expect that the dispersion of the bands close to the Fermi level will not be relevantly affected by the \mathbf{k}_\perp uncertainty.

The match between experiment and theory is overall quite good and several bands can be precisely reconciled. As expected the low energy spectrum finds a better match with the calculations. At the $\bar{\Gamma}$ point it is the β band (light blue) that barely touches the Fermi level (but does not). Along $\bar{\Gamma}\bar{X}$ we expect to see intensity at the Fermi level related to the outer square bands (γ and δ) in the Fermi surface. From the dispersion image it is not immediately clear where these are dispersing. The DFT shows that γ and δ drop below the Fermi level at $\mathbf{k}_\parallel \approx \pm 0.4 \text{ \AA}^{-1}$ creating small, shallow electron pockets. Interestingly these pockets show linear dispersion. At the bottom these states create some sort of gapped Dirac-like state with small hole bands at $\mathbf{k}_\parallel \approx \pm 0.4 \text{ \AA}^{-1}$ coming from the α and β bands. The calculated energy gap is 24 meV. The ARPES shows higher spectral intensity at the Fermi level at the position of the electron pockets. Indeed, it is these electron pockets that give rise to most of the warped square contour at the Fermi surface, well visible in the photoemission. The γ and δ bands behave as quasi-1 dimensional electron pockets with small carrier density and linear dispersion.

In order to visualize this better in the ARPES spectrum we zoom around the gapped Dirac state. We look at the dispersion of the state by taking three different cuts parallel to the $\bar{\Gamma}\bar{X}$ direction. ARPES and curvature plots are shown in Fig. 6.5(a-f). The dispersion cuts are taken along the red lines “1”, “2”, “3” of Fig. 6.5(g) following the dispersion of the state towards the \bar{S} point. Cut 1 is taken on the $\bar{\Gamma}\bar{X}$ line while the parallel cuts 2 and 3 are taken at $\mathbf{k}_y = 0.15$ and 0.25 \AA^{-1} respectively. The intensity of the electron pocket at the Fermi level in Cut 1, indicated by a red arrow, is faint leading to a smeared feature in the curvature plot. The state is better visualized in cut 2 (panels(c,d)). Here we find clearer spectroscopic signature of the state dispersion, also zoomed in panel (h). The state is broader at the Fermi level and becomes narrower at higher binding energies, indicating an electron-like dispersion. Above 0.3 eV of binding energy the state disperses outward again merging in the valence bands. Such an image is similar to what expected from the calculated band structure along $\bar{\Gamma}\bar{X}$ (Fig. 6.4(c)). Similarly the state is still well-defined along the cut 3. The material has to be considered a semimetal because of the small energy gaps between the α/β and γ and δ bands.

Following the squared contour we reach the \bar{S} point. The electron-like nature of the Fermi surface is best visible by considering a cut in the dispersion through the \bar{S} (\bar{S}') point, where γ and δ binding energy is expected to be the highest. Indeed the ARPES spectrum at \bar{S}' in Fig. 6.5(j,k), taken along the cut 4, shows a deep electron pocket dispersing above 0.2 eV of binding energy, while α and β are almost horizontal and do not contribute to the Dirac like dispersion in this point of the Brillouin zone. The comparison between the experimental data in the curvature plot and the calculations gives a good agreement. The

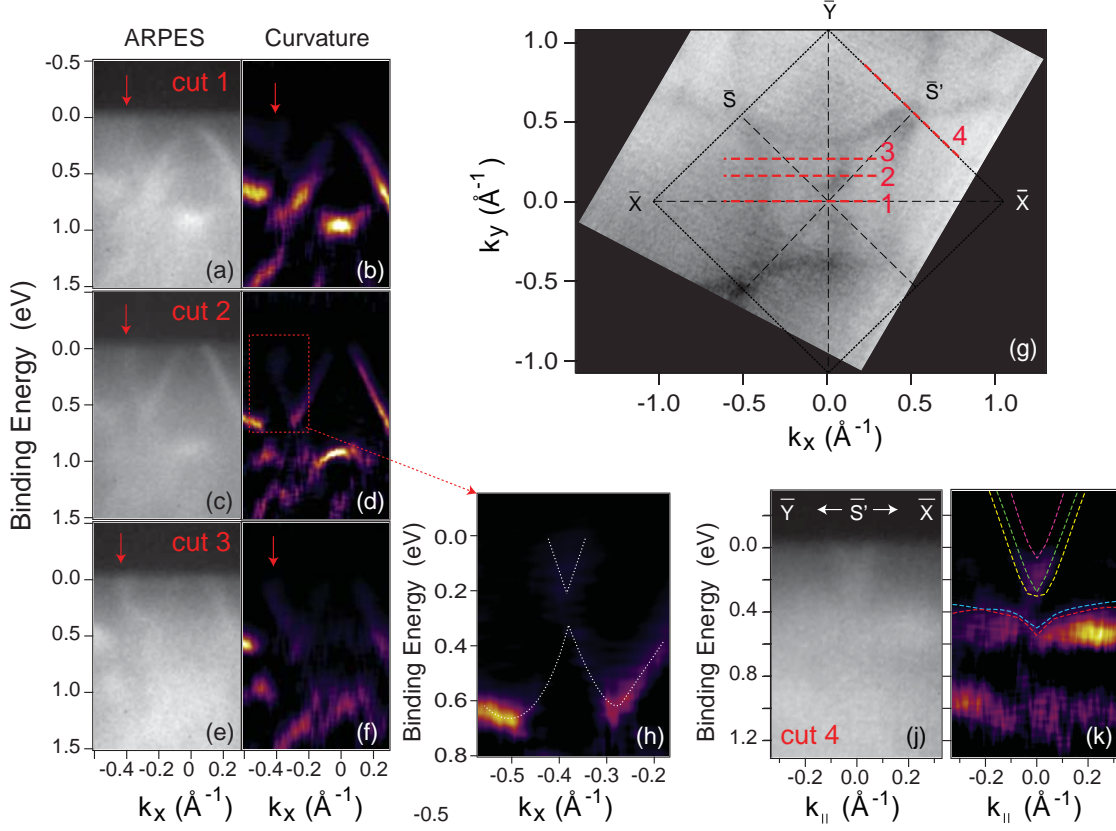


Figure 6.5: Photoemission intensity (a,c,e) and curvature plot (b,d,f) of the dispersion along three different cuts (1,2,3) in the k_x - k_y plane as shown in panel (g). Cut 1 is taken along the $\bar{\Gamma}\bar{X}$ direction and cut 2 and 3 are taken parallel to $\bar{\Gamma}\bar{X}$ at $k_y = 0.15 \text{ \AA}^{-1}$ and 0.25 \AA^{-1} , respectively. Red arrows point to the feature derived from the shallow electron pockets. (h) Zoom in of panel (d) in the region marked by the dashed rectangle. The white dashed lines are a guide for the eye representing the dispersion of the gapped Dirac-like state. (j) Dispersion along the \bar{Y} - \bar{S}' - \bar{X} direction as shown in cut 4 in (g). (k) Curvature plot of (j). The calculated low energy band structure is represented by coloured dashed lines. A clear electron pocket is found at the \bar{S}' point.

small ϵ Fermi surface is given by the ϵ purple band barely touching the Fermi level. From the experimental results it is impossible to say if this contributes to the Fermi surface.

At last we consider the dispersion along the second mirror line, $\bar{\Gamma}\bar{Y}$. A cut is taken along the line in Fig. 6.6(a). The low energy spectrum obtained by ARPES is shown in Fig. 6.6(b,c) before and after curvature, and compared to the calculated dispersion. In this direction the Dirac feature disappears. In the calculated band structure the conduction bands γ and δ do not reach the Fermi level. Moreover the bands α and β do not show the linear dispersion peak at $k_{\parallel} \approx \pm 0.4 \text{ \AA}^{-1}$. Instead α and β create two shallow hole pockets just off normal emission. These pockets are the oval contours in the Fermi surface plot. With a close-up look at the curvature plot around the Fermi level we find the dispersion of α and β is well reproduced by the calculations around $\bar{\Gamma}$ where a small dip in the dispersion is found. Here the higher band, β , is at a saddle point: the dip puts it in a local minimum along $\bar{\Gamma}\bar{Y}$ but it was found to be at maximum in the perpendicular direction $\bar{\Gamma}\bar{X}$, possibly

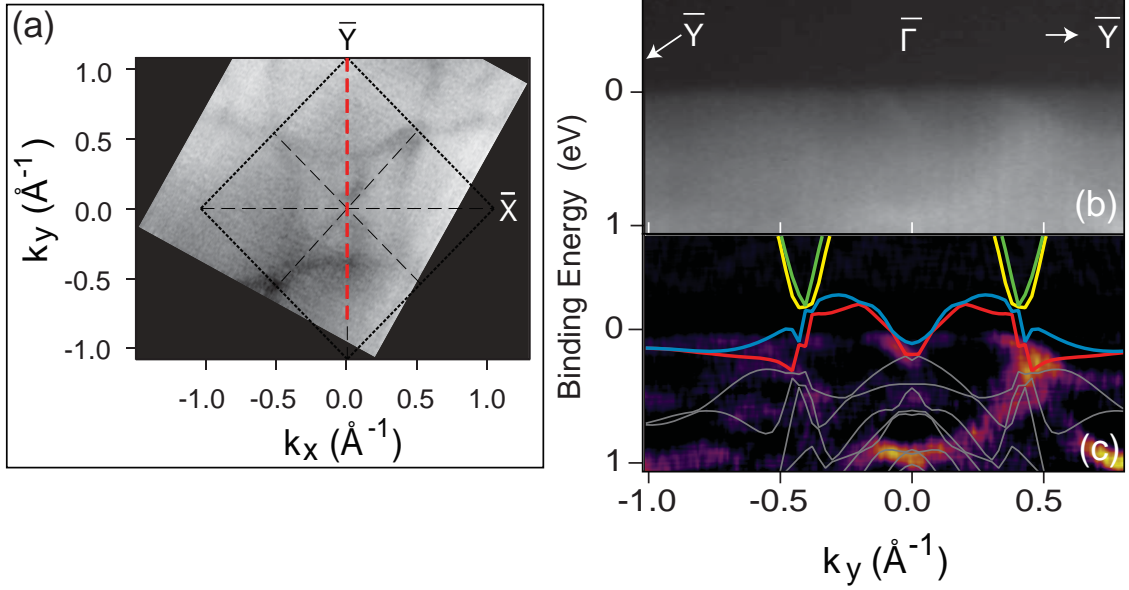


Figure 6.6: (a) Fermi surface obtained by ARPES. The red dashed line shows the cut along the $\bar{\Gamma}\bar{Y}$ direction plane whose dispersion is shown in (b). (b) Dispersion along $\bar{\Gamma}\bar{Y}$ as obtained by ARPES. (c) Curvature plot of the photoemission intensity of (b). The calculated band structure is represented by grey lines. The coloured lines are the five bands α - ϵ . Four massive hole pockets are found at the Fermi level (red and blue lines).

leading to a van Hove singularity. The electron pockets are pushed up above the Fermi level and are not visible in ARPES.

6.4 Features and properties of the electronic structure

We discuss now what are the possible implications of the examined band structure for the physical properties of LaSb_2 . We note, *in primo*, the strong one dimensionality of the portion of the Fermi surface derived from the bands γ and δ . The creation of two parallel edges gives rise to very strong nesting vectors at the Fermi surface. While this is not a condition sufficient for the creation of CDW, it is believed that it is vital to the existence of the CDW. With our measurement at 80 K we cannot, and did not, find signatures of CDWs in this material. Measurements at lower temperature for higher crystal quality are desired. We can only stress the presence of a remarkably nested surface. We find that LaSb_2 is a semimetal with very shallow pockets. All pockets at the Fermi level come in pairs, α/β and γ/δ , with very similar dispersion at low energies. It is impossible to disentangle the two contributions from the ARPES results because the distance between the bands is much smaller, from the calculation, than the resolution. We find four hole pockets with approximate effective mass along $\bar{\Gamma}\bar{Y}$ $m^* = 0.4 m_e$ (extracted from calculated band structure). The electron pockets are barely touching the Fermi level. The presence of both carrier types confirms the results of the Hall measurement behaviour at low magnetic field presented in Ref. [160]. At high field the Hall measurement show strongly predominant

hole behaviour. This can be induced by the change of the Fermi surface under magnetic field, one option being the discussed magnetic field induced CDW [7].

CDW is one of the possibilities expressed for the linear quantum magnetoresistance, an other discussed option is the quantum linear magnetoresistance. This was theorized by Abrikosov and details are found in his review in Ref. [44]. As a general rule, to push the electronic properties in a magnetic field to the quantum limit, the individual quantum levels associated to the electron orbits must be distinct and the condition $\hbar\omega_c \gg k_B T$, where $\omega_c = qB/m^*$ is the cyclotron frequency, must hold. It is straight forward to see that for this condition to be fulfilled at low magnetic field the effective mass of the carriers must go to zero. The electrons behave as massless particle when they are Dirac particles. The advantageous conditions for the quantum magnetoresistance to happen are very small carrier density and a transition to a massless linear dispersion. This was experimented in the case of InSb and silver chalcogenides where a transition from small direct band gap with low carrier density to Dirac-like semimetal occurs [170, 171]. We can notice that the band structure of LaSb_2 is characterized by the right ingredients: low density pockets with linear dispersion in the closeness of a possible transition to a Dirac state. On the other hand we have seen that LaSb_2 also presents massive hole pockets (α and β) which cannot be reconciled to the quantum limit conditions. A possibility, ventured by Abrikosov, is that carriers from portions of the Fermi surface carry the quantum conductivity while the remaining part carry ordinary conductivity. The two contribution sum up. The linear MR can be achieved when the quantum contribution to the conductivity is higher than the classic one. This is possible for samples with a high concentration of defects. The scattering process allow the electrons to hop at different quantized orbits allowing the quantum conductivity in magnetic fields. On the light of our results we cannot confirm the mechanism of the magnetoresistance but our findings in the electronic structure seem to point towards the assumption that quantum linear magnetoresistance might be the key.

At last we decide to compare the electronic structure of LaSb_2 with a similar material to have a better insight on the relation between chemical/crystal structure, electronic structure and physical properties. For this purpose we perform ARPES on NdSb_2 single crystals. NdSb_2 has the same crystal structure of LaSb_2 and it also shows linear non-saturating MR. In contrast to LaSb_2 , NdSb_2 presents several different magnetic phases at low temperature [7]. The preparation of the sample surface is similar to the case of LaSb_2 .

Fig. 6.7 shows the salient features of the photoemission spectrum. The Fermi surface of NdSb_2 is very similar to the case of LaSb_2 . A warped square contour on the outside and two rounded contours in the $\bar{\Gamma}\bar{Y}$ direction. It is instructive to examine the dispersion cut along $\bar{\Gamma}\bar{X}$ (Fig. 6.7(b)). In LaSb_2 the electron pockets giving rise to the squared contour are barely touching the Fermi level and, due to the low resolution, their identification is a hard task. For NdSb_2 we find these same pockets at $\pm 0.37 \text{ \AA}^{-1}$. The electron pockets are clearly distinguishable down to few tens of meV below the Fermi level (zoomed images in panel (c)). On the other side the sharp upward dispersion of the valence band at $\pm 0.37 \text{ \AA}^{-1}$ reveals the linear behaviour and the direct gap. Spectral intensity in the gap is due to the spectral broadening of the feature. The presence of the gap is better visible by looking at the two dimensional curvature. The magnitude of the gap is 0.28(5) eV.

In conclusion, we investigated the electronic structure of LaSb_2 with ARPES and *ab initio* calculations. A good match between experiment and theory was found. The electronic structure at the Fermi level is characterized by strong 2 dimensionality and most of the Fermi surface has open orbits in the \mathbf{k}_\perp direction. Four massive hole pockets are

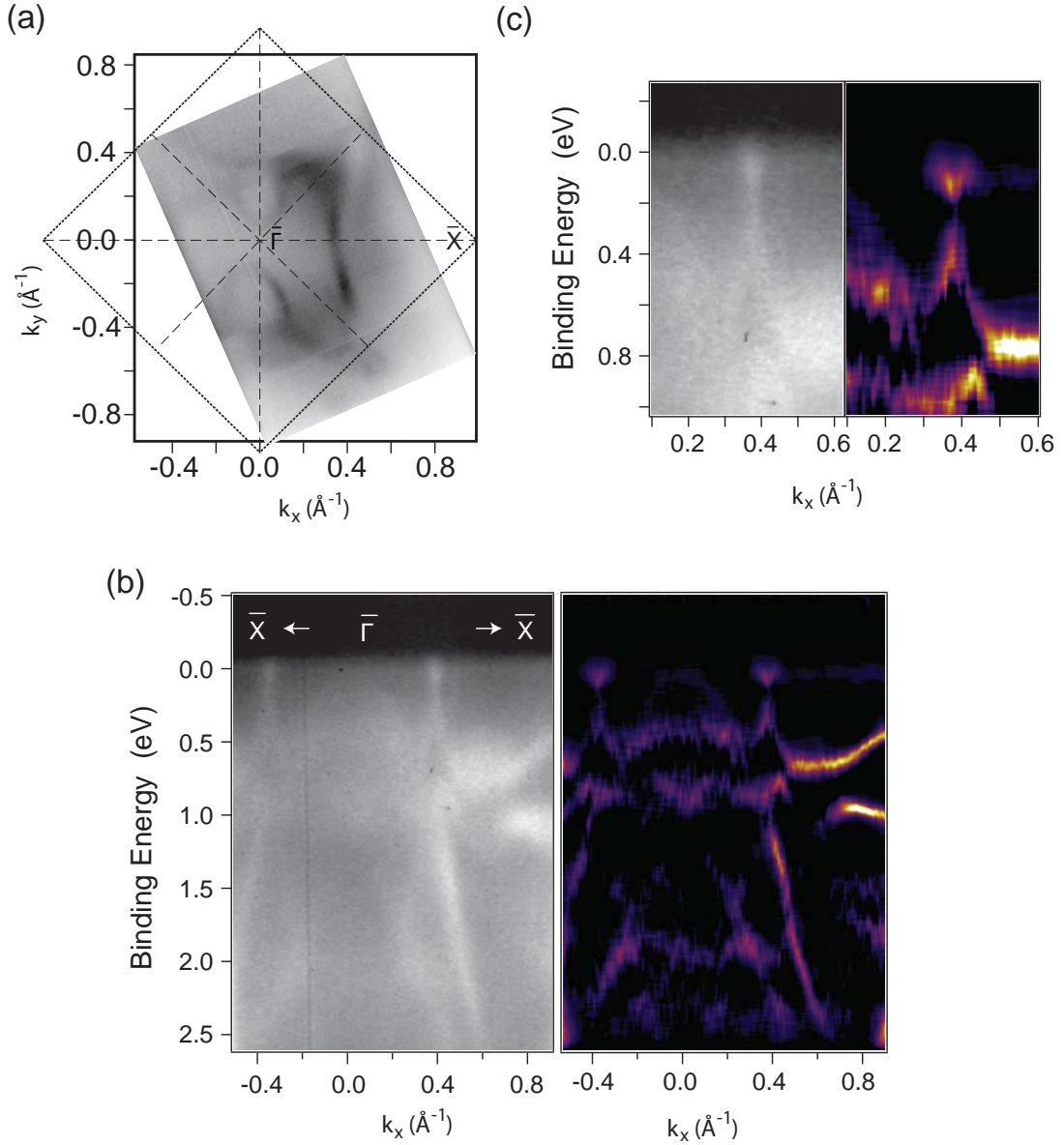


Figure 6.7: (a) Fermi surface of NdSb₂ obtained by ARPES using photon energy $h\nu = 25$ eV. The surface Brillouin zone is sketched on top. (b) Dispersion cut along the $\bar{\Gamma}\bar{X}$ direction using photon energy $h\nu = 56$ eV. On the left: ARPES intensity plot. On the right: Curvature plot. (c) Zoom in of the dispersion around the gapped Dirac-like state at $\bar{\Gamma}\bar{X}$. On the left: ARPES intensity plot. On the right: Curvature plot. A small gap of 0.28(5) eV is found.

present together with almost linearly dispersing low carrier density states. Here a small direct gap between valence and conduction pockets is found just at the Fermi level and the bands assume a linear dispersion. We speculate that this could give rise to quantum linear magnetoresistance. Similar electronic structure is found in the homologous compound NdSb₂, where a clear presence of gapped Dirac states is also found.

Chapter 7

Conclusive Remarks

The electronic structure of topological insulators and rare-earth diantimonides has been investigated using ARPES as principal tool. The absorption of adatoms on the surface of bismuth chalcogenides topological insulators proved to fruitfully modify the low energy electronic structure maintaining the topological insulator features, with interesting implication for TI-based devices. The rare-earth antimonides revealed an unusual electronic structure with Dirac-like states and interesting physical properties, in the hope that these materials will receive more attention in the future. Let summarize the main achievements in the following:

Bi₂Te₃ bulk band structure: the bulk band structure of TI Bi₂Te₃ has been investigated by ARPES and DFT calculations in the framework of LDA and *GW*. The comparison revealed a better overall agreement with *GW* revealing the important role of many-body effects. An indirect band gap was found.

Surface modification of Topological insulators: TIs surfaces have been modified by atoms adsorption. First rubidium was adsorbed on Bi₂Te₂Se and Bi₂Te₃. The n-doping effect of the Rb induced a 2DEG on the surface with strong spin-orbit splitting. It was revealed that such a 2DEG is strongly anisotropic, not only in its shape but also in the splitting. The bands were modelled with a modified Rashba Hamiltonian that included the effect of anisotropic band dispersion. This 2DEG goes beyond the conventional concept of Rashba splitting and opens the way to new anisotropic spin transport phenomena. Bi₂Te₂Se was doped on the surface with Ni and Fe as well to investigate potential magnetic properties. Strikingly XMCD results showed that Fe on Bi₂Te₂Se has a out of plane easy direction of magnetization while Ni has quenched magnetic moment. ARPES revealed a n-doping effect of the transition metals on the electronic structure of Bi₂Te₂Se, with no indication of magnetic-related features.

Bi/Bi₂Se₃: Bi bilayer, a 2D TI, has been grown on the 3D TI Bi₂Se₃. The electronic structure at the interfaces has been investigated by ARPES and FT-STs. For the interpretation of the latter a semi-theoretical method was employed using DFT slab calculation to create a three-dimensional simulated spectral function. This has then been used to perform JDOS simulations to be compared with the FT-STs QPI patterns. The interface band structure reveals a charge transfer between the bilayer and the Bi₂Se₃ and a strong hybridization with the substrate. A new Dirac-like feature

is found at the interface. Analysis of the scattering channels demonstrated that the novel Dirac cone is susceptible to interband scattering.

Electronic structure of LaSb₂ and NdSb₂: The electronic structure of LaSb₂ is here reported for the first time. The Fermi surface is composed by very shallow electron pockets and four higher effective mass hole pockets. The electron pockets create a direct band gap with linear dispersing valence states, as seen also for NdSb₂, and are found to be fairly one-dimensional in character. The interesting linear -non saturating magnetoresistance found for these materials might be explained by the linear dispersion of the electron pockets.

Bibliography

- [1] Y. Ando. *Topological insulator materials*. Journal of the Physical Society of Japan, 82(10):102001 (2013). <http://journals.jps.jp/doi/pdf/10.7566/JPSJ.82.102001>.
- [2] M. Z. Hasan and C. L. Kane. *Colloquium: Topological insulators*. Rev. Mod. Phys., 82:3045 (2010).
- [3] C. Kane and E. Mele. *Z₂ topological order and the quantum spin Hall effect*. Phys. Rev. Lett., 95(14) (2005).
- [4] M. Michiardi, I. Aguilera, M. Bianchi, V. E. de Carvalho, L. O. Ladeira, N. G. Teixeira, E. A. Soares, C. Friedrich, S. Blügel, and P. Hofmann. *Bulk band structure of Bi₂Te₃*. Phys. Rev. B, 90:075105 (2014).
- [5] M. Michiardi, M. Bianchi, M. Dendzik, J. A. Miwa, M. Hoesch, T. K. Kim, P. Matzen, J. Mi, M. Bremholm, B. B. Iversen, and P. Hofmann. *Strongly anisotropic spin-orbit splitting in a two-dimensional electron gas*. Phys. Rev. B, 91:035445 (2015).
- [6] A. Eich, M. Michiardi, G. Bihlmayer, X.-G. Zhu, J.-L. Mi, B. B. Iversen, R. Wiesendanger, P. Hofmann, A. A. K. hajetoorians, and J. Wiebe. *Intra- and interband electron scattering in a hybrid topological insulator: Bismuth bilayer on Bi₂Se₃*. Phys. Rev. B, 90:155414 (2014).
- [7] S. L. Bud'ko, P. C. Canfield, C. H. Mielke, and A. H. Lacerda. *Anisotropic magnetic properties of light rare-earth dioximonides*. Phys. Rev. B, 57:13624 (1998).
- [8] J. A. Galvis, H. Suderow, S. Vieira, S. L. Bud'ko, and P. C. Canfield. *Scanning tunneling microscopy in the superconductor LaSb₂*. Phys. Rev. B, 87:214504 (2013).
- [9] M. König, S. Wiedmann, C. Brüne, A. Roth, H. Buhmann, L. W. Molenkamp, X.-L. Qi, and S.-C. Zhang. *Quantum spin Hall insulator state in HgTe quantum wells*. Science, 318(5851):766 (2007). <http://www.sciencemag.org/content/318/5851/766.full.pdf>.
- [10] A. R. Mellnik, J. S. Lee, A. Richardella, J. L. Grab, P. J. Mintun, M. H. Fischer, A. Vaezi, A. Manchon, E.-A. Kim, N. Samarth, and D. C. Ralph. *Spin-transfer torque generated by a topological insulator*. Nature, 511(7510):449 (2014).
- [11] X.-L. Qi, R. Li, J. Zang, and S.-C. Zhang. *Inducing a magnetic monopole with topological surface states*. Science, 323(5918):1184 (2009). <http://www.sciencemag.org/content/323/5918/1184.full.pdf>.

-
- [12] L. A. Wray, S.-Y. Xu, Y. Xia, Y. S. Hor, D. Qian, A. V. Fedorov, H. Lin, A. Bansil, R. J. Cava, and M. Z. Hasan. *Observation of topological order in a superconducting doped topological insulator*. Nat Phys, 6(11):855 (2010).
- [13] C. Kittel. *Solid State Physics*. Wiley (1995).
- [14] N. E. Ashcroft and N. D. Mermin. *Solid State Physics*. Saunders College, Philadelphia, international ed. (1976).
- [15] W. Shockley. *On the surface states associated with a periodic potential*. Phys. Rev., 56:317 (1939).
- [16] I. E. Tamm. *On the possible bound states of electrons on a crystal surface*. Phys. Z. Sowjetunion, 1:733 (1932).
- [17] K. Fukutani, H. Hayashi, T. T. Scott, Y. Nagata, T. Horike, J. Jiang, H. Iwasawa, K. Shimada, Y. B. Losovyj, and P. A. Dowben. *Symmetry-protected surface state on Mo(112)*. Journal of Physics: Condensed Matter, 26(15):155501 (2014).
- [18] R. O. Jones. *Intrinsic surface states in semiconductors*. Phys. Rev. Lett., 20:992 (1968).
- [19] E. Caruthers, L. Kleinman, and G. P. Alldredge. *Electronic surface states on (111) aluminum*. Phys. Rev. B, 9:3330 (1974).
- [20] P. Heimann, H. Neddermeyer, and H. F. Roloff. *Ultraviolet photoemission for intrinsic surface states of the noble metals*. Journal of Physics C: Solid State Physics, 10(1):L17 (1977).
- [21] Y. A. Bychkov and E. I. Rashba. *Oscillatory effects and the magnetic susceptibility of carriers in inversion layers*. Journal of Physics C: Solid State Physics, 17(33):6039 (1984).
- [22] Y. A. Bychkov and E. I. Rashba. *Properties of a 2D electron gas with lifted spectral degeneracy*. JETP, 39:78 (1984).
- [23] S. LaShell, B. A. McDougall, and E. Jensen. *Spin splitting of an Au(111) surface state band observed with angle resolved photoelectron spectroscopy*. Phys. Rev. Lett., 77:3419 (1996).
- [24] S. Datta and B. Das. *Electronic analog of the electro-optic modulator*. Appl. Phys. Lett., 56:665 (1990).
- [25] G. Dresselhaus. *Spin-orbit coupling effects in zinc blende structures*. Phys. Rev., 100:580 (1955).
- [26] K. Ishizaka, M. S. Bahramy, H. Murakawa, M. Sakano, T. Shimojima, T. Sonobe, K. Koizumi, S. Shin, H. Miyahara, A. Kimura, K. Miyamoto, T. Okuda, H. Namatame, M. Taniguchi, R. Arita, N. Nagaosa, K. Kobayashi, Y. Murakami, R. Kumai, Y. Kaneko, Y. Onose, and Y. Tokura. *Giant Rashba-type spin splitting in bulk BiTeI*. Nat Mater, 10(7):521 (2011).

- [27] D. Xiao, G.-B. Liu, W. Feng, X. Xu, and W. Yao. *Coupled spin and valley physics in monolayers of MoS_2 and other group-VI dichalcogenides*. Phys. Rev. Lett., 108:196802 (2012).
- [28] M. Heide, G. Bihlmayer, P. Mavropoulos, A. Bringer, and S. Blügel. *Spin orbit driven physics at surfaces*. Newsletter of the Psi-K Network, 78 (2006).
- [29] J. H. Dil. *Spin and angle resolved photoemission on non-magnetic low-dimensional systems*. Journal of Physics: Condensed Matter, 21(40):403001 (2009).
- [30] D. Bercioux and P. Lucignano. *Quantum transport in Rashba spin-orbit materials: a review*. Reports on Progress in Physics, 78(10):106001 (2015).
- [31] A. Manchon, H. C. Koo, J. Nitta, S. M. Frolov, and R. A. Duine. *New perspectives for Rashba spin-orbit coupling*. Nat Mater, 14(9):871 (2015).
- [32] P. Hofmann. *Synchrotron-radiation studies of topological insulators*. arXiv, arXiv:1210.2672v2 [cond-mat.str-el] (2012).
- [33] X.-L. Qi and S.-C. Zhang. *Topological insulators and superconductors*. Rev. Mod. Phys., 83:1057 (2011).
- [34] J. E. Moore. *The birth of topological insulators*. Nature, 464(7286):194 (2010).
- [35] D. J. Thouless, M. Kohmoto, M. P. Nightingale, and M. den Nijs. *Quantized Hall conductance in a two-dimensional periodic potential*. Phys. Rev. Lett., 49:405 (1982).
- [36] L. Fu and C. L. Kane. *Topological insulators with inversion symmetry*. Phys. Rev. B, 76:045302 (2007).
- [37] L. Fu, C. L. Kane, and E. J. Mele. *Topological insulators in three dimensions*. Phys. Rev. Lett., 98:106803 (2007).
- [38] M. Bianchi. *PhD Thesis: Electronic structure and electron dynamics of the topological Bi_2Se_3* . Ph.D. thesis, Aarhus University (2013).
- [39] K. S. Novoselov, A. K. Geim, S. V. Morozov, D. Jiang, M. I. Katsnelson, I. V. Grigorieva, S. V. Dubonos, and A. A. Firsov. *Two-dimensional gas of massless Dirac fermions in graphene*. Nature, 438(7065):197 (2005).
- [40] A. Vishwanath. *Dirac nodes and quantized thermal Hall effect in the mixed state of d -wave superconductors*. Phys. Rev. B, 66:064504 (2002).
- [41] L. Fu. *Topological crystalline insulators*. Phys. Rev. Lett., 106:106802 (2011).
- [42] S.-Y. Xu, I. Belopolski, N. Alidoust, M. Neupane, G. Bian, C. Zhang, R. Sankar, G. Chang, Z. Yuan, C.-C. Lee, S.-M. Huang, H. Zheng, J. Ma, D. S. Sanchez, B. Wang, A. Bansil, F. Chou, P. P. Shibayev, H. Lin, S. Jia, and M. Z. Hasan. *Discovery of a Weyl fermion semimetal and topological Fermi arcs*. Science, 349(6248):613 (2015). <http://www.sciencemag.org/content/349/6248/613.full.pdf>.

- [43] O. Vafek and A. Vishwanath. *Dirac fermions in solids: From high- T_c cuprates and graphene to topological insulators and Weyl semimetals*. Annual Review of Condensed Matter Physics, 5(1):83 (2014). <http://dx.doi.org/10.1146/annurev-conmatphys-031113-133841>.
- [44] A. A. Abrikosov. *Quantum linear magnetoresistance; solution of an old mystery*. Journal of Physics A: Mathematical and General, 36:9119 (2003).
- [45] H. Hertz. *Über einen Einfluss des ultravioletten Lichtes auf die elektrische Entladung*. Annalen der Physik, 267(8):983 (1887).
- [46] A. Einstein. *über einen die erzeugung und verwandlung des lichtes betreffenden heuristischen gesichtspunkt*. Annalen der Physik, 322(6):132 (1905).
- [47] A. Damascelli, Z. Hussain, and Z.-X. Shen. *Angle-resolved photoemission studies of the cuprate superconductors*. Rev. Mod. Phys., 75:473 (2003).
- [48] S. Hüfner. *Photoelectron Spectroscopy*. Springer Berlin Heidelberg (1996).
- [49] S. Kevan. *Angle Resolved Photoemission*. Elsevier, Amsterdam (1992).
- [50] B. Feuerbacher, B. Fitton, and R. Willis. *Photoemission and the electronic properties of surfaces*. Wiley (1978). ISBN 9780471995555.
- [51] R. Comin and A. Damascelli. *ARPES: A probe of electronic correlations*. arXiv, arXiv:1303.1438 [cond-mat.str-el] (2013).
- [52] M. Wöhlecke, A. Baalman, and M. Neumann. *Zero-slope points and electronic energy bandmapping*. Solid State Communications, 49(3):217 (1984).
- [53] P. Hofmann, I. Y. Sklyadneva, E. D. L. Rienks, and E. V. Chulkov. *Electron-phonon coupling at surfaces and interfaces*. New Journal of Physics, 11(12):125005 (2009).
- [54] A. Bostwick, T. Ohta, T. Seyller, K. Horn, and E. Rotenberg. *Quasiparticle dynamics in graphene*. Nat Phys, 3(1):36 (2007).
- [55] F. Mazzola, J. W. Wells, R. Yakimova, S. Ulstrup, J. A. Miwa, R. Balog, M. Bianchi, M. Leandersson, J. Adell, P. Hofmann, and T. Balasubramanian. *Kinks in the σ band of graphene induced by electron-phonon coupling*. Phys. Rev. Lett., 111:216806 (2013).
- [56] T. Valla, A. V. Fedorov, P. D. Johnson, B. O. Wells, S. Hulbert, Q. Li, G. Gu, and N. Koshizuka. *Evidence for quantum critical behavior in the optimally doped cuprate $Bi_2Sr_2CaCu_2O_{8+\delta}$* . Science, 285(5436):2110 (1999).
- [57] C. Kirkegaard, T. K. Kim, and P. Hofmann. *Self-energy determination and electron-phonon coupling on $Bi(110)$* . New journal of physics, 7:99 (2005).
- [58] P. Hofmann. *Surface physics: An Introduction* (2013).
- [59] <http://www.isa.au.dk/index.asp>.

- [60] E. Lægsgaard, F. Besenbacher, M. Mortensen, and I. Stensgaard. *A fully automated, "thimble-size" scanning tunnelling microscope*. Journal of Microscopy, 152:663 (1988).
- [61] L. Petersen, P. Hofmann, E. Plummer, and F. Besenbacher. *Fourier transform-TM: determining the surface Fermi contour*. Journal of Electron Spectroscopy and Related Phenomena, 109(1-2):97 (2000).
- [62] W. Krenner, D. Kühne, F. Klappenberger, and J. V. Barth. *Assessment of scanning tunneling spectroscopy modes inspecting electron confinement in surface-confined supramolecular networks*. Scientific Reports, 3:1454 (2013).
- [63] R. Shantyr. *Scanning tunneling microscopy/scanning tunneling spectroscopy on growth, atomic and electronic structure of Co oxide and Mn oxide films on Ag(001)*. Ph.D. thesis, Martin-Luther-Universität Halle-Wittenberg (2004).
- [64] A. M. Gabovich, L. G. Il'chenko, E. A. Pashitski, and Y. A. Romanov. *Screening of charges and Friedel oscillations of the electron density in metals having differently shaped Fermi surfaces*. Zh. Eksp. Teor. Fi, 75:249 (1978).
- [65] J. I. Pascual, G. Bihlmayer, Y. M. Koroteev, H.-P. Rust, G. Ceballos, M. Hansmann, K. Horn, E. V. Chulkov, S. Blügel, P. M. Echenique, and P. Hofmann. *Role of spin in quasiparticle interference*. Phys. Rev. Lett., 93:196802 (2004).
- [66] H. Zhang, C.-X. Liu, X.-L. Qi, X. Dai, Z. Fang, and S.-C. Zhang. *Topological insulators in Bi_2Se_3 , Bi_2Te_3 and Sb_2Te_3 with a single Dirac cone on the surface*. Nat Phys, 5(6):438 (2009).
- [67] Y. Xia, D. Qian, D. Hsieh, L. Wray, A. Pal, H. Lin, A. Bansil, D. Grauer, Y. S. Hor, R. J. Cava, and M. Z. Hasan. *Observation of a large-gap topological-insulator class with a single Dirac cone on the surface*. Nature Physics, 5 (2009).
- [68] *Web of Science*.
- [69] R. J. Cava, H. Ji, M. K. Fuccillo, Q. D. Gibson, and Y. S. Hor. *Crystal structure and chemistry of topological insulators*. J. Mater. Chem. C, 1:3176 (2013).
- [70] L.-L. Wang and D. D. Johnson. *Ternary tetradymite compounds as topological insulators*. Phys. Rev. B, 83:241309 (2011).
- [71] Z. Xu, X. Guo, M. Yao, H. He, L. Miao, L. Jiao, H. Liu, J. Wang, D. Qian, J. Jia, W. Ho, and M. Xie. *Anisotropic topological surface states on high-index Bi_2Se_3 films*. Advanced Materials, 25(11):1557 (2013).
- [72] I. A. Nechaev, R. C. Hatch, M. Bianchi, D. Guan, C. Friedrich, I. Aguilera, J. L. Mi, B. B. Iversen, S. Blügel, P. Hofmann, and E. V. Chulkov. *Evidence for a direct band gap in the topological insulator Bi_2Se_3 from theory and experiment*. Phys. Rev. B, 87:121111 (2013).
- [73] L. Fu. *Hexagonal warping effects in the surface states of the topological insulator Bi_2Te_3* . Phys. Rev. Lett., 103(26):266801 (2009).

- [74] E. Frantzeskakis and M. Gioni. *Anisotropy effects on rashba and topological insulator spin-polarized surface states: A unified phenomenological description*. Phys. Rev. B, 84:155453 (2011).
- [75] E. Kioupakis, M. L. Tiago, and S. G. Louie. *Quasiparticle electronic structure of bismuth telluride in the GW approximation*. Phys. Rev. B, 82:245203 (2010).
- [76] B. Y. Yavorsky, N. F. Hinsche, I. Mertig, and P. Zahn. *Electronic structure and transport anisotropy of Bi_2Te_3 and Sb_2Te_3* . Phys. Rev. B, 84:165208 (2011).
- [77] I. A. Nechaev and E. V. Chulkov. *Quasiparticle band gap in the topological insulator Bi_2Te_3* . Phys. Rev. B, 88:165135 (2013).
- [78] A. Herdt, L. Plucinski, G. Bihlmayer, G. Mussler, S. Döring, J. Krumrain, D. Grützmacher, S. Blügel, and C. M. Schneider. *Spin-polarization limit in Bi_2Te_3 Dirac cone studied by angle- and spin-resolved photoemission experiments and ab initio calculations*. Phys. Rev. B, 87:035127 (2013).
- [79] S. V. Faleev, M. van Schilfgaarde, and T. Kotani. *All-electron self-consistent GW approximation: Application to Si, MnO, and NiO*. Phys. Rev. Lett., 93:126406 (2004).
- [80] C. Friedrich, A. Schindlmayr, S. Blügel, and T. Kotani. *Elimination of the linearization error in GW calculations based on the linearized augmented-plane-wave method*. Phys. Rev. B, 74:045104 (2006).
- [81] O. V. Yazyev, E. Kioupakis, J. E. Moore, and S. G. Louie. *Quasiparticle effects in the bulk and surface-state bands of Bi_2Se_3 and Bi_2Te_3 topological insulators*. Phys. Rev. B, 85:161101 (2012).
- [82] J. Vidal, X. Zhang, L. Yu, J.-W. Luo, and A. Zunger. *False-positive and false-negative assignments of topological insulators in density functional theory and hybrids*. Phys. Rev. B, 84:041109 (2011).
- [83] R. Sakuma, C. Friedrich, T. Miyake, S. Blügel, and F. Aryasetiawan. *GW calculations including spin-orbit coupling: Application to Hg chalcogenides*. Phys. Rev. B, 84:085144 (2011).
- [84] A. Svane, N. E. Christensen, M. Cardona, A. N. Chantis, M. van Schilfgaarde, and T. Kotani. *Quasiparticle band structures of $\beta\text{-HgS}$, HgSe , and HgTe* . Phys. Rev. B, 84:205205 (2011).
- [85] Z. Zhu, Y. Cheng, and U. Schwingenschlögl. *Topological phase diagrams of bulk and monolayer $\text{TiS}_{2-x}\text{Te}_x$* . Phys. Rev. Lett., 110:077202 (2013).
- [86] I. Aguilera, C. Friedrich, G. Bihlmayer, and S. Blügel. *GW study of topological insulators Bi_2Se_3 , Bi_2Te_3 , and Sb_2Te_3 : Beyond the perturbative one-shot approach*. Phys. Rev. B, 88:045206 (2013).
- [87] F. J. Himpsel. *Experimental determination of bulk energy band dispersions*. Applied Optics, 19:3970 (1980).
- [88] <http://www.flapw.de>.

- [89] C. Friedrich, S. Blügel, and A. Schindlmayr. *Efficient implementation of the GW approximation within the all-electron FLAPW method*. Phys. Rev. B, 81:125102 (2010).
- [90] C. Li, A. J. Freeman, H. J. F. Jansen, and C. L. Fu. *Magnetic anisotropy in low-dimensional ferromagnetic systems: Fe monolayers on Ag(001), Au(001), and Pd(001) substrates*. Phys. Rev. B, 42:5433 (1990).
- [91] P. Pecheur and G. Toussaint. *Tight-binding studies of crystal stability and defects in Bi_2Te_3* . Journal of Physics and Chemistry of Solids, 55(4):327 (1994).
- [92] S. Eremeev, Y. Koroteev, and E. Chulkov. *Effect of the atomic composition of the surface on the electron surface states in topological insulators $A_2^V B_3^VI$* . JETP Letters, 91:387 (2010).
- [93] L. Plucinski, A. Herdt, S. Fahrenndorf, G. Bihlmayer, G. Mussler, S. Doring, J. Kampmeier, F. Matthes, D. E. Burgler, D. Grutzmacher, S. Blugel, and C. M. Schneider. *Electronic structure, surface morphology, and topologically protected surface states of Sb_2Te_3 thin films grown on Si(111)*. Journal of Applied Physics, 113(5):053706 (2013).
- [94] C. Pauly, G. Bihlmayer, M. Liebmann, M. Grob, A. Georgi, D. Subramaniam, M. R. Scholz, J. Sánchez-Barriga, A. Varykhalov, S. Blügel, O. Rader, and M. Morgenstern. *Probing two topological surface bands of Sb_2Te_3 by spin-polarized photoemission spectroscopy*. Phys. Rev. B, 86:235106 (2012).
- [95] I. G. Austin. *The optical properties of bismuth telluride*. Proc. Phys. Soc. London, 72:545 (1958).
- [96] C. Li, A. L. Ruoff, and C. W. Spencer. *Effect of pressure on the energy gap of Bi_2Te_3* . J. Appl. Phys., 32:1733 (1961).
- [97] R. Sehr and L. Testardi. *The optical properties of p-type Bi_2Te_3 - Sb_2Te_3 alloys between 2-15 microns*. J. Phys. Chem Solids, 23:1219 (1962).
- [98] G. A. Thomas, D. H. Rapkine, R. B. V. Dover, L. F. Mattheiss, W. A. Sunder, L. F. Schneemeyer, and J. V. Waszczak. *Large electronic-density increase on cooling a layered metal: Doped Bi_2Te_3* . Phys. Rev. B, 46:1553 (1992).
- [99] N. F. Mott. *The theory of crystal rectifiers*. Proceedings of the Royal Society of London A: Mathematical, Physical and Engineering Sciences, 171(944):27 (1939).
- [100] N. F. Mott. *Note on the contact between a metal and an insulator or semi-conductor*. Mathematical Proceedings of the Cambridge Philosophical Society, 34:568 (1938).
- [101] Z. Zhang and J. John T. Yates. *Band bending in semiconductors: Chemical and physical consequences at surfaces and interfaces*. Chemical Reviews, 112(10):5520 (2012). <http://dx.doi.org/10.1021/cr3000626>.
- [102] P. D. C. King, R. C. Hatch, M. Bianchi, R. Ovsyannikov, C. Lupulescu, G. Landolt, B. Slomski, J. H. Dil, D. Guan, J. L. Mi, E. D. L. Rienks, J. Fink, A. Lindblad, S. Svensson, S. Bao, G. Balakrishnan, B. B. Iversen, J. Osterwalder, W. Eberhardt, F. Baumberger, and P. Hofmann. *Large tunable Rashba spin splitting of a two-dimensional electron gas in Bi_2Se_3* . Phys. Rev. Lett., 107(9):096802 (2011).

- [103] M. Bianchi, R. C. Hatch, Z. Li, P. Hofmann, F. Song, J. Mi, B. B. Iversen, Z. M. A. El-Fattah, P. Löptien, L. Zhou, A. A. Khajetoorians, J. Wiebe, R. Wiesendanger, and J. W. Wells. *Robust surface doping of Bi_2Se_3 by rubidium intercalation*. ACS Nano, 6(8):7009 (2012). <http://dx.doi.org/10.1021/nn3021822>.
- [104] A. Ohtomo and H. Y. Hwang. *A high-mobility electron gas at the $\text{LaAlO}_3/\text{SrTiO}_3$ heterointerface*. Nature, 427(6973):423 (2004).
- [105] T. Ando, A. B. Fowler, and F. Stern. *Electronic properties of two-dimensional systems*. Rev. Mod. Phys., 54:437 (1982).
- [106] N. Reyren, S. Thiel, A. D. Caviglia, L. F. Kourkoutis, G. Hammerl, C. Richter, C. W. Schneider, T. Kopp, A.-S. Rüetschi, D. Jaccard, M. Gabay, D. A. Muller, J.-M. Triscone, and J. Mannhart. *Superconducting interfaces between insulating oxides*. Science, 317(5842):1196 (2007). <http://www.sciencemag.org/content/317/5842/1196.full.pdf>.
- [107] D. C. Tsui, H. L. Stormer, and A. C. Gossard. *Two-dimensional magnetotransport in the extreme quantum limit*. Phys. Rev. Lett., 48:1559 (1982).
- [108] J. A. Miwa, P. Hofmann, M. Y. Simmons, and J. W. Wells. *Direct measurement of the band structure of a buried two-dimensional electron gas*. Phys. Rev. Lett., 110:136801 (2013).
- [109] V. Y. Aristov, G. Le Lay, V. M. Zhilin, G. Indlekofer, C. Grupp, A. Taleb-Ibrahimi, and P. Soukiassian. *Direct measurement of quantum-state dispersion in an accumulation layer at a semiconductor surface*. Phys. Rev. B, 60:7752 (1999).
- [110] L. Colakerol, T. D. Veal, H.-K. Jeong, L. Plucinski, A. DeMasi, T. Learmonth, P.-A. Glans, S. Wang, Y. Zhang, L. F. J. Piper, P. H. Jefferson, A. Fedorov, T.-C. Chen, T. D. Moustakas, C. F. McConville, and K. E. Smith. *Quantized electron accumulation states in indium nitride studied by angle-resolved photoemission spectroscopy*. Phys. Rev. Lett., 97:237601 (2006).
- [111] P. D. C. King, T. D. Veal, C. F. McConville, J. Zúñiga Pérez, V. Muñoz Sanjosé, M. Hopkinson, E. D. L. Rienks, M. F. Jensen, and P. Hofmann. *Surface band-gap narrowing in quantized electron accumulation layers*. Phys. Rev. Lett., 104:256803 (2010).
- [112] M. Bianchi, D. Guan, S. Bao, J. Mi, B. Iversen, P. King, and P. Hofmann. *Coexistence of the topological state and a two-dimensional electron gas on the surface of Bi_2Se_3* . Nature communications, 1:128 (2010).
- [113] L. Barreto, L. Kühnemund, F. Edler, C. Tegenkamp, J. Mi, M. Bremholm, B. B. Iversen, C. Frydendahl, M. Bianchi, and P. Hofmann. *Surface-dominated transport on a bulk topological insulator*. Nano Letters, 14(7):3755 (2014).
- [114] B. Rousseau and H. Estrade-Szwarckopf. *Photoelectron core level spectroscopy study of K- and Rb-graphite intercalation compound -II. clean surface study*. Solid State Communication, 85(9):793 (1993).

- [115] S. Vajna, E. Simon, A. Szilva, K. Palotas, B. Ujfalussy, and L. Szunyogh. *Higher-order contributions to the Rashba-Bychkov effect with application to the Bi/Ag(111) surface alloy*. Phys. Rev. B, 85:075404 (2012).
- [116] L. Moreschini, A. Bendounan, I. Gierz, C. R. Ast, H. Mirhosseini, H. Höchst, K. Kern, J. Henk, A. Ernst, S. Ostanin, F. Reinert, and M. Grioni. *Assessing the atomic contribution to the Rashba spin-orbit splitting in surface alloys: Sb/Ag(111)*. Phys. Rev. B, 79:075424 (2009).
- [117] L. Bawden, J. M. Riley, C. H. Kim, R. Sankar, E. J. Monkman, D. E. Shai, H. I. Wei, E. B. Lochocki, J. W. Wells, W. Meevasana, T. K. Kim, M. Hoesch, Y. Ohtsubo, P. Le Fèvre, C. J. Fennie, K. M. Shen, F. Chou, and P. D. C. King. *Hierarchical spin-orbital polarization of a giant Rashba system*. Science Advances, 1(8):e1500495 (2015).
- [118] Z. Alpichshev, J. G. Analytis, J.-H. Chu, I. R. Fisher, Y. L. Chen, Z. X. Shen, A. Fang, and A. Kapitulnik. *STM imaging of electronic waves on the surface of Bi_2Te_3 : Topologically protected surface states and hexagonal warping effects*. Phys. Rev. Lett., 104:016401 (2010).
- [119] J. Sánchez-Barriga, M. R. Scholz, E. Golias, E. Rienks, D. Marchenko, A. Varykhalov, L. V. Yashina, and O. Rader. *Anisotropic effect of warping on the lifetime broadening of topological surface states in angle-resolved photoemission from Bi_2Te_3* . Phys. Rev. B, 90:195413 (2014).
- [120] H. Zhang, C.-X. Liu, and S.-C. Zhang. *Spin-orbital texture in topological insulators*. Phys. Rev. Lett., 111:066801 (2013).
- [121] Z. Zhu, Y. Cheng, and U. Schwingenschlögl. *Orbital-dependent Rashba coupling in bulk $BiTeCl$ and $BiTeI$* . New Journal of Physics, 15(2):023010 (2013).
- [122] M. Bahramy, P. King, A. de la Torre, J. Chang, M. Shi, L. Patthey, G. Balakrishnan, P. Hofmann, R. Arita, N. Nagaosa, and F. Baumberger. *Emergent quantum confinement at topological insulator surfaces*. Nat Commun, 3:1159 (2012).
- [123] Q. Liu, C.-X. Liu, C. Xu, X.-L. Qi, and S.-C. Zhang. *Magnetic impurities on the surface of a topological insulator*. Phys. Rev. Lett., 102:156603 (2009).
- [124] J. Henk, M. Flieger, I. V. Maznichenko, I. Mertig, A. Ernst, S. V. Eremeev, and E. V. Chulkov. *Topological character and magnetism of the Dirac state in Mn-doped Bi_2Te_3* . Phys. Rev. Lett., 109:076801 (2012).
- [125] D. A. Abanin and D. A. Pesin. *Ordering of magnetic impurities and tunable electronic properties of topological insulators*. Phys. Rev. Lett., 106:136802 (2011).
- [126] D. K. Efimkin and V. Galitski. *Self-consistent theory of ferromagnetism on the surface of a topological insulator*. Phys. Rev. B, 89:115431 (2014).
- [127] Y. H. Choi, N. H. Jo, K. J. Lee, H. W. Lee, Y. H. Jo, J. Kajino, T. Takabatake, K.-T. Ko, J.-H. Park, and M. H. Jung. *Simple tuning of carrier type in topological insulator Bi_2Se_3 by mn doping*. Applied Physics Letters, 101(15):152103 (2012).

- [128] S.-Y. Xu, M. Neupane, C. Liu, D. Zhang, A. Richardella, L. Andrew Wray, N. Alidoust, M. Leandersson, T. Balasubramanian, J. Sanchez-Barriga, O. Rader, G. Landolt, B. Slomski, J. Hugo Dil, J. Osterwalder, T.-R. Chang, H.-T. Jeng, H. Lin, A. Bansil, N. Samarth, and M. Zahid Hasan. *Hedgehog spin texture and Berry's phase tuning in a magnetic topological insulator*. Nat Phys, 8(8):616 (2012).
- [129] J. Fransson, A. M. Black-Schaffer, and A. V. Balatsky. *Engineered near-perfect backscattering on the surface of a topological insulator with nonmagnetic impurities*. Phys. Rev. B, 90:241409 (2014).
- [130] L. A. Wray, S.-Y. Xu, Y. Xia, D. Hsieh, A. V. Fedorov, Y. S. Hor, R. J. Cava, A. Bansil, H. Lin, and M. Z. Hasan. *A topological insulator surface under strong Coulomb, magnetic and disorder perturbations*. Nat Phys, 7(1):32 (2011).
- [131] M. R. Scholz, J. Sánchez-Barriga, D. Marchenko, A. Varykhalov, A. Volykhov, L. V. Yashina, and O. Rader. *Tolerance of topological surface states towards magnetic moments: Fe on Bi₂Se₃*. Phys. Rev. Lett., 108:256810 (2012).
- [132] J. Honolka, A. A. Khajetoorians, V. Sessi, T. O. Wehling, S. Stepanow, J.-L. Mi, B. B. Iversen, T. Schlenk, J. Wiebe, N. B. Brookes, A. I. Lichtenstein, P. Hofmann, K. Kern, and R. Wiesendanger. *In-plane magnetic anisotropy of Fe atoms on Bi₂Se₃(111)*. Phys. Rev. Lett., 108:256811 (2012).
- [133] S. Jia, H. Beidenkopf, I. Drozdov, M. K. Fuccillo, J. Seo, J. Xiong, N. P. Ong, A. Yazdani, and R. J. Cava. *Defects and high bulk resistivities in the Bi-rich tetradymite topological insulator Bi_{2+x}Te_{2-x}Se*. Phys. Rev. B, 86:165119 (2012).
- [134] C. Piamonteze, U. Flechsig, S. Rusponi, J. Dreiser, J. Heidler, M. Schmidt, R. Wetter, M. Calvi, T. Schmidt, H. Pruchova, J. Krempasky, C. Quitmann, H. Brune, and F. Nolting. *X-Treme beamline at SLS: X-ray magnetic circular and linear dichroism at high field and low temperature*. Journal of Synchrotron Radiation, 19(5):661 (2012).
- [135] A. M. Black-Schaffer, A. V. Balatsky, and J. Fransson. *Filling of magnetic-impurity-induced gap in topological insulators by potential scattering*. Phys. Rev. B, 91:201411 (2015).
- [136] M. Wada, S. Murakami, F. Freimuth, and G. Bihlmayer. *Localized edge states in two-dimensional topological insulators: Ultrathin Bi films*. Phys. Rev. B, 83:121310 (2011).
- [137] S. Murakami. *Quantum spin Hall effect and enhanced magnetic response by spin-orbit coupling*. Phys. Rev. Lett., 97:236805 (2006).
- [138] Y. M. Koroteev, G. Bihlmayer, E. V. Chulkov, and S. Blügel. *First-principles investigation of structural and electronic properties of ultrathin Bi films*. Phys. Rev. B, 77:045428 (2008).
- [139] T. Hirahara, G. Bihlmayer, Y. Sakamoto, M. Yamada, H. Miyazaki, S.-i. Kimura, S. Blügel, and S. Hasegawa. *Interfacing 2D and 3D topological insulators: Bi(111) bilayer on Bi₂Te₃*. Phys. Rev. Lett., 107:166801 (2011).

- [140] L. Miao, Z. Wang, W. Ming, M.-Y. Yao, M. Wang, F. Yang, Y. Song, F. Zhu, A. Fedorov, Z. Sun, C. Gao, C. Liu, i.-K. Xue, C.-X. Liu, F. Liu, D. Qian, and J.-F. Jia. *Quasiparticle dynamics in reshaped helical Dirac cone of topological insulators*. Proceedings of the National Academy of Sciences of the United States of America, 110(8):2758 (2013).
- [141] R. Takahashi and S. Murakami. *Gapless interface states between topological insulators with opposite Dirac velocities*. Phys. Rev. Lett., 107:166805 (2011).
- [142] T. c. v. Rauch, M. Flieger, J. Henk, and I. Mertig. *Nontrivial interface states confined between two topological insulators*. Phys. Rev. B, 88:245120 (2013).
- [143] C. De Beule and B. Partoens. *Gapless interface states at the junction between two topological insulators*. Phys. Rev. B, 87:115113 (2013).
- [144] M. Chen, J. Peng, H. Zhang, L. Wang, K. He, X. Ma, and Q. Xue. *Molecular beam epitaxy of bilayer Bi(111) films on topological insulator Bi₂Te₃: A scanning tunneling microscopy study*. Applied Physics Letters, 101 (2012).
- [145] Z. F. Wang, M.-Y. Yao, W. Ming, L. Miao, F. Zhu, C. Liu, C. L. Gao, D. Qian, J.-F. Jia, and F. Liu. *Creation of helical Dirac fermions by interfacing two gapped systems of ordinary fermions*. Nat. Commun., 4:1384 (2013).
- [146] C. Gao, D. Qian, C. Liu, J. Jia, and F. Liu. *Topological edge states and electronic structures of a 2D topological insulator: Single-bilayer Bi (111)*. Chinese Physics B, 22 (2013).
- [147] Z.-Q. Huang, F.-C. Chuang, C.-H. Hsu, Y.-T. Liu, H.-R. Chang, H. Lin, and A. Bansil. *Nontrivial topological electronic structures in a single Bi(111) bilayer on different substrates: A first-principles study*. Phys. Rev. B, 88:165301 (2013).
- [148] R. S. Markiewicz. *Bridging k and q space in the cuprates: Comparing angle-resolved photoemission and STM results*. Phys. Rev. B, 69:214517 (2004).
- [149] L. Simon, C. Bena, F. Vonau, M. Cranney, and D. Aubel. *Fourier-transform scanning tunnelling spectroscopy: the possibility to obtain constant-energy maps and band dispersion using a local measurement*. J. Phys. D: Appl. Phys, 44:464010 (2011).
- [150] J. E. Hoffman, E. W. Hudson, K. M. Lang, V. Madhavan, H. Eisaki, S. Uchida, and J. C. Davis. *A four unit cell periodic pattern of quasi-particle states surrounding vortex cores in Bi₂Sr₂CaCu₂O₈*. Science, 295(5554):466 (2002). <http://www.sciencemag.org/content/295/5554/466.full.pdf>.
- [151] K. McElroy, D.-H. Lee, J. E. Hoffman, K. M. Lang, J. Lee, E. W. Hudson, H. Eisaki, S. Uchida, and J. C. Davis. *Coincidence of checkerboard charge order and antinodal state decoherence in strongly underdoped superconducting Bi₂Sr₂CaCu₂O_{8+δ}*. Phys. Rev. Lett., 94:197005 (2005).
- [152] P. Roushan, J. Seo, C. Parker, Y. Hor, D. Hsieh, D. Qian, A. Richardella, M. Hasan, R. Cava, and A. Yazdani. *Topological surface states protected from backscattering by chiral spin texture*. Nature, 460(7259):1106 (2009).

- [153] C. Fang, M. J. Gilbert, S.-Y. Xu, B. A. Bernevig, and M. Z. Hasan. *Theory of quasiparticle interference in mirror-symmetric two-dimensional systems and its application to surface states of topological crystalline insulators*. Phys. Rev. B, 88:125141 (2013).
- [154] *Igor Pro (Wavemetrics, Lake Oswego, OR, USA)*.
- [155] K. K. Gomes, W. Ko, W. Mar, Y. Chen, Z.-X. Shen, and H. C. Manoharan. *Quantum imaging of topological unpaired spin polarized Dirac fermions*. arXiv (2009).
- [156] C. Hess, S. Sykora, T. Hänke, R. Schlegel, D. Baumann, V. B. Zabolotnyy, L. Harnagea, S. Wurmehl, J. van den Brink, and B. Büchner. *Interband quasiparticle scattering in superconducting LiFeAs reconciles photoemission and tunneling measurements*. Phys. Rev. Lett., 110:017006 (2013).
- [157] D. Watson. *The natural neighbor series manuals and source codes*. Computers & Geosciences, 25(4):463 (1999).
- [158] R. Wang and H. Steinfink. *The crystal chemistry of selected AB₂ rare earth compounds with selenium, tellurium, and antimony*. Inorganic Chemistry, 6(9):1685 (1967). <http://dx.doi.org/10.1021/ic50055a017>.
- [159] A. Acatrinei, D. Browne, Y. B. Losovyj, D. P. Young, M. Moldovan, J. Y. Chan, P. T. Sprunger, and R. L. Kurtz. *Angle-resolved photoemission study and first-principles calculation of the electronic structure of LaSb₂*. Journal of Physics: Condensed Matter, 15(33):L511 (2003).
- [160] D. P. Young, R. G. Goodrich, J. F. DiTusa, S. Guo, P. W. Adams, J. Y. Chan, and D. Hall. *High magnetic field sensor using LaSb₂*. Applied Physics Letters, 82(21):3713 (2003).
- [161] J. F. DiTusa, V. Guritanu, S. Guo, D. P. Young, P. W. Adams, R. G. Goodrich, J. Y. Chan, and D. V. D. Marel. *Optical conductivity and superconductivity in LaSb₂*. Journal of Physics: Conference Series, 273(1) (2011).
- [162] A. Husmann, J. B. Betts, G. S. Boebinger, A. Migliori, T. F. Rosenbaum, and M.-L. Saboungi. *Megagauss sensors*. Nature, 417(6887):421 (2002).
- [163] J. R. Reitz and A. W. Overhauser. *Magnetoresistance of potassium*. Phys. Rev., 171:749 (1968).
- [164] A. H. Castro Neto. *Charge density wave, superconductivity, and anomalous metallic behavior in 2D transition metal dichalcogenides*. Phys. Rev. Lett., 86:4382 (2001).
- [165] R. G. Goodrich, D. Browne, R. Kurtz, D. P. Young, J. F. DiTusa, P. W. Adams, and D. Hall. *de Haas van Alphen measurements of the electronic structure of LaSb₂*. Phys. Rev. B, 69:125114 (2004).
- [166] S. Guo, D. P. Young, P. W. Adams, X. S. Wu, J. Y. Chan, G. T. McCandless, and J. F. DiTusa. *Dimensional crossover in the electrical and magnetic properties of the layered LaSb₂ superconductor under pressure: The role of phase fluctuations*. Phys. Rev. B, 83:174520 (2011).

-
- [167] *Karl F. F. Fischer, private conversation.*
- [168] P. Blaha, K. Schwarz, G. Madsen, D. Kvasnicka, and J. Luitz. *WIEN2k, an augmented plane wave + local orbitals program for calculating crystal properties* (2001).
- [169] P. Zhang, P. Richard, T. Qian, Y.-M. Xu, X. Dai, and H. Ding. *A precise method for visualizing dispersive features in image plots.* Review of Scientific Instruments, 82(4):043712 (2011).
- [170] J. Hu and T. F. Rosenbaum. *Classical and quantum routes to linear magnetoresistance.* Nat Mater, 7(9):697 (2008).
- [171] R. Xu, A. Husmann, T. F. Rosenbaum, M.-L. Saboungi, J. E. Enderby, and P. B. Littlewood. *Large magnetoresistance in non-magnetic silver chalcogenides.* Nature, 390(6655):57 (1997).